# Thin-film InGaAs metamorphic buffer for telecom C-band quantum dots and optical resonators

Von der Fakultät Mathematik und Physik der Universität Stuttgart
zur Erlangung der Würde eines Doktors der Naturwissenschaften
(Dr. rer. nat.) genehmigte Abhandlung

Vorgelegt von

**Robert Sittig**

aus Stuttgart

| | |
|---|---|
| Hauptberichter: | Prof. Dr. Peter Michler |
| Mitberichter: | PD. Dr. Eberhard Goering |

Tag der mündlichen Prüfung: 22. Mai 2023

Institut für Halbleiteroptik und Funktionelle Grenzflächen
Universität Stuttgart

2023

# Erklärung

**Schriftliche Bestätigung der eigenständig erbrachten Leistung gemäß § 6 Absatz 2 der Promotionsordnung der Universität Stuttgart**

Die eingereichte Dissertation zum Thema

**Thin-film InGaAs metamorphic buffer for telecom C-band quantum dots and optical resonators**

stellt meine eigenständig erbrachte Leistung dar.

Ich habe ausschließlich die angegebenen Quellen und Hilfsmittel benutzt. Wörtlich oder inhaltlich aus anderen Werken übernommene Angaben habe ich als solche kenntlich gemacht.

Die Richtigkeit der hier getätigten Angaben bestätige ich und versichere, nach bestem Wissen die Wahrheit erklärt zu haben.

| ____________________ | ____________________ |
| --- | --- |
| Ort, Datum | Unterschrift |

# Abstract

The advent of quantum cryptography applications holds the prospect of opening a new chapter of telecommunication. One vital building block for these technologies is access to efficient non-classical light sources. Recent breakthroughs have been reported in the effort of attaining high-quality single-photon emission from quantum dots inside the crucial telecom C-band. One attractive route in this regard is to apply additional strain-engineering to the established InAs-on-GaAs material system by inserting a metamorphic buffer. This approach has already demonstrated promising optical properties. However, an integration of these quantum dot emitters into an advanced photonic structure to enhance extraction efficiency and to utilize beneficial cavity effects is still missing.
This thesis aims at establishing an InGaAs metamorphic buffer that facilitates compatibility with conventional photonic cavity structures as well as common lithography fabrication methods. For this purpose, a next-generation buffer design is proposed and discussed. Its non-linear, strain-optimized content grading enables maximum lattice transition at minimal thickness. This thin-film design is then realized via metal-organic vapour-phase epitaxy. Here, a comprehensive optimization of growth parameters is conducted to attain maximum crystalline quality. This process includes fine-tuning the quantum dot emission to 1550 nm wavelength and an optimization for maximum brightness plus minimal fine-structure splitting. Furthermore, the completed layer stack is characterized structurally and design resiliencies within the buffer layer are explored. Markedly, a minimum feasible stable thickness of 170 nm is found. Moreover, benchmark emission properties like single-photon purity, linewidth and decay

time consistently exhibit favorable comparability to their traditional quantum dot system counterparts. Finally, the integration of the thin-film metamorphic structure into various exemplary advanced photonic cavities is investigated. Critically, the feasibility of necessary design adaptations is examined, determining flexibilities and limitations.
The presented results constitute a significant step towards the fabrication of high-quality single-photon sources inside the telecom C-band based on semiconductor quantum dots. Accordingly, the obtained progress will boost the real-world implementation of emerging communication technologies based on non-classical light.

# Kurzfassung

Die Einführung von Anwendungen der Quantenkryptografie hat das Potential ein neues Kapitel der Telekommunikation aufzuschlagen. Ein wichtiger Baustein für diese Technologien ist der Zugang zu effizienten Quellen nicht-klassischen Lichts. In jüngster Zeit konnten substantielle Durchbrüche vermeldet werden hinsichtlich der Bemühungen hochwertige Einzelphotonenemission im telecom C-Band aus Quantenpunkten zu erhalten. Ein attraktiver Weg zu diesem Ziel ist es durch das Einfügen eines metamorphen Puffers zusätzliches strain-engineering auf das etablierte InAs-auf-GaAs-Materialsystem anzuwenden. Dieser Ansatz hat bereits vielversprechende optische Eigenschaften aufgezeigt. Allerdings steht eine Integration dieser Quantenpunkt-Emitter in eine leistungsfähige photonische Struktur zur Verbesserung der Extraktionseffizienz und zur Nutzung von vorteilhaften Kavitäten-Effekten noch aus.
Ziel dieser Arbeit ist die Entwicklung eines metamorphen InGaAs-Puffers, der sowohl die Kompatibilität mit konventionellen photonischen Kavitätenstrukturen ermöglicht als auch mit gängigen lithographischen Herstellungsverfahren kompatibel ist. Zu diesem Zweck wird ein Pufferdesign der nächsten Generation eingeführt und diskutiert. Sein nichtlinearer, verspannungsoptimierter Kompositionsverlauf ermöglicht eine maximalen Gitteränderung bei minimaler Dicke. Dieses Dünnschichtdesign wird dann durch metallorganische Gasphasenepitaxie realisiert. Hierfür wird eine umfassende Optimierung der Wachstumsparameter durchgeführt um maximale Kristallqualität zu erhalten. Dieser Prozess umfasst die Feinabstimmung der Quantenpunktemission auf 1550 nm Wellenlänge, eine Maximierung der Helligkeit sowie eine Minimierung der Feinstrukturaufspaltung. Desweiteren

wird der fertige Schichtstapel strukturell charakterisiert und die Anpassungsfähigkeit der Pufferschicht untersucht. Maßgeblich wird eine minimale verwendbare Dicke von 170 nm aufgezeigt. Darüber hinaus zeigen Benchmark-Emissionseigenschaften wie Einzelphotonenreinheit, Linienbreite und Abklingverhalten durchgängig eine positive Vergleichbarkeit mit ihren traditionellen Quantenpunkt-Gegenstücken. Schließlich wird die Integration der dünnfilm metamorphen Struktur in verschiedene beispielhafte leistungsfähige photonische Kavitäten untersucht. Die Durchführbarkeit notwendiger Designanpassungen wird kritisch durchleuchtet um dabei Flexibilitäten und Grenzen zu ermitteln.
Die vorgestellten Ergebnisse sind ein erheblicher Schritt in Richtung der Herstellung von hochwertigen Einzelphotonenquellen im telecom C-Band basierend auf Halbleiter-Quantenpunkten. Dementsprechend werden die erzielten Fortschritte zur praktischen Einführung neuer Kommunikationstechnologien die auf nicht-klassischem Licht basieren betragen.

# Acronyms, Symbols, and Materials

## Acronyms

| Notation | Fully written out |
|---|---|
| AFM | atomic-force microscopy |
| AnnCap | annealing capping layer |
| $\alpha$-/$\beta$-dislocation | misfit dislocation with group-III/V atoms at its core |
| C-band | telecom C-band |
| Cap | capping layer |
| cw | continuous-wave |
| DBR | distributed Bragg-reflector |
| DOS | density of states |
| fcc | face centered cubic |
| FM | Frank-van-der-Merwe (growth mode) |
| FSS | fine-structure splitting |
| FWHM | full-width at half-maximum |
| HAADF | high angle annular dark field |
| IR | infrared |
| I-V curve | current over voltage curve |
| jci | jump-convex-inverse |
| LCAO | linear combination of atomic orbitals |
| MBE | molecular beam epitaxy |
| MD | misfit dislocation |
| MDFZ | misfit dislocation free zone |

| | |
|---|---|
| MFC | mass-flow-controller |
| μ-PL | micro-photoluminescence |
| ML | mono layer |
| MMB | metamorphic buffer |
| MOVPE | metal-organic vapour-phase epitaxy |
| NA | numerical aperture |
| NIR | near infrared |
| PIN | positive-intrinsic-negative |
| PL | photoluminescence |
| QD | quantum dot |
| R | Oswald ripening growth phase |
| RMS | root-mean-square (roughness) |
| RSM | reciprocal space map |
| SC | semiconductor |
| SEM | scanning electron microscopy |
| SK | Stranski-Krastanow (growth mode) |
| SSPD | superconducting single-photon detector |
| STEM | high resolution scanning transmission electron microscopy |
| TCSPC | time-correlated single-photon counting |
| TEM | transmission electron microscopy |
| TD | threading dislocation |
| UV | ultraviolet |
| V/III ratio | ratio of group V to group III atom types |
| VCSEL | vertical cavity surface emitting laser |
| VW | Volmer-Weber (growth mode) |
| WL | wetting layer |
| XRD | high-resolution X-ray diffraction |
| XRR | X-ray reflectometry |
| X | exciton |
| X+ | positively charged trion |
| X− | negatively charged trion |
| XX | biexciton |
| z-direction | growth direction of the epitaxy |

# Physical Constants and Symbols

| Notation | Description |
|---|---|
| $a$ | lattice constant |
| $E$ | energy |
| $E_d$ | diffusion energy |
| $E_G$ | band gap energy |
| $E_F$ | Fermi energy |
| $f$ | lattice mismatch |
| $g^{(2)}(\tau)$ | second-order correlation function |
| $\gamma_e$ | surface free energy of newly grown layer |
| $\gamma_i$ | interfacial free energy |
| $\gamma_s$ | surface free energy of previous layer |
| $h$ | layer thickness/height |
| $h_c$ | critical thickness |
| $\vec{k}$ | pseudo-wave-vector |
| $\bar{\mu}_i$ | electrochemical potential |
| $n$ | refractive index |
| $\nu$ | Poissin ratio |
| $q_{x/y/z}$ | reciprocal space direction/vector |
| $R^2$ | coefficient of determination |
| $T$ | Temperature |
| $\theta_c$ | contact angle |
| $V$ | volume |
| $V_c$ | volume of Wigner-Seitz unit cell |
| Z | atomic number |

# Materials

| Notation | Fully written out |
|---|---|
| AlAs | aluminium arsenide |
| AlGaAs | aluminium gallium arsenide |
| AlGaInP | aluminium gallium indium phosphide |
| $AsH_3$ | arsine |
| $CBr_4$ | tetrabromomethane |
| DMZn | dimethylzinc |
| GaAs | gallium arsenide |
| GaAs:Si | silicon doped gallium arsenide |
| GaInP | gallium indium phosphide |
| $H_2$ | hydrogen |
| InAs | indium arsenide |
| InGaAs | indium gallium arsenide |
| InP | indium phosphide |
| $PH_3$ | phosphine |
| $SiH_4$ | silane |
| $Si_2H_6$ | disilane |
| TEGa | triethylgallium |
| TMAl | trimethylaluminium |
| TMGa | trimethylgallium |
| TMIn | trimethylindium |
| ZnSe | zincselenide |

# Contents

**1 Introduction** **17**

**2 Basic Concepts** **25**

2.1 Semiconductor Crystals . . . . . . . . . . . . . . . . . . 26
2.1.1 Crystal Lattice . . . . . . . . . . . . . . . . . . 26
2.1.2 Band Structure . . . . . . . . . . . . . . . . . . . 27
2.1.3 Density of States in Low-dimensional Systems . 29
2.2 Heteroepitaxy of Semiconductors . . . . . . . . . . . . 30
2.2.1 Metal-Organic Vapour-Phase Epitaxy . . . . . 30
2.2.1.1 AIX-200 . . . . . . . . . . . . . . . . . 33
2.2.2 Nucleation . . . . . . . . . . . . . . . . . . . . . 34
2.2.3 Growth Modes . . . . . . . . . . . . . . . . . . . 36
2.2.4 Metamorphic Relaxation . . . . . . . . . . . . . 38
2.2.4.1 Relaxation models . . . . . . . . . . . 42
2.2.5 Metamorphic Buffer Growth . . . . . . . . . . . 43
2.2.5.1 Content grading . . . . . . . . . . . . 43
2.2.5.2 Dislocation coalescence/annihilation . 46
2.2.5.3 Temperature grading . . . . . . . . . . 47
2.2.6 Self-Assembled Quantum Dots . . . . . . . . . . 48
2.2.7 Distributed Bragg reflector . . . . . . . . . . . . 51
2.3 Methods . . . . . . . . . . . . . . . . . . . . . . . . . . 52
2.3.1 Atomic force microscopy . . . . . . . . . . . . . 52
2.3.2 High-resolution X-ray diffraction . . . . . . . . . 54
2.3.3 Electron microscopy . . . . . . . . . . . . . . . . 56
2.3.4 Photoluminescence . . . . . . . . . . . . . . . . . 56
2.3.5 Photolithography . . . . . . . . . . . . . . . . . . 57

**3 Thin-Film Buffer** **59**
3.1 Relaxation-optimized buffer design . . . . . . . . . . . 60
3.2 Growth parameter optimization . . . . . . . . . . . . . . 61
3.2.1 Jump layer . . . . . . . . . . . . . . . . . . . . 62
3.2.1.1 High temperature 2D-3D transition . 63
3.2.1.2 Approaches of controlling the surface diffusion . . . . . . . . . . . . . . . . 65
3.2.1.3 Temperature investigation, coarse . . 67
3.2.1.4 Low temperature 2D-3D transition . . 68
3.2.1.5 Temperature investigation, fine . . . . 70
3.2.1.6 Plastic relaxation initiation . . . . . . 71
3.2.1.7 V/III ratio . . . . . . . . . . . . . . . 75
3.2.2 Convex grading layer . . . . . . . . . . . . . . . 76
3.2.3 Inverse layer . . . . . . . . . . . . . . . . . . . 81
3.3 QD growth optimization . . . . . . . . . . . . . . . . . 84
3.4 Additional structural characterization . . . . . . . . . 92
3.4.1 AFM . . . . . . . . . . . . . . . . . . . . . . . 92
3.4.2 XRD . . . . . . . . . . . . . . . . . . . . . . . 93
3.4.3 STEM . . . . . . . . . . . . . . . . . . . . . . 96
3.5 Stability against growth parameter changes . . . . . . 99
3.5.1 Jump-layer thickness . . . . . . . . . . . . . . . 99
3.5.2 Jump-layer indium content . . . . . . . . . . . 101
3.5.3 Constant V/III ratio . . . . . . . . . . . . . . . 101
3.5.4 Reactor pressure . . . . . . . . . . . . . . . . . 102
3.5.5 Growth rate . . . . . . . . . . . . . . . . . . . . 103
3.5.6 Substrate offcut . . . . . . . . . . . . . . . . . . 104
3.5.7 Total structure thickness . . . . . . . . . . . . . 105
3.5.8 Annealing . . . . . . . . . . . . . . . . . . . . . 110
3.5.8.1 QD temperature stability . . . . . . . 113

**4 Photonic devices** **115**
4.1 Planar cavity with bottom DBR . . . . . . . . . . . . 115
4.1.1 Optical characterization . . . . . . . . . . . . . 118
4.2 Planar cavity with bottom and top reflector . . . . . . 123
4.3 Gaußian-shaped cavity . . . . . . . . . . . . . . . . . . 125

4.4 Circular Bragg grating cavity . . . . . . . . . . . . . . . 129
4.5 Grating outcoupler . . . . . . . . . . . . . . . . . . . . . . 131
4.6 PIN diode . . . . . . . . . . . . . . . . . . . . . . . . . . 133
4.6.1 p-side doping . . . . . . . . . . . . . . . . . . . . . 133
4.6.2 n-side doping . . . . . . . . . . . . . . . . . . . . . 136
4.6.3 PIN diode structure . . . . . . . . . . . . . . . . . 137

**5 Summary and Outlook 141**

**6 Appendix 155**
6.1 XRR example . . . . . . . . . . . . . . . . . . . . . . . . . 155
6.2 μ-PL spectrum with strong background . . . . . . . . . 156
6.3 Hole analysis QD overgrowth . . . . . . . . . . . . . . . 156
6.4 Refilling in pulsed second-order auto-correlation measurement . . . . . . . . . . . . . . . . . . . . . . . . . . 162
6.5 Surface morphology $CBr_4$ doping . . . . . . . . . . . . 163
6.6 XRD of zinc doped InGaAs . . . . . . . . . . . . . . . . 163
6.7 AFM of zinc and silicon doped InGaAs . . . . . . . . . . 165
6.8 RSM analysis program . . . . . . . . . . . . . . . . . . . 165

Chapter 1

# Introduction

Progression in means of communication defines the development of humankind and civilization, all the way back, starting from spoken [1, 2] and written language [3, 4].
Examples from ancient history are how the Egyptian empire was transformed by a shift from writing in stone to the more convenient papyrus [5] or how the invention of the Greek alphabet shaped but also divided societies [6]. The development of communication technologies can span hundreds of years and thousands of kilometers. Like the invention of paper and the printing press, having early roots in 8th century China, followed by usage all around East Asia [7]. However, the perfection of this technique is ascribed to Johannes Gutenberg in 15th-century Europe [8].
One pillar of communication is to ensure the transmission and accessibility of knowledge through time. Projects like the Library of Alexandria with its rise [9] and destruction [10] mark historical turning points. Also, the significance of knowledge collection and distribution for religious upheaval in medieval Europe can hardly be overstated [11].
Another aspect of information transmission is the speed at which physical distance can be bridged. Therefore, from time immemorial, significant effort has been taken to accelerate message delivery, from the arduous maintenance of signal fire chains [12–14] to the sophisticated network of carrier pigeon [15]. Moreover, for over two-thousand years, the equine express postal system constituted the

most trusted and flexible solution [16]. Only as part of the Industrial Revolution in the late 18th and early 19th century was this system improved by mechanization resulting in more efficient transportation of physical messages [17]. Nevertheless, it was the invention of the electric telegraph in 1837 [18] that heralded the beginning of modern telecommunication via well-defined electromagnetic waves. The evolution of this technology went through milestones like the radio, the telephone and the television [19–21], and finally reached the stage of the computer-accessed internet as a universal, interactive two-way medium [22]. This development simultaneously triggered the Communication Revolution [23] and hence dictated the rhythm for the dawn of the information society [24].

The story of communication is decisively and inextricably linked with the safety of any transmission against interference and eavesdropping from third parties. This context also explains the significance of cryptography techniques. From simple monoalphabetic substitution [25] through more sophisticated approaches like the Vigenère Cipher [26] to methods like computer-based RSA encryption [27], ciphers and their decryption have shaped history. They have decided royal lines of succession [28], and impacted the outcome of wars [29]. Clearly, our 21st-century lifestyle, embedded in the Communication Revolution and hence permeated by connectivity, demands equally powerful and revolutionary means of encryption. Fortunately, the field of quantum cryptography promises an answer to this challenge.

The original idea came from Stephen Wiesner and was published in 1983 [30]. However, one of the proposed applications, forging-impervious quantum money, was hardly technically feasible, while the approach to a communication scheme based on faint polarized light pulses lacked absolute security. Still, it provided the impulse for Bennett and Brassard to develop their famous BB84 quantum key distribution (QKD) protocol just one year later [31]. This concept utilizes polarized single-photons and hence draws on the no-cloning theorem [32, 33] to attain provable secure communication. After this milestone, further transmission protocols were conceived, either refined versions of BB84 [34, 35] or taking other angles to the problem

[36, 37], often including the generation of entangled two-photon states [38]. Nevertheless, while the original quantum cryptography concept has been tamed into the realm of feasibility, actual real-world implementation remains challenging. Most critically, the dependency on appropriate reliable single-photon emitters represents a major roadblock.
These devices, which in their idealized form are also dubbed "photon guns", are most prominently realized based on few-level quantum systems. Various contenders are employed for this purpose, including trapped atoms [39], molecules [40], superconducting circuits [41], metamaterials [42], vacancy centers in crystals like SiC [43] or diamond [44] and semiconductor (SC) quantum dots (QDs) [45]. The aforementioned quantum cryptography protocols impose stringent requirements on these single-photon sources in terms of brightness, purity and indistinguishability. Moreover, they should emit on-demand and show a high entanglement fidelity. Lastly, a significant constraint is put on these emitters to generate photons at telecom wavelengths to enable compatibility with the existing communication infrastructure [46]. In the end, all the mentioned candidates have advantages and drawbacks in various categories.
In the case of QDs, the biggest boon, as well as curse of these artificial atoms, is their encapsulation into a solid-state matrix. On the one hand, this embedding constitutes a gateway for undesirable interaction with the surrounding, disturbing the quantum states [47]. On the other hand, it allows the fabrication of stable, non-volatile devices and the inherent possibility for electrical excitation and manipulation [48]. Last but not least, modification of the matrix material opens up an avenue for advanced bandgap engineering. For example, the system of InAs QDs on GaAs substrate has demonstrated excellent emission quality in most discussed aspects [49], albeit at suboptimal wavelengths. This shortcoming can be remedied by capitalizing on this flexibility.
More precisely, the $\approx 7\,\%$ smaller lattice constant of GaAs compared to InAs applies significant compressive strain on the QDs. This strain-effect produces a strong blue-shift compared to InAs bulk emission

resulting in a typical wavelength of around 900 nm at cryostatic temperatures [50]. Therefore, some of this strain has to be released in order to reach the pivotal high-transmittance telecom windows at 1310 nm (O-band) and 1550 nm (C-band) [51].
O-band emission has been demonstrated by depositing a thin InGaAs strain-reducing layer directly on top of the QDs [52–54]. Nevertheless, more extensive strain-engineering is necessary to attain C-band emission. One successful approach is a complete switch from the GaAs substrate to the only ≈3.5 % mismatched InP [55–59]. Upon closer inspection, however, the InP matrix does not provide the optimal but rather slightly too little strain for this purpose. Therefore, without considerable effort [60], the InAs/InP system typically emits at longer wavelengths than 1550 nm. Furthermore, this situation leads to undesirable elongation of the QD structures, often forming quantum dashes instead [61], which necessitated an advanced synthesis scheme to mitigate this effect [62]. Therefore, the promising InAs QD emitters can clearly benefit from an alternative, more fine-tuned strain-engineering approach.
Highest-quality substrates for the epitaxy of SCs are only available for few materials, with the most prominent being Si, GaAs, InP and GaN/sapphire. On the other hand, the utilization of metamorphic buffers (MMBs) consisting of their respective alloys like $Si_{1-x}Ge_x$, $In_xGa_{1-x}As$ and $In_xGa_{1-x}N$ offers tremendous flexibility for bandgap and strain-engineering [63, 64]. Here, in contrast to the more traditional pseudomorphic growth, the strain introduced by the epitaxy of lattice-mismatched materials is released partly or wholly through the formation of misfit dislocations [65]. This results in a permanent change of the in-plane lattice constant for the growth of all further layers. Arguably, the GaAs-based system is an ideal candidate for this approach. The possibility of mixing Ga, Al and In at the type-III lattice position [66, 67] and As, P and Sb at the V-lattice-position [68, 69]provides a wealth of ternary (e.g., $In_xAl_{1-x}As$) and even quarternary (e.g., $Al_xGa_{1-x}Sb_yAs_{1-y}$) zincblende SC compounds to choose from for metamorphic growth. This freedom in parameters space allows simultaneous tailoring of properties like lattice constant,

band gap, elastic stiffness [70] and thermal expansion [71]. Naturally, the growth of the MMB at constant composition is the most direct approach to reach the desired mixing ratio. However, this usually becomes impractical at larger mismatches if a 2D growth mode shall be sustained [72, 73]. Therefore, various content grading profiles and their respective relaxation processes have been investigated in recent decades, the most prominent being step- and linearly-graded buffers [74], but sub-, superlinear [75, 76] and s-grading [77] schemes have been implemented as well.
Early work in unlocking the potential of MMB growth in combination with SC QDs focused on the fabrication of QD lasers. In the year 2003, Ledentsov et al. [78] used a molecular beam epitaxy-grown structure, featuring a 1.2 µm thick MMB with constant $In_{0.2}GaAs$ composition, to show photoluminescence from In(Ga)As QDs with an emission maximum at 1450 nm and electrically-driven lasing exceeding 1510 nm utilizing the temperature shift. Later, they extended this range up to 1600 nm by increasing the indium content in the MMB to 25-30 % [79]. In order to compensate for the deterioration of crystal quality caused by the increased lattice mismatch, they had to implement an advanced defect-reduction technique based on strain-sensitive overgrowth and selective evaporation.
Emission at 1550 nm from single QDs grown on a GaAs substrate was reported for the first time in 2008 by Semenova et al. [80]. The $In_xGa_{1-x}As$ MMB they used consisted of a 0.78 µm thick section, which was linearly graded up to $x = 47\,\%$, followed by a 0.4 µm thick inverse step of $In_{0.42}GaAs$. Notably, for QDs to serve as single-photon sources, they must be kept at low temperatures. Thus additional strain reduction is required to offset the missing temperature-shift, which explains the much higher indium content here than MMBs designed for laser applications. The medium QD area density in the $10^9 cm^{-2}$ range observed in this structure made the application of a gold mask with 1-2 µm diameter apertures necessary to isolate single emitters. Nevertheless, Semenova et al. were able to detect sharp lines in the spectrum and observed excitation-power-dependent behavior of integrated intensity, which could be attributed to the exciton

and biexciton transitions. However, the fabrication of bright, low-density In(Ga)As QDs suitable to demonstrate single-photon emission at 1550 nm proved challenging [81] and was not achieved for almost another decade.
In 2017 Paul et al. showed for the first time single-photon emission in the telecom C-band from InAs QDs grown on the GaAs material platform by using a structure including a linearly graded MMB [82]. The sample was fabricated by metal-organic vapor-phase epitaxy (MOVPE), starting with an exactly oriented (100) GaAs substrate, followed by a distributed Bragg reflector to enhance extraction efficiency [83]. The QDs were deposited after the 1080 nm thick $In_xGa_{1-x}As$ MMB with a maximum indium content of 36.7 %. In combination with 220 nm capping, this resulted in a 3λ-cavity between the distributed-Bragg-reflector (DBR) and the SC-air interface with the QDs at the upper anti-node. The area density of optically active QDs was $1 \cdot 10^7\,\mathrm{cm}^{-2}$ and hence low enough to observe single emission lines without post-processing. The optical quality of this emission proved to be favorable in terms of purity, linewidth and fine-structure splitting. The structure allowed to demonstrate polarization-entanglement [84], on-demand generation of entangled photon-pairs [85, 86] and indistinguishability [87, 88]. Nevertheless, while these are impressive achievements, integration of QD emitters into an advanced optical cavity was still pending due to limitations of thickness and surface quality [89]. Clearly, such a photonic device would provide outstanding utility and open up exciting avenues for applications [45].

This thesis aims to design and optimize a suitable MOVPE-grown MMB for InAs QDs emitting in the telecom C-band that retains the previously demonstrated excellent optical properties while enabling compatibility with advanced device fabrication.
Chapter 2 will establish the essential theoretical background and experimental methods upon which this work is built. In chapter 3, first, a dedicated relaxation-optimized grading design for the realization of thin-film MMBs is proposed. Then, meticulous MOVPE growth parameter calibration is conducted to fabricate an InGaAs MMB

based on this design with maximum crystalline quality. Moreover, the acquired lattice constant transition is calibrated for the deposition of telecom C-band InAs QDs. Their growth recipe is then adapted for optimal performance on the MMB virtual substrate. Lastly, an AFM, XRD and STEM characterization of the final QD/MMB structure is performed, followed by an analysis of its stability against growth parameter modifications. Furthermore, chapter 4 explores various routes for device integration and examines the necessary MMB growth adjustments to enable the respective fabrication. Finally, all results are summarized in chapter 5 and an outlook for the QD/MMB approach is presented.

Chapter 2

# Basic Concepts

This chapter will give a short overview of the fundamental physical and technological concepts upon which the work in this thesis is built. The first section contains a basic theoretical description of SC crystals. This includes the concepts of the regular lattice and the energy band structure, specifically their extension to low-dimensional systems. In the second section, the peculiarities of epitaxy with different materials are discussed. A special focus is placed on the metamorphic growth of lattice-mismatched layers and how it is associated with the transition of the lattice constant. Here, broached topics are the formation and propagation of dislocations and utilizing metamorphic layers as buffers, i.e., virtual substrates. Moreover, the strain-moderated deposition of self-assembled 3D islands is reviewed. In particular, how controlling this effect pertains to the fabrication of QDs for high-quality non-classical light emission. The last section gives an introduction to the utilized methods. First, measurement techniques for gauging the crystalline quality of thin-film stacks, like AFM and XRD, are discussed. This is followed up by an explanation of various schemes to evaluate the optical properties of single-photon emitters. Lastly, photolithography as a means to fabricate laterally structured devices is outlined.

## 2.1 Semiconductor Crystals

SCs play a vital role in a wide range of technological applications. This versatility is facilitated by their unique atomic and electronic state structure. Prominent materials like silicon, germanium and gallium arsenide display a remarkably wide range of macroscopic and microscopic properties. Nevertheless, at the same time, all SC crystals are united by distinct common features, which are explained in this section.

### 2.1.1 Crystal Lattice

The main property that distinguishing crystals from other forms of matter is their regular short-range ordering.
Their periodic space lattice is defined by translation relation

$$\vec{r'} = \vec{r} + u\vec{a} + v\vec{b} + w\vec{c}, \tag{2.1}$$

where $\vec{a}, \vec{b}, \vec{c}$ are the basis vectors, and $u, v, w$ are integers. All possible crystalline symmetry types are defined by their Bravais lattice type plus their atomic basis. Fig. 2.1 illustrates this construction on the example of GaAs with zincblende structure. The crystal is of face-centered cubic lattice type, as drawn in Fig. 2.1(a). This symmetry is complemented by a basis consisting of two atoms: the As atom at the (0,0,0) position and the Ga atom at the (1/4,1/4,1/4) position (Fig. 2.1(b)). A GaAs crystal is constructed by combining these two defining components by placing the basis at every lattice point. The result is displayed in Fig. 2.1(c). It represents the primitive building block of this system: the Wigner-Seitz unit cell. Its volume is given by

$$V_c = (\vec{a} \times \vec{b}) \cdot \vec{c}, \tag{2.2}$$

depicting its relation to the basis vectors. Note that only 4 Ga atoms end up actually positioned within this unit cell. Furthermore, the 6 depicted As atoms laying within the plane only count with a factor 1/2 towards this unit cell, and the ones at the corners only with 1/8,

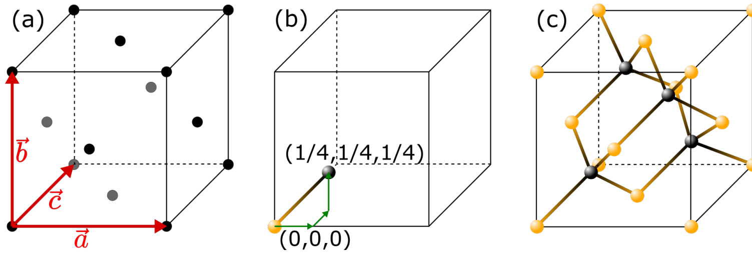


**Fig. 2.1.** Construction of the zincblende lattice for GaAs. (a) Depiction of the face-centered cubic lattice. The basis vectors are drawn in red. (b) Atomic basis of zincblende with As at the (0,0,0) position and Ga at the (1/4,1/4,1/4) position. (c) Complete lattice construction of the GaAs unit cell.

which also adds up to 4. Finally, its paramount that the whole crystal can be assembled in space by shifting and copying the unit cell with the translation vector defined in equation 2.1.
Another useful tool directly connected to crystalline symmetry is the reciprocal lattice. It neatly describes the relation of plane-families within the crystal. Its basis vectors are defined by

$$\vec{a}^* = \frac{\vec{b} \times \vec{c}}{V_c} \quad , \quad \vec{b}^* = \frac{\vec{c} \times \vec{a}}{V_c} \quad \text{and} \quad \vec{c}^* = \frac{\vec{a} \times \vec{b}}{V_c}. \tag{2.3}$$

Overall, this construction represents a Fourier transform of the Bravais lattice. Analogous to the unit cell in real space, the complete reciprocal information is contained in the 1.Brillouin zone as the basic building block. Major applications of this description are found for, e.g., refraction experiments like XRD.

## 2.1.2 Band Structure

Understanding the difference between metallic and semiconductor crystals, e.g., in their temperature-dependent resistivity, necessitates knowledge of their electronic states. Theoretical descriptions like the

LCAO method and the tight-binding model [90] expand the basic free-electron gas model. They acknowledge the fact that the atomic cores of the positive ion lattice affect the electron states beyond compensating charge.
The associated calculations result in the development of energy bands in which all possible $\vec{k}$-states are located. They are complemented by forbidden without any states, i.e., bandgaps. In principle, no periodic order is necessary for the development of a band structure. Instead, it is a consequence of wavefunction overlap akin to the description of bonding and antibonding states in molecules [91, 92].
However, in crystals, symmetry and periodicity must be taken into account. This requirement is covered by selecting a Bloch ansatz for the wavefunction in the form of:

$$\Psi_{\vec{k},\sigma}(\vec{r},t) = u_{\vec{k},\sigma}(\vec{r})e^{i\vec{k}\vec{r}}e^{-\frac{i}{\hbar}E_{\vec{k},\sigma}t}. \tag{2.4}$$

Here, $\vec{k}$ is the pseudo-wave-vector and $\sigma$ is the band index. Most importantly, the Bloch factor $u_{\vec{k},\sigma}(\vec{r})$ incorporates the lattice periodicity of the crystal from equation 2.1 and specifies the modulation within the unit cell.
Furthermore, each electron state in the isolated atom is translated into an energy band with states equal to the number of involved atoms in the solid. The population of these energy bands determines material class, with a special focus on the highest occupied state defining the electrochemical potential $\bar{\mu}_i$ (Fermi energy $E_F$ at 0 K). This relationship can be exemplified by the property of electrical conductivity.
In a good conductor, electrons must have many free states with a large spread of $\vec{k}$-vectors within minimal energy investment. Metals readily fulfill this condition due to their partly-filled highest band, consequently called the conduction band. On the other hand, SCs and insulators possess a completely filled valence band and an entirely empty next band. In the ideal case, this means $\bar{\mu}_i$ is located in the center of the bandgap, and significant energy is necessary to reach free states. Moreover, the magnitude of $\Delta E$ relative to the thermal activation energy distinguishes between SCs and insulators. Furthermore, the position of the smallest energy gap in $\vec{k}$-space classifies direct and

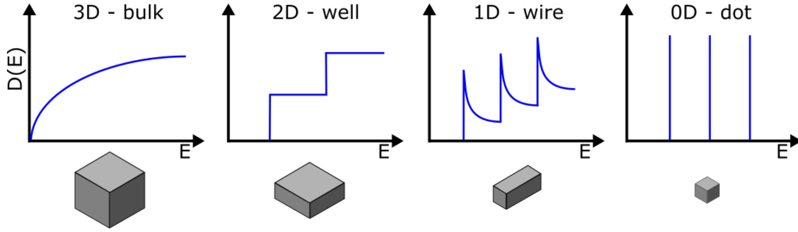


**Fig. 2.2.** Density of states for materials with reduced dimensions including 3D bulk, 2D quantum-wells, 1D nano-wires and 0D QDs.

indirect SCs.
Lastly, a small dosage of well-defined irregularity, i.e., dislocations and foreign atoms, can unlock additional applications by providing energy states within the bandgap. This circumstance is, for example, utilized when designing the conductivity of doped SCs.

### 2.1.3 Density of States in Low-dimensional Systems

Limiting the size of bulk material into the nanometer-range results in unique properties.
An easy illustration of the behavior of electronic states for reduced dimensions can be given by starting at the energy dispersion relation of the free electron model [93] in 3 dimensions:

$$D_{3D}(E) = \frac{V}{(2\pi)^2}(\frac{2m}{\hbar^2})^{3/2}\sqrt{E}. \tag{2.5}$$

Following the same derivation but for only two and one dimensions, leads to

$$D_{2D}(E) = \frac{V}{(2\pi)^2}(\frac{2m}{\hbar^2})^{3/2}\sqrt{E} \tag{2.6}$$

and

$$D_{1D}(E) = \frac{V}{(2\pi)^2}(\frac{2m}{\hbar^2})^{3/2}\sqrt{E}. \tag{2.7}$$

Finally, complete 3D confinement, i.e., 0D objects, results in well-defined, discrete energy levels similar to the behavior of electron states in isolated atoms. The progression of these calculations is displayed in Fig. 2.2.

## 2.2 Heteroepitaxy of Semiconductors

The majority of SC-devices is produced by starting with wafers of pure materials like Si and GaAs, which are then gradually structured by a combination of photolithography and chemical processing 2.3.5. This approach allows to obtain the all-important integrated circuits for microchip technologies, which was the key to our age of information [94]. However, for many applications, this concept has to be complemented by utilizing multiple stacked layers of different SCs on top of the pure wafer. The fabrication of these structures is called heteroepitaxy, and its relevant aspects to this work will be explained in the following sections.

### 2.2.1 Metal-Organic Vapour-Phase Epitaxy

Techniques that can be used to grow thin-film systems for optoelectronic applications have to fulfill demanding specifications. On the one hand, sufficient material purity and precise control over layer thicknesses are mandatory. Moreover, the method must support a flexible input of element types to enable a wide range of bandgap and strain engineering. Simultaneously, layers with varying compositions should be divided at abrupt interfaces. Apart from these points, scaling in terms of throughput is favorable if industrial deployment is pursued. Metal-organic vapour-phase epitaxy (MOVPE) is one of the few techniques successfully employed in this fashion.
This growth method uses precursor molecules where the desired central atom is chemically bound to organic end groups. This arrangement serves two primary purposes. First, it keeps the central atom in an inert state to protect it from premature chemical reactions. Second,

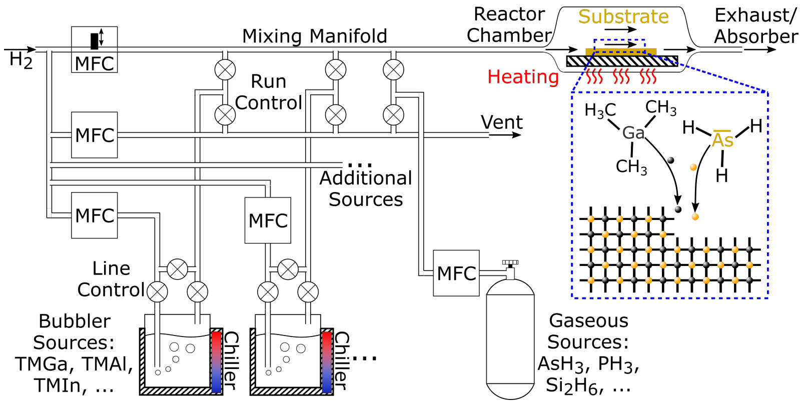


**Fig. 2.3.** Schematic drawing of the MOVPE machine layout. Material supply is either provided by direct gaseous input or mediated by $H_2$ carrier gas passing through bubbler sources. Two exemplary temperature-controlled bubblers and one exemplary gaseous source are depicted. Inlet into the reactor chamber is regulated via MFCs and line plus run valves (cross-circles). Heating of the substrate wafer induces the release of the desired atoms, which are incorporated into the crystalline surface.

the gaseous phase facilitates transportation and precise intermixing of multiple different precursors. Precursor-molecule-enriched gas flux is then introduced into a reactor chamber in the form of a laminar flow. This process is conducted in a range from atmospheric pressure to a few millibars, but markedly not at ultra-high vacuum. Once the molecule has reached its destined position above the heated substrate surface, the chemical bonds are selectively broken via thermal activation, i.e., pyrolysis [95]. As illustrated in the blue box of Fig. 2.3, this releases the central atoms, which are then subject to multiple processes like diffusion, desorption and integration into the lattice. The exact development is difficult to predict but can be readily influenced by growth parameters, e.g., temperature, pressure, and absolute as well as relative precursor fluxes.

Precise and stable infeed into the reactor chamber is facilitated by a

sophisticated upstream supply and mixing unit, of which a simplified version is displayed schematically in Fig. 2.3. $H_2$ with less than 1 x $10^{-6}$ impurity is utilized as carrier gas. One of its tasks is to serve as supplementary, non-reactive flux into the reactor chamber, keeping the total input constant. That way, the conditions for enabling laminar flow above the substrate are stabilized. Additionally, $H_2$ is inserted into the bubbler vessels containing the precursor in liquid form, where the carrier gas then absorbs evaporating vapours. Obviously, the amount of $H_2$ insertion is a major parameter for controlling the total material transport. Additionally, evaporation is managed by setting the pressure in combination with temperature regulation via a chiller. The carrier gas flux into various bubblers is adjustable within a time frame of a few seconds through mass-flow-controllers (MFCs).
Further control is attained by utilizing a two-stage switchable input system. The line stage consists of a bypass that can be switched to the bubblers' in- and output valves (drawn as a circle with a cross). The second run checkpoint can relay the flux either into the reactor or the refuse vent. Opening the line valves for bubbler flow, but keeping the run control set to vent, allows the $H_2$ flow and precursor evaporation to settle and stabilize. Switching a particular material online for insertion into the reactor chamber can then be performed within the $\approx$0.1 s response time of the run valves. Some precursors sources like $AsH_3$ are directly available in gaseous form. In that case, the flux can be set by a single MFC, but the run stage is still utilized. Due to the medium pressure conditions, slightly less purity is achieved in the MOVPE technique compared to the leading competitor, molecular beam epitaxy (MBE). Moreover, some restrictions are imposed on the possible in-situ measurement methods. On the other hand, this circumstance entails much less complex maintenance in order to counteract unwanted reactor wall coverage and the associated quality drop after a certain amount of deposited material. More specifically, an easily exchangeable interior liner system enables fast and almost seamless progression between growth runs and full parameter sweeps at high repetition rates. Consequently, MOVPE can also readily cover several orders of magnitude for layer growth from sub-monolayer [96]

to tens of micrometers [97] without extended outage times. Furthermore, the high throughput allows for fast development circles covering extensive parameter space. Finally, the laminar flow approach enables sufficient homogeneity, specifically at large-scale wafer usage.

**Precursor mixing** Content-graded layers, e.g., MMBs, are obtained by continuously changing the mixing ratio of two precursors like TMGa and TMIn. This can be accomplished by either keeping the growth rate constant and adjusting both fluxes accordingly or by keeping one flux constant and increasing the other. The second technique was used in this thesis. However, when translating a grading function $y(t)$ to a composition functions, a correction of the form

$$In_x = \frac{y(t)}{C + y(t)}, \tag{2.8}$$

has to be considered. Here, C accounts for the incorporation ratio of the two precursors. Function 2.8 captures the effect of an equal amount of material added to a mixture having a diminishing impact on the final composition.

#### 2.2.1.1 AIX-200

Practically all the samples in this thesis are produced with an AIXTRON AIX-200 MOVPE machine. Moreover, the base substrates were 1/6 of a 2" wafer or 1/12 of a 3" wafer (approximately equal in total area) of exactly-oriented (100) GaAs. The only exception is the first 20 AlAs/GaAs pairs of bottom DBR structures, which were prepared on full 2"/3" wafers via an Aixtron Close Coupled Showerhead© machine, cleaved, and then transferred for MMB and QD growth (see also section 4.1).
The AIX-200 has a horizontal reactor with a substrate slot sized for a single 2" wafer. Furthermore, the model in this work generates the required elevated temperatures of up to 810 °C via IR-lamp heating. The temperature-setting feedback unit is a thermocouple mounted

inside the susceptor block. This configuration protects the sensor from physical and chemical stress. It results in a low risk of failure and avoids the necessary recalibration after a possible replacement of the thermocouple, improving reliability. However, the critical value for the growth process is the temperature on top of the substrate, which can be considerably lower than inside the susceptor [98]. This discrepancy increases at higher temperatures. Therefore, the stated steps during optimization, e.g., in section 3.2.1.1, have to be considered slightly uneven.
The available precursors, which were mounted during this work, are trimethylgallium (TMGa), trimethylindium (TMIn), trimethylaluminium (TMAl), triethylgallium (TEGa), arsine ($AsH_3$), phosphine ($PH_3$), carbon tetrabromide ($CBr_4$), dimethylzinc (DMZn), silane ($SiH_4$) and disilane ($Si_2H_6$). The latter four are dopant materials and thus equipped with an additional dilution stage. This refitting allows a much more precise mass flow control and overall significantly lower supply rates.

## 2.2.2 Nucleation

In the macroscopic description, the way one material will form or nucleate on top of another is dictated by the minimization of the (surface) free energy. If $\gamma_e$ represents the surface free energy of the newly grown and $\gamma_s$ of the previous layer and $\gamma_i$ is the interfacial free energy, then complete wetting is expected for $\gamma_s > (\gamma_e + \gamma_i)$, while for $\gamma_i > (\gamma_e + \gamma_s)$ there will be no wetting at all. For all other cases, a partial wetting will, according to Young's equation [99], occur with a contact angle $\theta_c$ of

$$\theta_c = \arccos\left(\frac{\gamma_s - \gamma_i}{\gamma_e}\right), \tag{2.9}$$

which is illustrated in Fig. 2.4(a).
On the other hand, methods like MOVPE require an atomistic model since typical growth conditions make nucleation through nuclei containing as few as two atoms feasible. The processes that must be

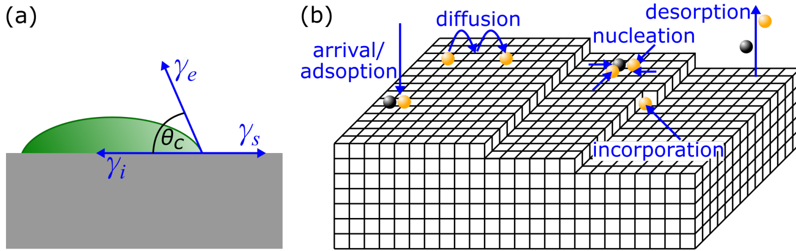


**Fig. 2.4.** (a) Schematic construction of the contact angle for a partial wetting case. (b) Surface processes during crystal growth via epitaxy.

considered for this approach are illustrated in Fig.2.4(b). New atoms arrive with a rate $F$ at the surface and feed a population $n_1$ of single adatoms. Those adatoms can then evaporate again, join an existing stable cluster, form/enlarge a subcritical cluster or complete a new stable cluster (nucleation). Notably, processes involving subcritical clusters are reversible. By considering all these exchange mechanisms of adatoms and assuming monolayer islands as well as negligible evaporation, an analytical solution for the normalized density of stable clusters can be found as

$$\frac{n_x}{N_0} = C\eta \left( \frac{F}{N_0 \nu} \right)^{\frac{i}{i+2}} \exp \left( \frac{E_i + iE_d}{(i+2)kT} \right). \tag{2.10}$$

Here, $C$ and $\eta$ are constants, $N_0$ is the atomic density in the substrate crystal, $\nu$ the effective surface vibration frequency, $i$ the number of atoms in a critical cluster, $E_i$ the free energy change associated with the critical cluster size and $E_d$ the diffusion energy. Details of the derivation can be found in [100].
The main drawback of this atomistic model is that its deterministic character makes it impossible to describe the statistical processes like surface diffusion of the atoms. Complementary models [101][102], which include stochastic behavior, can be applied to fill this gap if necessary.

### 2.2.3 Growth Modes

A lattice-matched layer design is usually preferable from a crystal quality point of view. However, the requirements of advanced bandgap-engineering often makes it necessary to grow materials with different lattice constants on top of each other. This lattice mismatch can be defined as

$$f \equiv \frac{a_{epitaxial} - a_{substrate}}{a_{substrate}}, \tag{2.11}$$

with $a_{epitaxial}$ being the relaxed lattice constant of the newly grown epitaxial crystal and $a_{substrate}$ of the substrate. It significantly influences the growth process and is the origin of a wealth of desirable as well as undesirable effects.
In section 2.2.2, nucleation was described as the first step of heteroepitaxy. In order to successfully deposit thicker layers of crystalline materials, additional influences like long-range ordering have to be considered. Namely, in the case of mismatched deposition, the strain energy in a coherent epitaxial layer increases linearly with its thickness, which influences the deposition process independently of a satisfied wetting condition. Daruka et al.[103] provided a detailed theoretical description of the emerging growth modes in equilibrium. In addition to the traditional Frank-van der Merwe (FM), Volmer-Weber (VW) and Stranski-Krastanov (SK) growth [104], they introduced three distinct modes of islands caused by Oswald ripening (R) [105]. The complete phase diagram is shown in Fig.2.5, supplemented by schematic drawings of all six growth modes. For a lattice mismatch of $f < f_2$, the layer forms in planar FM mode, albeit pseudomorphically strained. After a few monolayers of additional deposition and if $f < f_1$, phase $R_1$ emerges. Here, a WL is accompanied by ripened islands without a stable maximum size. If $f > f_1$, instead, small islands with a defined finite size emerge in phase $SK_1$. For larger lattice mismatch $f > f_2$, stable islands are formed initially on top of the substrate in VW mode. For an even larger mismatch ($f > f_3$), adding more material leads to a ripening phase $R_3$ in which the wetting layer is absent. On the other hand, in the $f_2 < f < f_3$

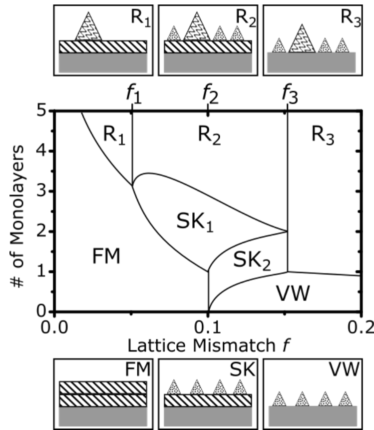


**Fig. 2.5.** Equilibrium phase diagram of depositing a few monolayers of foreign material with and a lattice mismatch $f$ on a substrate. The surrounding panels show a schematic illustration of the respective phases morphology. The brick-structured area represents the wetting layer, the small spotted triangles denote stable islands and the large wave-shaded triangles correspond to ripened islands. (Adopted from [103])

range, additional material forms retroactively into a 2D wetting layer underneath the small islands. Therefore, this phase region is called $SK_2$ and turns into $SK_1$ once the wetting layer is finished. Lastly, if more material is added to the $SK_1$ phase, it transitions into another ripening region ($R_2$), with both stable and ripened islands as well as an underlying wetting layer.

Notably, the discussed model describes the energy-minimized equilibrium case, while experimental layer growth often produces kinetically limited structures (cf. section 3.3). Furthermore, dislocation formation inside larger islands for strain energy reduction has the be taken into account. Nevertheless, phases $SK_1$ and $R_2$ are of special importance for the investigated structures in this work because they allow the fabrication of self-assembled QD layers (see 2.2.6).

### 2.2.4 Metamorphic Relaxation

The minimization of strain energy inside the epitaxial layer is the main driver for the 3D-growth modes discussed in section 2.2.3. Metamorphic relaxation constitutes an additional, competing mechanism of strain reduction. It is most similar to SK growth in that it starts with a pseudomorphic layer. However, the formation of islands at a certain critical thickness is replaced by the introduction of misfit dislocations (MDs).
Fig. 2.6 displays the simplified cubic case of pseudomorphic and metamorphic lattice morphology. In the first case, the mismatched epitaxial layer (blue spheres) emulates the substrates (grey spheres) lattice constant in the x- (and y-) direction. This results in the atomic bonds being squeezed and elongated in the growth direction following the Poisson effect [106]. Since this configuration continuously increases the strain energy when more material is added, it is only preferred for small mismatch and thin layers. At a certain critical thickness $h_c$, the introduction of MDs becomes favorable, which means that an atomic bond is omitted at the strained interface. Through this metamorphic process, the epitaxial layer relaxes and adopts an in-plane lattice constant closer to its inherent value, reducing its total energy. As a consequence, the vertical plane associated with this bond has to be removed from the crystal as well. Naturally, no actual removal of the surplus atoms occurs, but a progressive relocation of individual atoms [107].
An essential concept for describing metamorphically grown dislocated layers is the Burger vector. In combination with the slip plane and the line vector, the Burger vector unambiguously classifies the dislocation type. It can be defined by constructing a closed loop around the (prospective) dislocation position, like ABCDA in the pseudomorphic lattice in Fig. 2.6. The same atom-to-atom jumps (here: 3-down; 4-left; 3-up; 4-right) of this Burger circuit are then transferred to the metamorphic crystal. However, these permutations do not produce a closed loop around the dislocation but end at point $Q$ instead. The

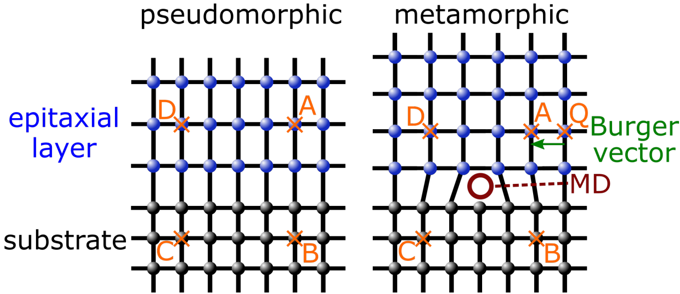


**Fig. 2.6.** Schematic drawing for cubic crystal geometry of depositing a compressively strained heterolayer on a mismatched substrate. A pseudomorphic epitaxial layer mimics the substrates lattice constant for in-plane direction(s) and is stretched in out-of-plane direction. Metamorphic growth reduces strain energy by forming MDs, for which one of the atomic bonds/lattice planes is skipped. Nodes A, B, C, D and Q for the exemplary construction of a Burger vector are drawn in orange.

Burger vector is then defined by the necessary translation $\overrightarrow{QA}$ to close the circuit.
The MD segment creation process is associated with the simultaneous formation of threading dislocations (TDs) protruding into the epitaxial layer and surface roughening. The two most basic of those propagation mechanisms are illustrated in Fig. 2.7(a). In case I, the MD segment originates from a pre-existing TD in the substrate that also protrudes into the strained layer. The upper part of this TD is pushed by lattice stress to glide along the plane that necessitates minimal activation energy for this movement. As labelled, in zincblende crystals, these slip planes are of the $\{111\}$ symmetry. In the wake of this gliding process, an $[0\bar{1}1]$ MD segment emerges at the interface. In case II, a dislocation half-loop forms at the surface and then moves along the slip plane downwards into the layer until it reaches the interface. At this point, it transitions into pure sidewards motion while generating a MD. These glide processes are, in principle, thermally activated. However, the actual impact of growth temperature

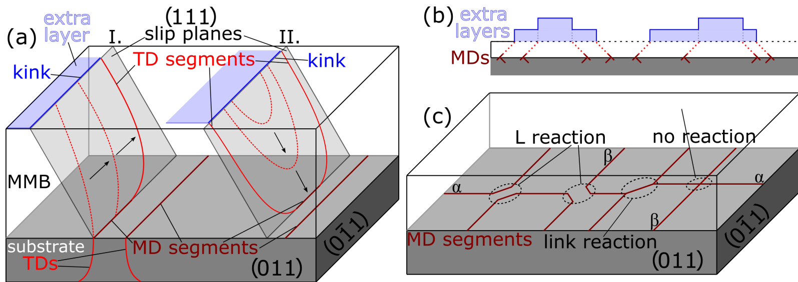


**Fig. 2.7.** Misfit dislocation behavior along ⟨110⟩ directions at the interface between a zincblende heteroepitaxial layer and the substrate. (a) MD segments forming at the interception of the interface and the (111) slip planes. In case I, a TD from the substrate serves as the starting point and is then bent along the slip plane. In case II, a dislocation half-loop originates at the surface and glides into the layer until it forms a MD segment at the bottom of the strained layer. (b) Mechanism for roughening through surplus layers caused by MDs leading to surface kinks for growth nucleation. (c) Different types of interaction between perpendicular MDs, depending on their burger vector. MDs in [011]/[0$\bar{1}$1] directions are labelled $\alpha/\beta$ due to their different dislocation core type.

variations on the strain release is highly dependent on the examined range and the strained layer material properties [108–110]. Additional MD generation mechanisms are, e.g., multiplication at pinning point defects and Hagen-Strunk multiplication [111].

Which strain-release process is prevailing also depends on the epitaxial layer thickness and can be divided into four regimes [112]. As mentioned before, only pseudomorphic growth occurs below the critical thickness. Here, only minimal strain accommodation is realized through surface undulations. Beyond $h_c$, initially, a slow relaxation phase appears in which almost exclusively case I MD generation takes place because it needs the lowest activation energy since it is based on pre-existing dislocations. Due to the insufficient strain release of this process,more strain energy builds up in the layer until more inert mechanisms become active. At this point, first, the fast relax-

ation regime takes place, characterized by the abrupt nucleation of dislocations, followed by rapid propagation of MD segments. Finally, the system transitions into the saturation regime, where the limited residual strain is counteracted by processes like dislocation blocking [113].

These processes are also associated with surface roughening. The kinks (blue lines) in Fig. 2.7(a) are a by-product of the relaxation processes. As displayed in Fig. 2.7(b), they serve as preferred nucleation sites for the growth of new layers and thus produce additional surface steps. Due to the considerable number of those kinks, this leads to a measurable increase of surface roughness for metamorphic layers [114, 115].

Furthermore, especially for high-density networks of perpendicular MDs, interactions between dislocations must be considered. Possible types of reaction for a system of pure 60° nature are shown in Fig. 2.7(c). They depend on the relation between the Burger vectors of the involved MDs [116, 117]. In the case of parallel or antiparallel alignment, two L-shaped dislocations are formed, with their bend adjacent to the omitted intersection. If the two Burger vectors are positioned at a 60° angle toward each other, a link reaction occurs, and the MDs move in concert for a short distance before separating again. Finally, for full perpendicularity, both dislocations pass undisturbed through each other.

Another aspect of metamorphic relaxation in zincblende crystals is that a distinction has to be made between MDs with segments along the two perpendicular directions. As labelled in Fig. 2.7(c), $\alpha$-type MDs run along the [011] direction, while $\beta$-types are aligned to the $[01\bar{1}]$ direction. $\alpha$-dislocations have a group-III atom, e.g., In/Ga/Al, at their core. In contrast, type-V atoms, e.g., As, form the core of $\beta$-dislocations [118]. Furthermore, in undoped InGaAs, $\alpha$-types possess lower activation energy for movement and thus higher glide velocity than $\beta$-types [119]. This circumstance leads, inter alia, to anisotropic macroscopic relaxation for thin or weakly strained layers. However, this glide velocity disparity can be swapped for p-doped layers [120].

#### 2.2.4.1 Relaxation models

There are two main approaches for establishing dislocation models of metamorphic growth. One is force-balancing, and the other is finding energy equilibrium. The first goal of these theoretical considerations is calculating a value for the critical thickness $h_c$.
In the force balance model by Matthews and Blakeslee [121], the glide force induced by strain on a misfit segment is equated to its line tension. For the slip system of zincblende crystals and uniform layer composition, this results in the transcendent equation:

$$h_c = \frac{b(1-\nu\cos^2(\alpha))}{8\pi|f|(1+\nu)\cos\lambda}\left[\ln\left(\frac{h_c}{b}\right)+1\right], \tag{2.12}$$

where $a$ is the lattice constant, $b$ the length of the MD Burger vector, $\nu$ the Poisson ratio and $\alpha/\lambda$ is the angle between the Burger and line vector/perpendicular direction to the intersection of the glide plane and interface. Markedly, one of the central statements is the reciprocal relation to $f$.
On the other hand, People and Bean [122] compared the strain energy in the pseudomorphic layer with that of a dense network of misfit dislocations at the substrate interface. In that case, the transcendent term

$$h_c = \frac{(1+\nu)b^2}{16\sqrt{2}\pi a(1-\nu)f^2}\ln\left(\frac{h_c}{b}\right) \tag{2.13}$$

emerges. Here, the lattice mismatch contributes through a $1/f^2$-factor. Depending on the actual material system, specifically the examined range for $f$, both approaches have shown agreement with experimental data [123–128], with the force-balance model being generally more widely accepted overall.
The next step in modelling is typically predicting the total relaxation $R$ depending on the layer thickness $h$. Building on the force-balance calculations by Matthews and Blakeslee, Dunstan et al. [129] have proposed the relation

$$R = 1 - \frac{h_c}{h}. \tag{2.14}$$

They have furthermore shown that this dependency is supported by experimental data but exhibits deviations in the low as well as the high thickness regime [130, 131].
Based on energy-balance considerations, Marée et al. [132] have obtained

$$R = 1 - \sqrt{\frac{h_c}{h}} \tag{2.15}$$

for the evolution of plastic relaxation. Here, experimental data from Drigo et al. [133] showed good agreement. Additionally, Bellani et al. [134] have found a much better matching of their data for InGaAs to this model than for the force-balance counterpart.
Further and more precise predictions, especially for non-uniform metamorphic layers, are available through more recent advanced numerical simulation models like, e.g., Ref. [135].

### 2.2.5 Metamorphic Buffer Growth

Control over the metamorphic relaxation process allows intentional alteration of the lattice constant. The associated potential given by this design flexibility is typically utilized by growing a dedicated section in which the relaxation takes place, a so-called metamorphic buffer (MMB). Since it provides different growth conditions than the wafer material for all subsequent structures, it is sometimes also dubbed a "virtual substrate." However, compared to a typical substrate, possible feedback in terms of, e.g., strain from layers in the active region into the MMB has to be considered much more strongly. Achieving the desired transition of the lattice constant and simultaneously maintaining a high crystal quality is a challenging task.

#### 2.2.5.1 Content grading

Staying with the most straightforward uniform composition design limits the maximum possible lattice transition due to the onset of 3D growth modes (see section 2.2.3). Employing content grading

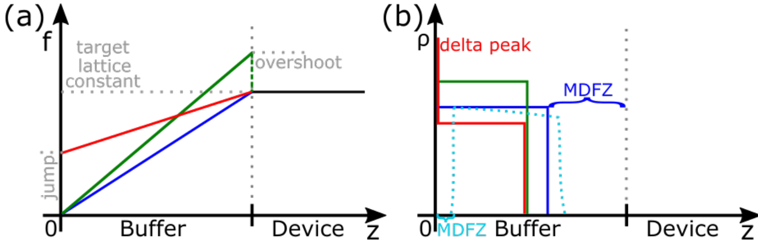


**Fig. 2.8.** (a) Content grading designs based on a linear function with the same target lattice constant for the device layers. Basic linear grading is plotted in blue. A design with an additional overshoot is shown in green. A grading function featuring a jump step is displayed in red. (b) The respective misfit dislocation cross-sectional area density ρ over the z-position of the three designs. The MDFZ of the simple linear case is marked.

instead can also facilitate control over defect generation and surface roughness [136, 137]. The concepts of critical thickness, MDs and TDs are all still valid for the graded case but must be re-evaluated in their manifestation.

In the general case of zincblende and a (100) substrate, $h_c$ can be calculated via a force balance model by equating glide and line tension, including a correction due to the initial MD possibly being formed at a distance $z_c$ from the interface. This results in the term

$$\int_{z_c}^{h_c} f(z)dz = \frac{b(1-\nu\cos^2\alpha)}{8\pi(1+\nu)\cos\lambda}\left[\ln\left(\frac{h_c-z_c}{b}\right)+1\right], \qquad (2.16)$$

with the notation from section 2.2.4.1. Notably, the correction of the MD formation location is not trivial but a main qualitative difference to the constant case. For a uniformly mismatched layer, all MDs are located at the substrate/MMB interface, while a graded MMB shows a density distribution throughout its thickness. This distribution has been calculated for the general case for equilibrium by Bertoli et al. in Ref. [138] and for the kinetic limit by Kujofsa et al. in Ref [139]. Some

of the features resulting from these kinds of calculations, as well as two advanced design techniques are schematically illustrated in Fig. 2.8 for the example of linear grading. The basic linear grading design in blue starts matched to the substrate and then steadily increases the lattice constant up to the target for the device layers. According to the analytical calculations by Tersoff in Ref. [65], this approach results in an approximately uniform MD areal density within a large section of the MMB, as illustrated in Fig. 2.8(b). Furthermore, a misfit dislocation free zone (MDFZ) is generated adjacent to the device layer at the top of the buffer. Based on these results, experimental data [140] as well as numerical calculation [138] reveal three primary corrections to this model. First, an additional thin MDFZ emerges at the bottom of the MMB close to the substrate interface. Second, $\rho$ is not constant but instead slightly tapered towards the end. Third, the relaxation region extends further to the MMBs top. These corrections are illustrated in the dashed light blue line.
The drawbacks of this simple linear grading are a relatively slow relaxation with respect to thickness and significant residual strain in the device layers, which reduces optical and structural quality [141]. Fig. 2.8(a), green/red shows two common design enhancements to counteract these weaknesses. Utilizing a content overshoot can provide better lattice matching and, consequently, a fully relaxed device section. Additionally, the steeper grading produces a higher MD density as well as a broadened upper MDFZ compared to the base case (cf. Fig. 2.8(b)). Furthermore, inserting a content jump at the substrate interface facilitates faster relaxation. This design is accompanied by an especially high MD density at the interface. Moreover, the significant amount of strain relaxed by these dislocations results in a much narrower relaxation zone with a reduced MD density level.
Compared to the MD case, much less literature is available for modelling the TD behavior dependency on linear grading and specifically growth rate and temperature. Nevertheless, Fitzgerald et al. established a dislocation dynamics model that shows good agreement with experimental data of an InGaP MMB on GaP substrate [142]. They

found the following expression for the final steady-state TD density $D_{TD}$:

$$D_{TD} = \frac{2gC_f}{bC_1} \exp\left(\frac{U}{k_B T}\right), \tag{2.17}$$

with $g$ being the growth rate, $C_f$ the grading rate $\Delta C/\Delta z$, $b$ the length of the Burger vector, $C_1$ a material dependant constant, $U$ the glide activation energy and $T$ the temperature. Two key conclusions can be drawn from this equation. First, the TD density increases linearly with the growth rate and the grading slope. Second, there is an exponential reciprocal dependency of $D_{TD}$ on deposition temperature. Notably, the model is limited to cases with unimpaired dislocation glide and its validity diminishes once, e.g., pinning effects are considered [143, 144].
The discussed characteristics, i.e., critical thickness $h_c$, MD/TD distribution (specifically MDFZ dimensions) and residual strain, vary depending on the exact MMB grading design. Nevertheless, the outlined general behavior is mostly transferable. For the case of an InGaAs MMB, calculation and experimental data of step-graded MMBs can be found, e.g., in Refs. [66] and [145]. Various sub- and superlinear gradings are discussed, e.g., in Refs. [75, 77, 146] and [76].

#### 2.2.5.2 Dislocation coalescence/annihilation

In the previous sections, it has been established that TDs are an inseparable part of MD generation and, thus, relaxation. TD density, however, is subject to further effects beyond the initial MD segment length and total lattice constant transition. Most importantly, TDs can react with each other once they are in close spacial vicinity. The two categories for these interactions are coalescence and annihilation. In the former, a pair of dislocations with different Burger vectors combine into a single TD, reducing the overall net number by one. In the special case of antiparallel Burger vectors, complete annihilation can occur, removing both dislocations. The efficacy of these interactions depends, on the one hand, on the current dislocation density and, on the other hand, on their mobility. In turn, lateral movement of the

TDs is moderated by the following main effects.
The first is that, during active plastic relaxation, MD segments are elongated, dragging their associated TDs with them, as has been discussed in Fig. 2.7(a). Especially for high-strain situations and, consequently, large numbers of gliding TDs, this can lead to a large number of interactions. However, these mechanisms are part of the overall process of generating the final dislocation network and can hardly be resolved from, e.g., multiplication events. Nevertheless, these interactions are mostly responsible for the maximum TD density rarely exceeding the lower $10^9\,\mathrm{cm}^{-2}$ range even for highly mismatched materials [147]. Once a state of almost complete relaxation is reached, major effective movement can be directly derived from the natural inclination of the dislocations along their slip plane. Consequently, a predictable TD density reduction with $\propto 1/h$ dependency on layer thickness emerges [148].
Finally, filtering techniques like strained-layer superlattices can be utilized. These structures actively increase the dislocation mobility and reaction probability within thin layer dimensions and for low densities.

#### 2.2.5.3 Temperature grading

Temperature considerations for MMB growth are often limited to finding and setting constant, optimal deposition conditions for, e.g., reducing roughness or TD density [149, 150]. One step further is separate optimization for buffer and device layer [151]. However, grading the growth temperature within the MMB should facilitate additional control, but only very sparse investigations have been performed following this approach.
Kujofsa et al. [152] have studied the impact of different grading profiles on the crystalline properties of mismatched ZnSe on GaAs substrate via a plastic flow model. One effect they found is that for the same start and end values, changing the temperature convex-up generated a higher MD density and relaxation than the convex-down counterpart. Furthermore, keeping the final temperature fixed while

varying the initial value similarly accelerated the relaxation process. In an analogues fashion, the TD density is suppressed by designs with low average temperature.
In conclusion, managing the thermal budget during the growth of metamorphic layers can significantly influence key properties but needs further examination.

### 2.2.6 Self-Assembled Quantum Dots

Self-assembled QDs can be fabricated using the $SK_1/R_2$ growth modes discussed in section 2.2.3. This approach can provide high-quality dislocation-free emitters [153] while omitting any pre-patterning of the substrate [154].
Using a QD material with a sufficiently larger lattice constant but a smaller band gap than the surrounding matrix material, like InAs on a GaAs substrate, produces inclusions with proper quantum size, i.e., the nanometer range. These structures can be distinguished from simple islands by the strength of their 3D confinement potential resulting in discrete states. More precisely, two conditions have to be fulfilled. On the one hand, the extension of the material inclusion has to be small enough to reach the length scale of the involved electrons/holes deBroglie-wavelength. On the other hand, in order to possess bound states, the QDs radius $R_0$ and confinement depth $\Delta E_{c,v}$ must stay within a defined ratio. In the simple finite potential-well-model [155], for example, this is given by

$$R_0 \geq \frac{\pi\hbar}{\sqrt{8m^* \, \Delta E_{c,v}}}, \tag{2.18}$$

where $m^*$ is the effective particle mass, setting a lower bound for the QD size.
A schematic illustration of such a SK growth-mode based QD is displayed in Fig. 2.9(a). The discrete bound states are labelled, analogous to their counterparts in atoms, with s-shell for the ground state, p-shell for the first excited state, etc.. A bound electron and hole pair is called an exciton ($|X\rangle$). These states can be generated optically.

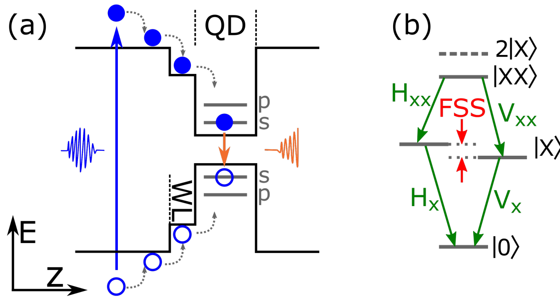


**Fig. 2.9.** (a) Schematic of a QD with discrete atom-like energy states emerging by embedding a SC material with a small band gap into a matrix with a larger one. Excitation can occur via an above-band photon generating an electron-hole pair that can relax into the potential well. Recombination emits a single photon with defined energy.
(b) Double excitation diagram of a QD. The energy of the biexciton is slightly lower than twice the exciton energy. Asymmetry of the QD can generate a FSS of the originally degenerate relaxation paths.

E.g., for the depicted case, a (laser) photon with higher (above-band) energy than the matrix material generates an electron-hole pair that then relaxes into the QD states. Subsequently, recombination sends out a single photon with a defined wavelength. More sophisticated excitation schemes have been shown to allow more precise control over state population [156–160]. Alternatively, an exciton can be created by electrical charge injection utilizing the SC-nature of the matrix material. This route has the advantage of simultaneous stabilization and control of the charge environment [161]. In any case, to address single QDs, a sufficiently low area density is essential [162].
Markedly, the s-shell ground state can be occupied by exactly two electron-hole pairs due to spin degeneracy. Special attention has been paid to this biexciton ($|XX\rangle$) configuration because of its potential to create entangled two-photon emission [163]. The corresponding energy scheme is drawn in Fig. 2.9(b). The first important aspect is that the energy of the biexciton is slightly lower than for two separate

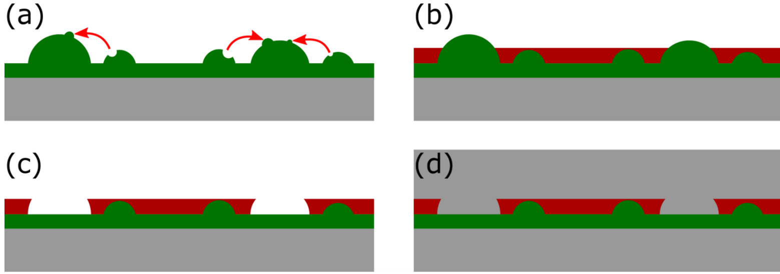


**Fig. 2.10.** Consecutive steps of QD shape manipulation after initial SK growth phase formation. The substrate is drawn in grey. QDs and WL are shown in green. The annealing cap is displayed in red.
(a): Oswald ripening once material supply is stopped. (b): QD layer partly covered with an annealing cap. (c): Large islands are desorbed by thermal annealing. (d): Completed matrix after capping layer deposition.

excitons due to additional binding energy from Coulomb interaction [164]. Furthermore, two paths are available for the cascaded radiative recombination through $|X\rangle$ with either $M = +1$ or $M = -1$. For complete energetic degeneracy of these excitonic states, polarization-entangled photon pair can be described in the linear basis as

$$|\Psi^+\rangle = \frac{1}{\sqrt{2}} \left( |H_{XX} H_X\rangle + |V_{XX} V_X\rangle \right), \tag{2.19}$$

representing a maximally entangled Bell state. However, the necessary degeneracy can be lifted by breaking the rotational symmetry of the QD. Either growth-related elongation along a preferred crystalline axis or inhomogeneous composition due to diffusion causes this kind of asymmetry [165]. This generates a fine-structure splitting (FSS) of the $|X\rangle$ states establishing "which-way" information critically diminishing the entanglement [166]. Therefore, avoiding any asymmetry/FSS is one goal of QD fabrication.
All in all, to achieve highest-quality single-photon emission with maximum applicability, QD emitters must be meticulous engineered in terms of size, shape and density. Apart from the typical MOVPE

growth parameters based on temperature, fluxes and time, additional parameter space is available for QD deposition. Several prominent examples can be explained based on the four steps illustrated in Fig. 2.10. Step (a) describes the ripening during a growth interruption after the material supply is stopped but before covering the QDs. As the previously mentioned $SK_1/R_2$ growth modes describe the equilibrium state, they can basically never be fully realized for InAs QDs in an (In)GaAs matrix fabricated via MOVPE. In addition to diffusion, adsorption and desorption processes are usually unbalanced. This effect is especially prominent for In-atoms. The material redistribution can be described by Oswald and Ostwald-like ripening [167, 168].
In any case, control over the ripening time allows additional flexibility for QD design. Furthermore, a dedicated deposition temperature $T_{QD}$ is typically utilized, which is distinctly different from the optimized value for matrix layer growth [169]. Consequently, a temperature adjustment phase is necessary before a full-thickness capping layer can be deposited. In order to protect and stabilize the QD structure, this step is often prepared via a thin annealing cap (AnnCap) grown at $T_{QD}$, as shown in panel (b) [170]. Furthermore, it can be combined with a dedicated annealing step at possibly even increased temperature relative to optimal matrix growth. As shown in Fig. 2.10(c), this procedure can eliminate larger islands, provided the AnnCap material has higher thermal stability than the QD material. This is the case for In(Ga)As QDs with high Indium content in an (In)GaAs matrix. In summary, this technique allows control over the maximum QD height in the embedded layer, as displayed in step (d), through setting the AnnCap thickness.

### 2.2.7 Distributed Bragg reflector

The distributed Bragg reflector (DBR) is a functional structure that can be monolithically integrated as a mirror into a device. A DBR is based on constructive interference from Fresnel reflection at interfaces between layers with different refractive indices. For SC materials,

maximum reflectivity can be calculated with the equation [83]:

$$R = \left[ \frac{n_0 \cdot (n_H)^{2p} - n_H \cdot (n_L)^{2p}}{n_0 \cdot (n_H)^{2p} + n_H \cdot (n_L)^{2p}} \right]^2 , \tag{2.20}$$

where the refractive indexes are $n_0$ for the originating medium and $n_H/n_L$ for the high/low optical density semiconductor, and $p$ is the number of layer pairs. For the devices in this thesis, $n_0$ can be either air or InGaAs for the top and bottom DBR respectively. A comparatively thick structure must be deposited to reach high reflexivity (>99 %). For monocrystalline growth techniques like MOVPE, this requires (almost) lattice-matched materials with sufficiently large refractive index contrast. This prerequisite is prominently fulfilled by the binary AlAs and GaAs materials. Consequently, AlAs/GaAs DBRs are extensively used in commercial devices like, e.g., Vertical-Cavity Surface-Emitting Lasers [171]. Similar systems like InP/InGaAlAs are much more challenging to grow with comparable high quality due to the quaternary nature of the latter material and the many necessary arsine-phosphine transitions [172].

## 2.3 Methods

The measurement techniques that were employed to characterize the sample structures' crystalline and optical properties are briefly explained in this section. Furthermore, the machine's producer and the specific device versions are stated. Finally, particular sub-methods, utilized options and filters are declared.

### 2.3.1 Atomic force microscopy

Atomic force microscopy (AFM) is an effective tool for attaining information about surface morphology. It uses a cantilever with a fine tip to scan over the sample. The arising forces between the tip and surface will then bend the cantilever (Contact Mode) or influence its resonance frequency (Tapping Mode). This information is then

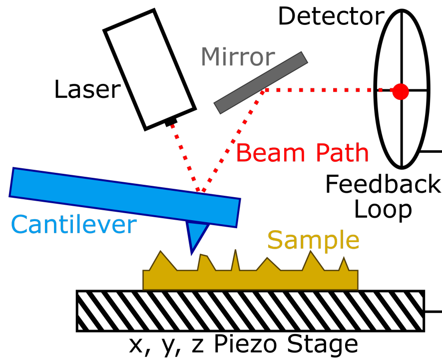


**Fig. 2.11.** Schematic drawing of AFM measurement principle. The laser beam is reflected on top of the cantilever tip. The feedback loop controls the distance between tip and sample according to the detector signal and depends on the measurement mode.

analyzed to determine the surface height at any point in time and fine scanning of an area results in a full profile. From this data, the RMS roughness can be calculated by determining the deviation of each point from the mean surface level ($R_q$). Other properties like ductility, composition and magnetization can also be accessed but were not required in this work.
All AFM data shown in chapters 3 and 4 were recorded with a Bruker Dimension Icon ©. Post-processing is performed with the Nanoscope Analysis 1.5 software. Three consecutive filters were applied for all scans and resulting roughness data: 1st order Flatten, 2nd order Plane Fit and Clean Image with Remove Streaks turned on and Remove Peaks turned off. All scan images are depicted with the horizontal axis being aligned to the intersection of the surface with the Ga/In-facets ($[011]/[0\bar{1}\bar{1}]$) and the vertical axis being aligned to the respective As-facets ($[0\bar{1}1]/[01\bar{1}]$).

### 2.3.2 High-resolution X-ray diffraction

High-resolution X-ray diffraction (XRD) is a non-destructive method for investigating crystalline or similar regular structures. The technique can directly depict the reciprocal lattice, which can then be used to draw conclusions regarding the real-space lattice.
The utilized effect is the fulfillment of the Bragg condition for EM-waves at a specific set of parallel crystalline planes. The basic geometric construction is shown in Fig. 2.12(a) and leads to the Bragg equation

$$2d\sin(\theta) = n\lambda, \tag{2.21}$$

with $d$ as the distance between the planes, $\theta$ the incidence angle, $n$ as an integer and $\lambda$ as the wavelength of the incoming beam. For the typical $d$ of (SC) crystals, this results in $\lambda$ being in the X-ray range. Furthermore, for a 3D crystal lattice containing various sets of parallel planes, this leads to a full diffraction pattern. Depending on the relevant sought information and the investigated material, there is an extensive range of available specialized XRD-based techniques described, e.g., by Bertram Warren in Ref. [173]. The specific methods and the machine used in this work are outlined in the following.
Fig. 2.12(b) displays the core components of the Rigaku SmartLab © device. It features a 9 kW rotating anode X-ray source, a 5-axis goniometer, and can be equipped with the D/teX Ultra 250 © linear detector with 0.3 ° omega angle scan capabilities. Incidence, as well as receiving beam, can be refined by a variety of optical options. E.g., a 4-times crystal channel monochromator was used for all data in this work.
The primarily utilized method is reciprocal space map (RSM) measurement, which allows analysis of tertiary materials with undefined composition and relaxation state, and is thus ideal for metamorphic InGaAs. Its main drawback of extended scan time can be reduced by using linear detectors. As displayed in Fig. 3.17 in section 3.4, this technique produces an intensity map, which directly corresponds to a sector of reciprocal space. By referencing all peak positions to the bright, well-defined GaAs substrate signal, lattice constants can

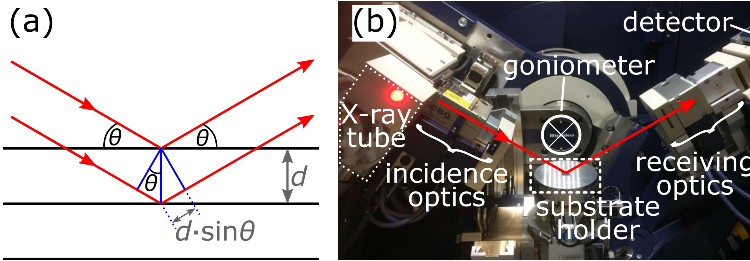


**Fig. 2.12.** (a) Geometric construction of Bragg condition for atomic crystal lattice layers with distance $d$. The length difference between the two red paths is marked and labelled depending on the incidence angle.
(b) Picture of Rigaku XRD device with labelled components. The respective beam path is drawn in red.

be precisely defined. The RSM around the [400]-reflection allows crystalline tilt measurement through the slight offset in $q_z$ direction relative to the GaAs peak, as explained in Ref. [174]. This data is then used for tilt correction of the [422]-map, which results in a well-defined position-relaxation relation of the strained-layer peaks. By evaluating two perpendicular [422] directions, one can then account for the Poisson deformation and calculate the composition of the tertiary material, in this case, $In_xGa_{1-x}As$.
All RSM data in this work is recorded around the GaAs peak via the D/teX Ultra 250© detector. For structures with high indium content (>24 %), two adjacent map pieces are collected in order to cover sufficient reciprocal space area. The data is then loaded into the Rigaku 3D Explore Version 3.1.3.0 software. For more reliable peak position determination, it is then processed via the Smooth Data operation with a smoothing factor of 10 and exported into .txt-files. The peak identification, as well as the resulting composition and relaxation analysis, are executed via the self-made software displayed in appendix 6.8.
The second relevant method is X-ray reflectometry based on total reflection effects. Therefore, a sweep around grazing angles of incidence

is performed. Hereby, surface and interface roughness produce a faster decay of the total signal. This behavior can be quantitatively analyzed and hence supplements AFM and SEM data. More importantly, a heterogeneous layer structure generates interference oscillations with a defined wavelength from which the film thickness can be calculated. The analysis is performed via the Rigaku GlobalFit software.

### 2.3.3 Electron microscopy

Electron microscopy is a valuable approach to resolve structures beyond the diffraction limit of traditional photon-based measurements. It is categorized into either detecting and evaluating reflected/dispersed signal within the incidence hemisphere called scanning electron microscopy (SEM). Alternatively, signal collection can focus on the transmitted side for transmission electron microscopy (STEM). In any case, deflection and diffraction of the primary electrons as well as energy loss can be combined with analyzing the properties of secondary emission to enable various contrasts based on, e.g., element composition and strain.

### 2.3.4 Photoluminescence

Photoluminescence (PL) measurements are a vital cornerstone to evaluating the properties of QD/MMB structures. The basic principle, as displayed in Fig. 2.13, is to excite the sample optically via an attenuated laser and collect its emission in a spectrometer. The necessary light paths are moderated by a central beam splitter plus a filter to block the excitation signal from distorting the detection.
Especially when characterizing QD samples, one often distinguishes between ensemble-PL and micro-PL (μ-PL). The former examines emission within a spot size in the millimeter range using a simple lens as the focussing element. The method can thus provide averaged information about, e.g., the overall wavelength and brightness behavior of a sample. In contrast, in micro-photoluminescence (μ-PL), the detection spot size is restricted to approximately 2 μm diameter via a

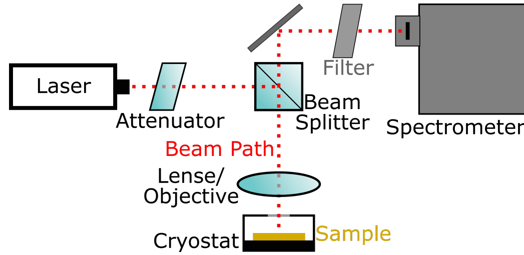


**Fig. 2.13.** Schematic drawing of PL measurement setup. Excitation and detection beam paths impinge on the beam splitter. The sample can be cooled to 4 K in the cryostat. Ensemble- and μ-PL observations differ in the optical element focussing the beam onto the sample.

microscope objective. This allows to address single QD emitters and attain their properties.
Different excitation modes differ in their wavelength and time profile. Considerably higher energy than the examined materials bandgap is used for above-band excitation. This is a quick and straightforward approach, but internal charge carrier relaxation and diffusion channels are indiscriminately active, which can influence the investigated transition. Therefore, more sophisticated excitation schemes typically use tailored/resonant photon energy [159, 160]. Moreover, the laser can be operated in a continuous-wave (cw) or pulsed fashion. Here, the latter facilitates the observation of time-sensitive effects. Finally, supplementary optical elements can be inserted into the beam path to modify the setup according to the desired measurement scenario. Various setting combinations are employed in chapters 3 and 4, and are labelled accordingly. Additional details on the distinct utilized methods can be found in [175].

## 2.3.5 Photolithography

Heteroepitaxy is often combined with photolithography steps if enhanced complexity is needed for device functionality. The multi-step

process starts with the thin, uniform application of a photosensitive resist, typically by spin-coating. This film is then exposed to UV light or an electron beam. At this step, the desired pattern is transferred through either a shadow-mask or direct control and scanning of focussed radiation. Depending on whether a positive or negative type resist is used, the illuminated area is then either dissolved or solely remains after the chemical development. Subsequently, additional material is deposited onto the sample for bottom-up techniques. Alternatively, the top-down counterpart means structures are etched into the existing layer material. In any case, only the unprotected areas provide an accessible surface for the process. Finally, the resist is completely removed, and the structured sample is now available for further fabrication steps.

Details on the photolithography and subsequent etching of metamorphic InGaAs can be found in [176] and [177].

Chapter 3

# Thin-Film Buffer

Previous results of C-band emission from single In(Ga)As QDs on the GaAs platform have primarily been achieved using a linear MMB [80, 82]. This design and a layer with constant composition are likewise the most common approaches for MMBs in applications such as high electron mobility transistors [178] and multi-junction solar cells [179]. The slow strain release inside these layers facilitates control over surface roughness and dislocation density [136], at the cost of significant layer thickness, typically several micrometers. However, one of the strengths of using GaAs substrates is the ability to grow almost lattice-matched heteroepitaxial AlGaAs layers. This feature allows flexible band-gap engineering, varying the refractive index and inserting chemically diverse layers to produce structures like DBRs, barrier/cladding [180] and etch-stop layers [181].
In order to retain this advantage, it is necessary for many photonic structures, e.g., micro-pillars, to place the MMB inside the cavity region. Therefore, to achieve the best results for important quantities like the Purcell enhancement, the total thickness of MMB plus capping layer has to equate to an optical length of a single $\lambda$ at 1550 nm. Notably, the InGaAs matrix must have an indium concentration of around 28 % to provide sufficient strain reduction [82], which results in a geometrical length of approximately 440 nm [182]. This means only 220 nm are available for the MMB thickness since the QDs are typically placed in the antinode at the center of the cavity. Furthermore, the surface roughness has to be sufficiently low to allow high-quality

QD deposition, undisturbed excitation/extraction efficiency and compatibility with nano-structuring techniques.
In conclusion, a novel MMB design has to simultaneously provide an efficient transition of the lattice constant and high crystalline quality.
Parts of this chapter are published in [183].

## 3.1 Relaxation-optimized buffer design

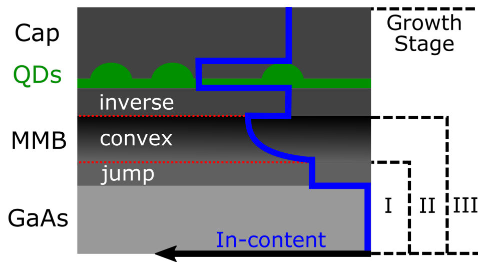


**Fig. 3.1.** Schematic drawing of the jump-convex-inverse InGaAs MMB design for InAs QDs emitting at 1550 nm. The indium content depending on thickness, is marked in blue. The three consecutive stages of growth optimization are labelled I, II and III. (Adopted from [183])

As discussed in section 2.2.4, the formation of misfit dislocations and, therefore, the alteration of the lattice constant is driven by strain energy. Consequently, a MMB design with the goal of minimizing the total thickness has to maximize the strain at every point inside the layer. In the case of a content graded InGaAs MMB on a GaAs substrate, this means consistently using the maximum permissible indium content without inducing 3D growth. The proposed design for this purpose, which will be examined in this work, is shown in Fig. 3.1. It starts with a jump of the indium content, representing the maximum possible value that stays within the limits of the FM mode. Furthermore, the thickness of this layer is set to the minimum value necessary to induce plastic relaxation (i.e., slightly above the

critical thickness). Once this metamorphic process starts to increase the lattice constant, the indium grading can also be initiated without generating 3D structures. Following this logic, a convex-up function, in analogy to the metamorphic relaxation curve [114], is employed as the steepest permissible grading profile. This grading is furthermore set to the steepest rate that still produces sufficient crystalline quality. Moreover, an overshoot of In content ensures efficient relaxation by avoiding the stagnant saturation regime (see section 2.2.4). Finally, the maximum indium content depends on the composition of the inverse layer because it has to be adjusted to allow a lattice-matched deposition. In turn, the indium content of the inverse layer is calibrated to provide the correct amount of strain reduction to enable the deposition of InAs QDs emitting around 1550 nm. Capping is realized via an InGaAs layer with the same indium content as the inverse step. This extremely efficient plastic relaxation in terms of total layer thickness is assumed to be associated with a high density of short MD segments, which are, in turn, accompanied by a large number of initial TDs [147]. However, as discussed in section 2.2.5.2, this should also trigger equally fast annihilation to bring the TD density back into a manageable range. Furthermore, the front-loaded strain introduction should generate a proportionally thick MDFZ [76]. Finally, the 0D-nature of the QD emitters constitutes a considerable advantage for dislocation robustness. All in all, these effects make the realization of sufficient crystalline quality for high-quality single-photon emission feasible, provided carefully optimized growth conditions are implemented.

## 3.2 Growth parameter optimization

Values like indium content, thickness and grading progression mentioned in the previous section 3.1 have to be meticulously calibrated, and the growth parameters have to be adjusted for the best results in terms of crystal quality. This optimization was performed in three consecutive growth stages that are labelled I, II and III in Fig. 3.1:

First, only the jump layer is deposited, then the grading section is added, and finally, the whole structure, including the inverse layer, the QDs and the capping layer is grown.
Surface roughness was used as the main criterion for the optimization because it prominently influences QD growth, excitation/extraction efficiency and compatibility with nano-structuring techniques. Moreover, the RMS value is readily available via simple AFM measurement. In an ideal case, when studying the impact of a particular growth parameter, all other parameters are kept constant. Nevertheless, due to strong interdependences, unintentional drifts during a test series are expected. In order to counteract this effect, sensible extrapolation can be used (e.g.: precursor flux↔layer thickness↔growth rate). Alternatively, a separate calibration can be performed by utilizing characterization measurements for feedback. However, this necessitates additional samples produced by separate growth runs for each final data point and is thus associated with a significant expenditure of resources. This method was therefore omitted for all cases in which the impact of this error source on the implications of a test series was negligible (e.g., the outer data points of a test series with a clear trend). Naturally, the respective resulting error is discussed for each data set.
Furthermore, this section demonstrates the main path toward a stable growth recipe for the jump-convex-inverse MMB. Subsequent investigations of its stability against growth parameter changes and further techniques to improve the crystalline quality are discussed in section 3.5.

### 3.2.1 Jump layer

As specified in the design, the main aims of calibrating the jump layer were to find the maximum permissible indium content and the minimum thickness for the onset of plastic relaxation. Additionally, finding the optimal growth parameters to minimize surface roughness was mainly pursued in this step because an ungraded InGaAs layer constitutes the simplest system for these calibrations, allowing to

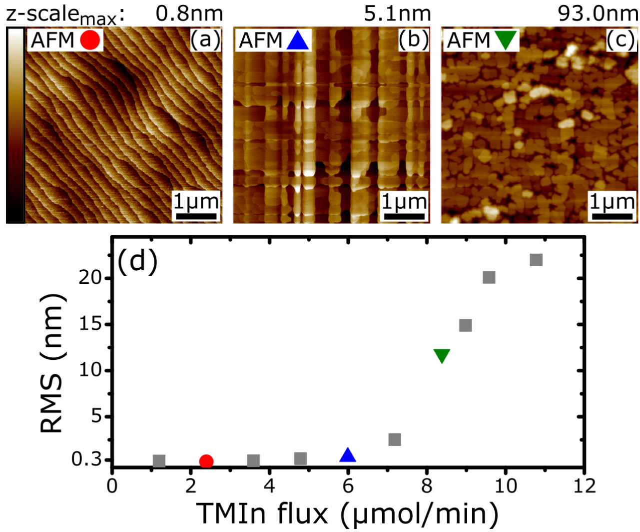


**Fig. 3.2.** AFM analysis of 50 nm thick InGaAs layers with varying indium content grown at 710 °C. Graph (d) shows the behavior of the surface roughness depending on the TMIn flux. AFM scans (a), (b) and (c) exemplify the topography at selected values. (Graph (d) reproduced after [183]

draw direct conclusions about the impact of different growth parameters. Notably, the considerable interdependency of these parameters necessitates multiple iterations for each one.

#### 3.2.1.1 High temperature 2D-3D transition

The default growth of high-quality GaAs on the utilized MOVPE-machine was chosen as the starting point, namely a temperature of 710 °C, a TMGa flux of 20.8 µmol/min, and an $AsH_3$ flux of 2973 µmol/min. On this basis, 50 nm thick layers of InGaAs were grown by adding varying amounts of TMIn. As shown in Fig. 3.2(d), for low fluxes ($< 5$ µmol/min), the surface roughness of those layers

stays at approximately 0.3 nm, which is typical for epitaxial GaAs. Consequently, the step-flow surface topography of the representative AFM scan Fig. 3.2(a) implies a pseudomorphic growth mode. In contrast, for 6 µmol/min, the surface exhibits the typical cross-hatch structure associated with metamorphic relaxation (cf. Fig. 3.2(b)) [114]. For further increase of the In-flux, a sharp rise of the RMS indicates a transition towards a 3D-growth mode underlined by the grain-like topography in the respective AFM scan Fig. 3.2(c). Moreover, XRD measurements determined an indium content of 16.2 % for the 4.8 µmol/min sample and 21.3 % for the 6.0 µmol/min sample. In contrast, the data of the 7.2 µmol/min sample could not be evaluated due to insufficient signal-to-noise ratio caused by low crystalline quality. This means that the transition from 2D to 3D growth occurs around 1.5 % lattice mismatch, which is considerably lower than the literature specifying a possible mismatch of up to $\approx 2\,\%$ [184]. However, this transition is governed by surface diffusion and is thus substantially growth parameter dependent [185]. Therefore, further investigations aim to extend this boundary and find a sensible upper limit. For this purpose, a TMIn flux of 6 µmol/min was selected as the reference value.
Furthermore, in order to work with a layer thickness that shows a high contrast for this roughening effect, the surface behavior around the 2D-3D transition of 30 nm, 100 nm and 200 nm thick InGaAs layers, in addition to the previous 50 nm, were examined. The results are shown in Fig. 3.3. The absolute difference in RMS between using 4.8 µmol and 7.2 µmol of TMIn flux is largest for 100 nm thick layers ($\Delta\mathrm{RMS}_{100} = 3.64$ nm), compared to 50 nm ($\Delta\mathrm{RMS}_{50} = 2.05$ nm), 30 nm ($\Delta\mathrm{RMS}_{30} = 1.52$ nm) and 200 nm ($\Delta\mathrm{RMS}_{200} = 2.46$ nm). Therefore, 100 nm was used for the thickness of the InGaAs layers featured in the following samples.
**Error sources:** Inaccuracies in depositing precisely 30/50/100/200 nm thick layers for the full indium composition range has to be mentioned as a source of error in the evaluation of Fig. 3.2 and Fig. 3.3. This would lead to inconsistencies in the relaxation state and thus RMS values. Therefore, XRR was utilized as a method for thickness deter-

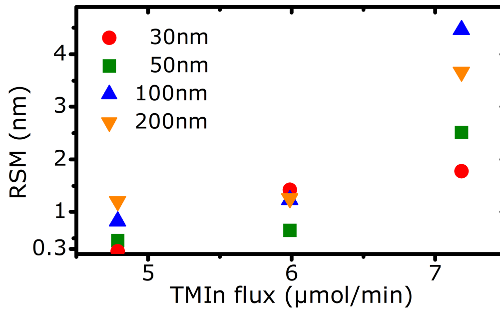


**Fig. 3.3.** Evaluation of the increase in surface roughness of InGaAs using a TMIn flux around 6 µmol/min for different thicknesses at a growth temperature of 710 °C. (Reproduced after [183])

mination (see Appendix 6.1) but was limited to the range between 3.6 µmol/min and 6.0 µmol/min. For lower indium contents, there was insufficient contrast between the GaAs substrate and the InGaAs layer, while layers with higher indium content had inadequate crystalline quality. The XRR data for the three accessible samples with a nominal thickness of 50 nm revealed a large spread of 45 nm to 52 nm in their actual value. Nevertheless, a possible regrowth of these samples with adjusted growth rates was omitted due to the clear visibility of the 2D-3D transition in Fig. 3.2, which is robust even against a 10 % error of the RMS values. On the other hand, this adjustment was implemented for the nominal 30/100/200 nm layers depicted in Fig. 3.3, with the low and medium flux samples being directly calibrated and the 7.2 µmol sample being extrapolated accordingly. This resulted in a deviation in thickness of less than 1 % for these samples according to respective XRR measurements.

#### 3.2.1.2 Approaches of controlling the surface diffusion

In MOVPE, there are four main parameters for controlling the surface diffusion: growth rate, temperature, V/III ratio and pressure [186].

**Table 3.1.** Investigation of different growth rates for 100 nm thick InGaAs layers grown at 710 °C.

| # | TMIn flux | TMGa flux | RMS | $In_x$ |
|---|---|---|---|---|
| 1 | $6.0\,\frac{\mu mol}{min}$ | $20.8\,\frac{\mu mol}{min}$ | 1.26 nm | 21.4 % |
| 2 | $9.0\,\frac{\mu mol}{min}$ | $31.2\,\frac{\mu mol}{min}$ | 1.23 nm | 21.1 % |
| 3 | $3.0\,\frac{\mu mol}{min}$ | $10.4\,\frac{\mu mol}{min}$ | 0.91 nm | 18.1 % |
| 4 | $1.5\,\frac{\mu mol}{min}$ | $5.2\,\frac{\mu mol}{min}$ | 0.65 nm | 12.4 % |

This evaluation will mainly be performed by monitoring the RMS as a measure of 3D growth. Furthermore, surface roughness, respectively its minimization, is also an important parameter for QD growth, excitation/extraction efficiency and the applicability of nano-structuring techniques.
The pressure parameter will be excluded at this point since manipulation of the growth pressure can critically hinder the laminar flow inside the reactor [187], but will be evaluated in section 3.5.4.
Furthermore, preliminary results regarding the impact of growth rates at 710 °C showed varying material composition. As shown in table 3.1, the indium content of the InGaAs layers is only stable for higher absolute TMIn/TMGa fluxes (samples #1 and #2). In comparison, it is reduced progressively for lower fluxes (samples #3 and #4). This behavior signifies a substantial dependency on surface desorption versus incorporation of atom species, an effect that has been observed previously for strained InGaAs layers [188]. Naturally, investigations in the context of designing the jump layer have to be performed at a constant InGaAs composition and this behavior would therefore necessitate a separate calibration for every data point. Further analysis was thus postponed at this point and will be conducted at a later stage in section 3.5.5.
On the other hand, growth temperature has proven to be a decisive parameter for the optimization of MMBs [151], since it prominently affects surface diffusion as well as the mobility of dislocations inside the layer [189] and will therefore be the central tuning knob here.

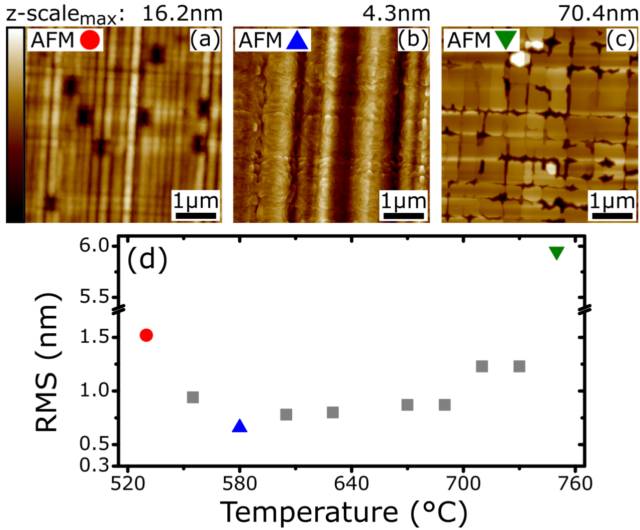


**Fig. 3.4.** AFM analysis of the temperature dependence of 100 nm thick InGaAs layers with a TMIn flux of 6.0 µmol/min. Graph (d) shows the behavior of the surface roughness depending on temperature. AFM scans (a), (b) and (c) exemplify the topography at selected values. (Graph (d) reproduced after [183])

#### 3.2.1.3 Temperature investigation, coarse

Fig. 3.4(d) displays the temperature evolution of the RMS of 100 nm thick InGaAs layers with a TMIn flux of 6.0 µmol/min. Increasing the temperature above the initial 710 °C results in a plateau-like, step-bunched cross-hatch surface structure, as exemplified by the AFM scan Fig. 3.4(c) for 750 °C. In contrast, lowering the temperature has a smoothening effect on the surface resulting in a minimum at 580 °C. Eventually, the RMS increases again below 550 °C The decline of epitaxial quality at this point is indicated by the onset of a hole pattern, as shown in Fig. 3.4(a). This morphology is possibly caused by inadequate surface diffusion to counteract a decreased growth speed around

emerging TDs due to the associated strain-fields [190]. Additionally, insufficient pyrolysis of the precursors starts to play a role at lower available thermal energy (see 2.2.1). The surface of the layer grown at the optimal temperature of 580 °C, depicted in Fig. 3.4(b), features an anisotropic cross-hatch mainly consisting of single steps. This anisotropy between [011]/[$0\bar{1}\bar{1}$] and [$0\bar{1}1$]/[$01\bar{1}$] directions is typically caused by an imbalance of plastic relaxation in their respective (111) and ($1\bar{1}\bar{1}$) slip planes [119]. However, the relaxation data acquired by XRD reveals values of 42.5 % and 40.5 %, respectively. This hints at the imbalance being present only at the early (i.e., thin layer) stages of growth (cf. section 3.2.1.6). The respective morphology anisotropy, however, is transferred to thicker structures.
**Error sources:** An indium content of 20.7±1.4 % was determined for the samples in this series. The standard deviation significantly exceeds the measurement error of the XRD (0.2%) and represents an unusually large fluctuation for MOVPE processes. It was attributed to an instability in the TMIn bubbler cylinder, which was fixed for all subsequent samples. In contrast, no systematic temperature dependant variation of the indium incorporation was observed. The large content error of 6.8 %, in combination with the coarse temperature steps, allows only a preliminary determination of 580 °C as the optimal growth temperature. The re-iteration and fine-tuning of this parameter are therefore performed at a later stage in section 3.2.1.5. As a further consequence, the thickness of the InGaAs layers fluctuates in concert with their indium content, with the exception of the sample grown at 530 °C. Here, a slight drop in the growth rate of $\approx 4$ % was detected, reinforcing the observation of insufficient pyrolysis (cf. Fig. 3.4(a)).

#### 3.2.1.4 Low temperature 2D-3D transition

At this point, a re-iteration of the maximum indium content was performed at 580 °C. An increased permissible value is expected since lower temperatures are known to suppress 3D growth [191].
The result of this test series is shown in Fig. 3.5(d). It reveals a mostly linear roughening behavior within the investigated TMIn flux range

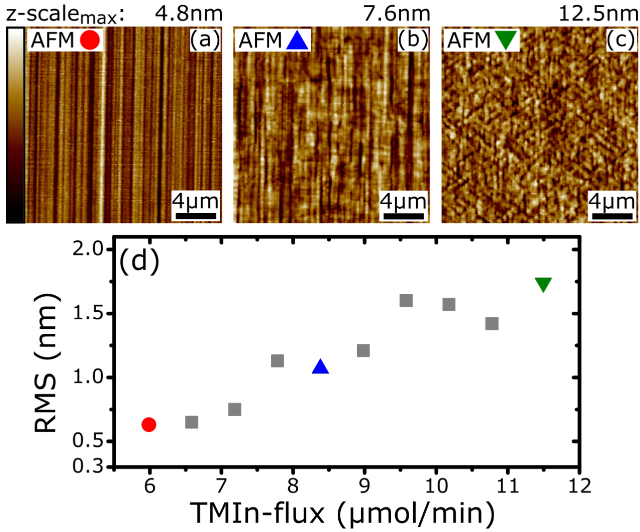


**Fig. 3.5.** AFM analysis of 100 nm thick InGaAs layers with varying indium content grown at 580 °C. Graph (d) shows the behavior of the surface roughness depending on the TMIn flux. AFM scans (a), (b) and (c) exemplify the topography at selected values. (Graph (d) reproduced after [183])

instead of the clear growth-phase transition observed in Fig. 3.2. However, a peculiar evolution of the surface topography is visible instead. When increasing the TMIn flux from 6.0 µmol/min (Fig. 3.5(a)) to 8.4 µmol/min (Fig. 3.5(b)), the cross-hatch pattern starts to balance out instead of being dominated by the $[0\bar{1}1]/[01\bar{1}]$ direction. However, beyond this value, untypical ordering emerges along the diagonal [001] and [010] directions, as exemplified in Fig. 3.5(c) (11.5 µmol/min). This transition could be connected to a change in dislocation morphology from regular rectangular dislocations to random arrays of curved dislocations described by Breen et al. in Ref. [192]. They specify $x = 0.25$ as the critical indium composition, which is in accordance

with XRD measurements of the 8.4 µmol/min-sample yielding a content of $26.4 \pm 0.2\%$. They furthermore observed partial dislocations and stacking faults for this ultra-high MD density growth. Therefore, it was decided to avoid this regime and adopt 8.4 µmol/min as the maximum permissible TMIn flux for the jump layer. Nevertheless, this decision will be re-examined in section 3.5, addressing the question of using the diagonally patterned topography. Notably, the utilized precursor fluxes entail a final growth rate of 0.49 nm/s.

**Error sources:** Similar to the high-temperature evaluation in section 3.2.1.1, increasing the TMIn flux influenced the growth rates, which were thus extrapolated to minimize the error. Nevertheless, the XRR-measured layer thicknesses diverged from the defined value of 100 nm with a standard deviation of 1.6 %. This is, however, an acceptable error and no recalibration and regrowth was necessary.

#### 3.2.1.5 Temperature investigation, fine

Based on this revised TMIn flux of 8.4 µmol/min, a re-examination and fine-tuning of the growth temperature was performed next. The small-step roughness investigation is shown in Fig. 3.6. The RMS increase below 560 °C and above 620 °C clearly reinforces that a minimum of roughness has been found. However, considering the measurement scattering, the precise position of this minimum is less well-defined.

Furthermore, in contrast to the observations in section 3.2.1.3, a trend towards lower indium incorporation at elevated temperatures is visible for the higher TMIn flux used. This effect probably stems from an increased desorption ratio at higher target indium content and larger strain energies [193]. The smoothening influence of lower indium content is hence superimposed on the RMS data. As a result, this reinforces the rising slope at >600 °C, while the detrimental effect of insufficient thermal energy <560 °C has already been established.

Nevertheless, instead of directly using the temperature with the minimal RMS, 595 °C was added as an intermediate step between the two best values (600 °C and 590 °C) and displayed stable roughness.

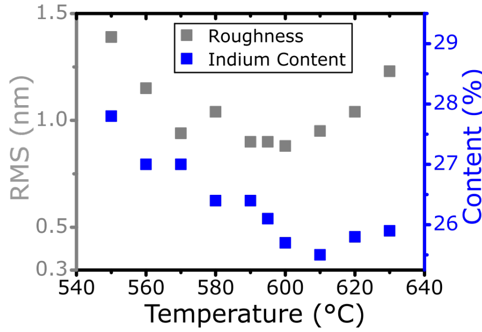


**Fig. 3.6.** Temperature-dependent roughness of 100 nm thick InGaAs layers with a TMIn flux of 8.4 µmol/min. (Graph IV reproduced after [183], supplementary)

Therefore, 595 °C is the final value for temperature calibration. Furthermore, ± 5 K can be given as the optimization precision but is also a measure of the process stability.

### 3.2.1.6 Plastic relaxation initiation

Defining the temperature and TMIn flux covers the two main parameters of the jump layer. Therefore, at this point, a study of the plastic relaxation behavior depending on the layer thickness was performed, with the goal of determining the critical thickness. This investigation was combined with a roughness analysis, and both results are displayed in Fig. 3.7.

Notably, the grey squares depict the average relaxation in the two in-plane directions. However, this only provides a proper description for layer thicknesses ≥50 nm for which a balanced relaxation (within measurement errors) has been observed. The 20 nm sample shows a non-uniform relaxation of 6.9 % in the [011] direction versus 1.2 % in the $[01\bar{1}]$ direction. Similarly, imbalanced results were observed for 30 nm layer thickness, namely 17.8 %/5.0 % for $[011]/[01\bar{1}]$ XRD measurements. This sort of anisotropic plastic relaxation near the

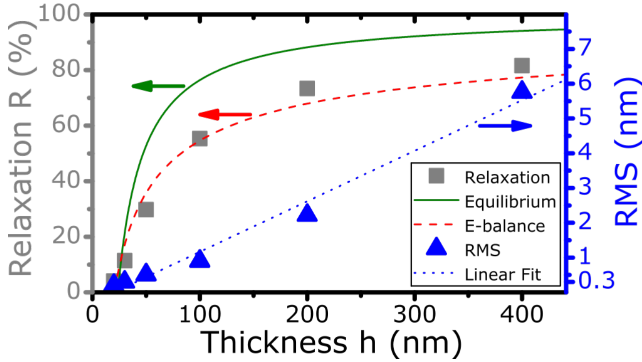


**Fig. 3.7.** Strain relaxation and surface roughness depending on thickness of $In_{0.264}GaAs$ layers grown at 595 °C with a V/III ratio of 102. Includes an equilibrium model and an energy balance model fit of the relaxation as well as a linear fit of the roughening behavior. (Reproduced after [183], supplementary)

critical thickness has been amply described in literature for InGaAs layers [194, 195]. It is attributed to $\alpha$ dislocations with $[01\bar{1}]$ line direction (responsible for relaxations in [011] direction) having higher glide velocities and lower nucleation energies in undoped and n-type compressively strained layers than their $\beta$ ([011]) counterparts [120, 196]. Furthermore, a typical saturation behavior [114] is observed for the relaxation. The solid green line represents a fit according to the equilibrium model ($\propto h^{-1}$) with a fit parameter of $h_c$ =23.6±3.1 nm and a low coefficient of determination of $R^2 = 0.63101$. In contrast, the energy balance model fit (dashed red line; $\propto h^{-1/2}$) agrees well ($R^2 = 0.97166$) with the experimental data for a fitted critical thickness of $h_c$ =20.1±1.4 nm. As has been previously reported [134], models describing partly relaxed InGaAs layers must carefully consider the formation and propagation of (e.g., half-loop) dislocations in order to accurately predict the relaxation behavior beyond the critical thickness.

Furthermore, calculations (see section 2.2.4.1) produce values of

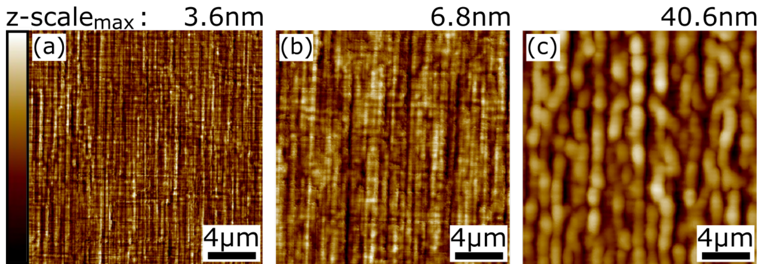


**Fig. 3.8.** AFM surface scans of $In_{0.264}GaAs$ layers with varying thickness grown at 595 °C with a V/III ratio of 101. (a): 50 nm; (b): 100 nm; (c): 400 nm

.

$h_c$ =3.98 nm for the Matthews and Blakeslee model (force balance [121]) and 24.93 nm according to People and Bean (energy of MD network [122]). Obviously, the latter shows much better agreement with the experimental data. However, the Matthews and Blakeslee model is established as the standard in the community [197]. Discrepancies, like for the XRD measurement at hand, are typically ascribed to influences like limited resolution and initially sluggish lattice relaxation [198]. They can be eliminated by utilizing methods that are more sensitive at the early stages of plastic relaxation, e.g., TEM analysis of misfit dislocations [199]. Furthermore, temperature effects and multiple dislocation types can also play a role [109], complicating the analysis of $h_c$.
Nevertheless, for the purpose of the jci-design, the exact determination, and discussion of the critical thickness is of secondary importance. Instead, a clear onset of plastic relaxation is the pivotal criterion. Therefore, 30 nm was chosen as the proper thickness for the jump layer since it is larger than all $h_c$ values mentioned above and has a stand-alone XRD measurement of 11.4 % relaxation. This decision will be re-examined in section 3.5.
The surface roughening in Fig. 3.7 (blue triangles) shows no saturation. Instead, a linear fit function (dotted blue line) displays good

agreement ($R^2 = 0.981$) for a slope of $\Delta\text{RMS} = 0.0145 \pm 9 \cdot 10^{-4}$ and an x-axis intercept at 19.8 nm. In other words, a roughening of approximately 1.5 nm RMS increase per 100 nm thickness once the layer starts to relax plastically is observed.

In the surface topography, this effect appears as a merging and heightening of the undulations, which is illustrated in Fig. 3.8. This progression can be tracked by the wavelength of the undulations in $[01\bar{1}]$ direction increasing from 0.40±0.05 µm for 50 nm thick InGaAs to 0.67±0.07 µm at 100 nm and 1.25±0.07 µm at 400 nm. The peak-to-peak height is extremely unevenly distributed but can be approximated to 1.5/3/15 nm for 50/100/400 nm layer thickness, which means that it scales consistently with the z-scale maximum (cf. values in Fig. 3.8) and consequently, RMS roughness.

This roughening process is commonly attributed to modulations in chemical potential induced by unevenly strain-relaxed regions due to the presence of misfit dislocation arrays [200, 201]. This, in turn, leads to lateral mass transport through surface diffusion [202]. These strain fields influence surface roughness up to 2-10 µm above the original dislocation [203] (see also section 3.5.7).

The alternative model associates high indium content and low growth temperature with the onset of fluctuations in composition, i.e., phase separation [204]. Once established, this state would then stabilize the growth speed imbalance between Ga-rich valleys and In-rich hillocks against the smoothening via lateral material transport to eliminate surface steps [114, 115]. However, the STEM data shown in section 3.4.3 refutes this explanation for the case at hand.

In any case, diffusion and lateral growth rate play a major role in determining the structure's surface morphology. However, the growth temperature as a potent parameter for altering the surface mobility is already optimized at this point, and thus, the V/III ratio was examined next.

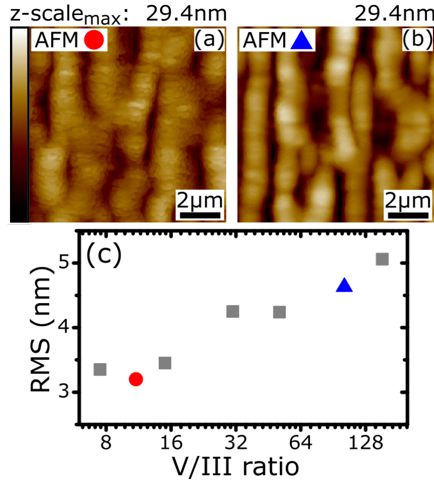


**Fig. 3.9.** Surface roughness of 400 nm thick $In_{0.262}GaAs$ layer with final jump layer TMGa/TMIn fluxes and varied V/III ratio via $AsH_3$ flux.

### 3.2.1.7 V/III ratio

In order to investigate the influence of the V/III ratio on the surface roughness, samples with 400 nm thick InGaAs layers were prepared since a larger thickness should provide a better RMS contrast. Additionally, this is close to the reference value of a λ-cavity. The precursor fluxes were kept constant at 8.4 µmol/min for TMIn and 20.8 µmol/min for TMGa, as previously determined. Consequently, the $AsH_3$ flux was varied to change the V/III ratio. Fig. 3.9(c) shows the resulting RMS depending on the V/III ratio. A clear trend towards reduced roughness at lower V/III ratios is observed. It is approximately linear between a V/III of 150 and 11 in the displayed $\log_2$ scale. However, the data point for the lowest V/III ratio of 7.5 shows a slight increase in RMS instead. Due to machine limitation, the $AsH_3$ flux can not be reduced further to reach smaller V/III ratios. Therefore, at this point, there is no way to unambiguously confirm that an RMS

minimum has been found around V/III= 11. Nevertheless, the clear and stable smoothening of approximately 30 % at this lower V/III range entails V/III= 11 as the adapted value for further growth.
The influence of this smoothening effect on the surface morphology is visible in the comparison between the AFM scans in Fig. 3.9(a) and (b). The enhanced surface mobility of the In and Ga adatoms, due to the lower $AsH_3$ flux [205, 206], leads to an increase in atomic layer completion and a decrease in additional layer nucleation. This circumstance reduces the depth and size of the valley (dark brown) as well as hillock formations (light yellow). Note that the z-scale of both scans has been equalized to emphasize this difference in surface features. The indium composition remains stable throughout all samples at 26.2±0.1 % within the examined V/III range. This observation is contrary to the result by Bugge et al. [188], who reported a higher In incorporation at higher $AsH_3$ fluxes. Nevertheless, the updated jump in lattice constant constitutes 1.84 % at this point and is hence close to the maximum permissible value found in literature of ≈ 2 % [184]. Markedly, this step finalizes the optimization of the jump layer.

### 3.2.2 Convex grading layer

With the optimization of the jump layer being concluded, examining the graded layer, i.e., growth stage II (cf. Fig. 3.1), is the next step. The optimal grading function must promote high average strain without excessively increasing the surface roughness. Ideally, the design should endorse the necessary misfit dislocation formation close to the interface, i.e., far away from the active layer.
According to the results by Kujofsa et al. in Ref. [207], a sublinear grading fulfills the last requirement. However, the proposed logarithmic ($\propto \ln(1 + z/h)$) function is not ideal for maximum strain. Therefore, the function of a quarter circle in the second quadrant was used instead. It is comparable in strain production to the exponential design ($\propto (1 - \exp(z/h))$) examined in Ref. [208]. With the starting point being shifted appropriately, this means the TMIn flux as a

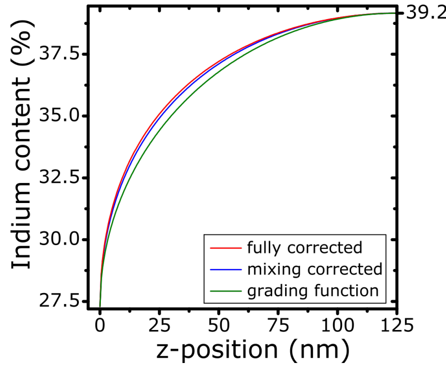


**Fig. 3.10.** Indium content function of a 125 nm thick graded InGaAs layer transitioning from 26.2 % to 39.2 %. Green line: raw grading function from equation 3.1. Blue line: grading function with TMIn/TMGa mixing correction. Red line: grading function with TMIn/TMGa mixing and growth rate correction.

function of growth time is given by

$$y(t) = y_0 + G \cdot \sqrt{1 - (t-1)^2}, \tag{3.1}$$

with $y_0$ being the flux of the jump step, $G$ being the maximum grading, and $t$ going from 0 to 1.
Two major corrections have to be considered when function 3.1 is translated to the indium content depending on the position in growth direction $z$. Fig. 3.10 illustrates the impact of these corrections exemplified by a 125 nm thick InGaAs layer with an indium content ranging from 26.2 % to 39.2 %. Based on the green quarter circle function, the blue line corrects the mixing ratio according to equation 2.8, while the red line also considers the enhanced growth speed at increased added TMIn flux. Both corrections lead to a higher indium content in the medium grading range, with the mixing adjustment having a larger impact than the changing deposition rate. Nevertheless, even after these distortions of the original grading function, the general idea of

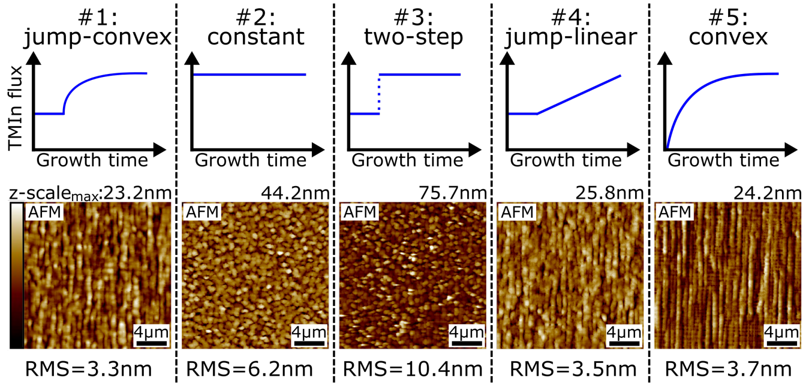


**Fig. 3.11.** Comparison between AFM scans of various $In_xGa_{1-x}As$ grading profiles to reach 13.2 µmol/min TMIn flux. The constant section used in profiles #1, #3 and #4 has a thickness of 30 nm and each structure's total thickness is 200 nm. (Graph reproduced after [183])

a high slope at the start, which then abates in the end, is maintained.

Fig. 3.11 displays a surface topography comparison of the jump-convex design with four alternative grading schemes. All structures have a total thickness of 200 nm and a final TMIn flux of 13.2 µmol/min. Furthermore, designs #1, #3 and #4 utilize the jump layer optimized in section 3.2.1.

The jump-convex grading results in a RMS roughness of 3.3 nm and a mostly balanced [011]/[01$\bar{1}$] morphology. Moreover, its final $In_x$ of 37.0 % at 77.0 % relaxation represents an effective lattice constant of $In_{0.285}GaAs$. These values can also sensibly be compared to 200 nm thick $In_{0.262}GaAs$ (thickness extended jump layer) with an RMS of 1.9 nm and an effective lattice constant of $In_{0.205}GaAs$. An increase by a factor of 1.4 in lattice constant transition is accompanied by a 74.0 % roughness increase, which is an acceptable ratio for the targeted composition range.

The constant composition design #2 represents the maximum feasible strain for the given final TMIn flux. Due to the resulting higher

relaxation state (84.4 %), the structure's effective lattice constant corresponds to $In_{0.313}GaAs$. However, it also has almost double the roughness.
The two-step design #3 produces similarly high strain but integrates the results of the jump layer optimization. Notably, the RMS is even worse than for design #2, possibly because the considerable amount of highly strained material (i. e., 30 nm of $In_{0.262}GaAs$) that transitions to a 3D growth mode can cause a stronger roughening than a thin SK 3D nucleation layer. Therefore, while fast grading is profitable, a discontinuous step to the final content clearly overextends the strain engineering.
In contrast, structure #4 omits steep grading slopes and uses a linear function. This results in a comparable RMS to the reference. However, the lattice constant transition is significantly reduced, resulting in an indium content equivalent of 26.3 %. Finally, structure #5 aims to utilize the advantages of a convex grading discussed above but omits the jump step. The reduced average strain compared to design #1 inhibits the plastic relaxation and produces the effective lattice constant of only $In_{0.268}GaAs$, i.e., higher than #4 but lower than #1. Moreover, the AFM scan shows a slightly increased roughness, but more importantly, it forfeits the balanced $[011]/[01\bar{1}]$ morphology (cf. section 3.2.1.4). This also coincides with a large tilting in $[01\bar{1}]$ direction of 1.1 °, which exceeds the values measured for the jump-convex design by a factor of 3-4 (cf. section 3.4.2). The tilt hints at an imbalance of $\beta$-dislocations, which is suppressed by the insertion of a jump layer. Finally, with this grading, the relaxation initiation depends on the final composition, while they are decoupled for the jump-convex design.
In conclusion, the displayed comparison clearly showcases the superiority of the proposed jump-convex design, which can thus confidently be used for all further structures.
With the grading function defined, the most practical thickness can be determined next. There are two constraints for this parameter. Firstly, a thinner layer means more space for a thicker inverse layer, for which a minimum target of approximately 50 nm seems sensible.

**Table 3.2.** Convex grading layers with varying thicknesses and grading rates. All structures include a 30 nm jump step.

| # | thickness | TMIn final | RMS | relaxation | max content |
|---|---|---|---|---|---|
| 1 | 130 nm | 14.2 $\frac{\mu mol}{min}$ | 2.80 nm | 72.5 % | 38.4 % |
| 2 | 100 nm | 14.2 $\frac{\mu mol}{min}$ | 2.49 nm | 66.9 % | 38.0 % |
| 3 | 80 nm | 14.2 $\frac{\mu mol}{min}$ | 2.23 nm | 64.4 % | 37.9 % |
| 4 | 100 nm | 15.6 $\frac{\mu mol}{min}$ | 3.07 nm | 63.6 % | 39.1 % |

This will increase not only the spacing between QDs and the interface but also the flexibility for the design of photonic devices. Secondly,the low thickness limit is given by the necessity to increase the grading slope, which will, at some point, disrupt the strain engineering, as illustrated by the two-step design in Fig. 3.11. Furthermore, beyond this hard constraint, stopping at a thickness with high relaxation slope could undermine a reliable and reproducible MMB deposition since minor variations of deposited material could lead to large fluctuations of the effective lattice constant. Considering the relaxation data in Fig. 3.8, a thickness in the 75 nm to 150 nm range should be sensible. Therefore, samples with a convex layer thickness of 130 nm, 100 nm and 80 nm were prepared and their roughness, as well as relaxation state, were examined. The comparison can be seen in table 3.2. Samples #1, #2 and #3 have the same final TMIn flux, which is reflected in their similar maximum indium content. However, the reduced thickness results in an effective lattice constant of $In_{0.273}GaAs$ for 130 nm thickness and a considerable decrease to $In_{0.254/0.240}GaAs$ for 100/80 nm due to lower relaxation. Therefore, the aim of sample #4 was to compensate for this effect by increasing the TMIn flux. As designed, this resulted in an increased indium content of 39.1 %. Nevertheless, due to an unexpectedly low relaxation value, only the effective lattice of $In_{0.249}GaAs$ is reached. This circumstance could be the first indication of unfavorable relaxation instability in this thickness range. Additionally, a slightly improved RMS for thinner layers was offset by minor deterioration.

Therefore, 130 nm of convex layer thickness was selected as a good compromise between thin-film requirements and reliable relaxation, and the optimization procedure advanced to growth stage III.

### 3.2.3 Inverse layer

The pivotal criterion for the calibration of the inverse layer is the necessity to provide the correct amount of strain reduction to allow for QD emission in the telecom C-band. For a fully relaxed layer like the inverse step, this translates directly to its indium content. Thus, finding the correct value here is the goal of the following study.
There are two reference numbers for the target composition in the literature. Semenova et al. used the lattice constant of $In_{0.374}GaAs$ for a structure grown via MBE [80], while the MOVPE-grown QD/MMB structure by Paul et al. [82] utilized $In_{0.295}GaAs$. This work will stay closer to the second value because of the similar growth process. Furthermore, of the available 220 nm (see section 3, introduction), after subtracting the thickness of the jump and convex layers, 60 nm remains for the inverse step.
In order to maintain an unstrained inverse layer for varying the indium composition, the convex grading has to be adjusted accordingly to provide the appropriate effective lattice constant. Since the thickness has been fixed to 130 nm, the final grading flux has to be adapted. Five pairs of convex plus inverse layers were prepared, including a calibration of all growth rates. The maximum indium contents on top of the grading sections are 35.9 %, 37.0 %, 38.2 %, 39.3 % and 40.6 %, which are combined with their matrix counterparts of 27.0 %, 28.2 %, 29.4 %, 30.3 % and 31.4 %. Notably, instead of perfect lattice matching, a slight residual strain ($< 5\,\%$) was used to avoid tensile strain.
Based on these designs, five samples featuring QDs and a 220 nm thick InGaAs capping with the same indium content as the inverse layer were grown. The QD deposition was performed at 595 °C and with a TMIn

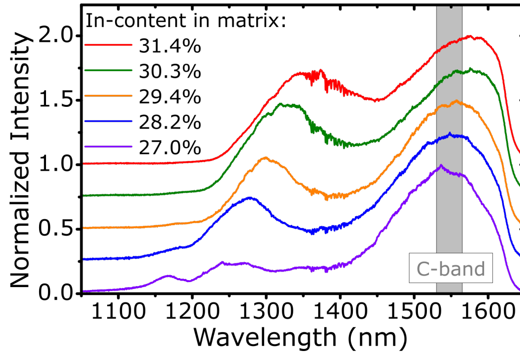


**Fig. 3.12.** Optimization of the inverse step indium content for QD emission at 1550 nm: Photoluminescence spectra of samples with varying indium content in the $In_xGa_{1-x}As$ matrix around the QDs. The curves are offset vertically for clarity. (Graph reproduced after [183])

flux of 9.6 µmol/min for a duration of 4 s. This approach represents the most basic recipe using the optimized temperature of the MMB growth and the default material supply of the established InAs-QDs-on-GaAs recipe. A dedicated optimization of the QD deposition was conducted at a later stage and is described in section 3.3.
The PL spectra under nonresonant excitation at 4 K of these samples are shown in Fig. 3.12, where the prominent peak around 1550 nm in each spectrum can be identified as QD emission. The observed red-shift for the displayed composition range from 27.0 % to 31.4 % is around 40 nm. This value can be compared with literature calculations made by Seravalli et al. in Ref. [209], where they discuss the impact of matrix composition and relaxation on the emission energy and predict a linear behavior for the indium content of a fully relaxed matrix. Between 27.0 % and 31.4 %, this would result in a shift from 1530 nm to approximately

$$E_{GaAs} - (E_{GaAs} - E_{0.270}) * (31.4\%/27.0\%) \approx 0.718\,\text{eV} \widehat{=} 1727\,\text{nm},$$

with $E_{GaAs}$ being the emission energy of InAs QDs on GaAs($\widehat{=}$900 nm) and $E_{0.270}$ being the energy of the peak maximum for the $In_{0.270}GaAs$ sample. In other words, calculations predict a shift of $\Delta\lambda_{calc} \approx 200$ nm instead of the measured 40 nm. This discrepancy can not be explained by the cut-off wavelength of the detector, which only dominates the curve shape for wavelengths $> 1625$ nm (see 2.3.4). Therefore, the impact of strain reduction clearly shows diminishing returns on the InAs QDs energy for the presented MOVPE-grown structures. Moreover, similar to Semenova et al.[80], Seravalli et al. also determined a significantly higher necessary indium content than the $\approx 30$ % used in this work to reach the telecom C-band[210]. This difference can tentatively be ascribed to QD deposition by MOVPE in contrast to MBE but could warrant further investigation in the future.
The ensemble distribution is greatly inhomogeneously broadened for all five samples, resulting in a full width at half maximum (FWHM) of more than 150 nm or $\approx$ 78 meV. In comparison, deposition on GaAs leads to a FWHM in ensemble PL of around 18.6 meV [211] or 23 meV [212]. The amplified broadening is an expected result of the additional inhomogeneity introduced by the insertion of the MMB since slight fluctuations of the strain field can significantly affect the QD deposition and the subsequent emission behavior [213].
One consequence of the stagnant wavelength shift and the broad emission peak is the lowered importance of the PL measurement for the exact selection of the matrix composition. Thus, properties like crystalline quality can be considered with a higher priority. A fluctuation of the RMS roughness is observed for the five PL samples displayed in Fig. 3.12 instead of the expected monotonous increase with indium content. The $In_{0.294}GaAs$ sample exhibited minimal RMS with 4.91 nm, while lower or higher indium content led to 6.14 nm, respectively 6.26 nm. This minimum behavior was not present for the calibration structures, which omitted QD plus capping growth. It could be ascribed to missing precision of lattice matching between convex and inverse layers, although a calibration via XRD measurements was performed, which only manifests for thicker layers. Furthermore, using an $In_{0.294}GaAs$ matrix consistently produced RMS $<$5 nm for

repeated re-growth as well as deposition of the structure on a DBR. Therefore, lacking any PL-quality incentives as described above, the $In_{0.294}GaAs$-configuration was fixed for the inverse-layer deposition. It corresponds to a TMIn flux of 9.1 µmol/min and a final convex grading of 14.2 µmol/min, thus, concluding the jci-MMB optimization procedure.

**Error sources:** The central error margin that has to be mentioned for the inverse-layer optimization is given by the precision and reproducibility of the stated indium composition. The value of 29.4 %, used in Fig. 3.12 and the corresponding text, is measured for this distinct sample but constitutes an outlier. The mean indium composition determined for the inverse layer of various jci-MMB structures via XRD is 28.7 %, with a variance of 0.3 %.

## 3.3 QD growth optimization

With the jci-MMB being defined in a stable manner, at this point, the QD deposition procedure on this virtual substrate can be addressed. The µ-PL data in this section was primarily measured by Cornelius Nawrath and Julius Fischer.

The optimization was performed based on the planar cavity bottom DBR structure, as discussed in section 4.1. This approach constitutes an easy method to enhance light extraction and thus increase the data validity. Furthermore, this is the same cavity type as the sample featured in Ref. [82], which allows a direct comparison of the emission quality. In contrast to other works, AFM investigation was omitted because of the limited transferability of QD shapes to their capped counterparts [214]. Instead, µ-PL measurements were used to directly attain figures of merit like brightness, linewidth and FSS for various samples and asses the most favorable QD growth parameters. In order to enable efficient allocation of measurement time, two different µ-PL setups were utilized. The lower quality, multi-purpose precharacterisation setup was mainly used to exclude clearly unsuitable structures in the early optimization phase. Promising candidates were

then transferred to the specialized infrared setup for final characterization, including the determination of FSS via polarization-dependent evaluation. Brightness is specified by the averaged raw counts per second of the brightest line in each distinct QD spectrum. This uncalibrated value can thus only be used to compare samples among each other in the paragraph at hand. A calibrated comparison with literature is shown in section 4.1. All measurements were performed at 4 K and with above-band excitation.

The starting point is the established recipe for high-quality, low-density InAs QD growth for emission around 900 nm [215] adjusted for deposition on GaAs substrates without offcut. The parameters include a TMIn flux of 9.4 µmol/min for 4 s with a V/III ratio of 310 at a temperature of 530 °C. The QD growth is supplemented with a 1.5 nm thick GaAs AnnCap deposited after an interruption of 60 s, which then allows annealing at 610 °C with limited indium desorption. Material supply and $AsH_3$ flux were directly adopted, while the target temperature for the annealing and subsequent capping was adjusted to 595 °C, given by the optimization of the InGaAs layer deposition. The first objective was to adapt the encapsulation and the associated heating process to an appropriate thickness and time for the QD/MMB structure. Here, mainly a higher thickness range than for the InAs/GaAs QDs was explored since QDs deposited on InGaAs can reach larger defect-free sizes due to the lower strain [216]. Additionally, the ripening time (i.e., the growth interruption between QD and annealing cap deposition) was investigated in parallel due to the strong interdependence of this parameter with the annealing procedure in terms of indium mobility.

Table 3.3 shows the investigated growth parameters for this purpose. Double horizontal lines loosely group the samples into batches for related comparison. Sample #A1 was simultaneously overgrown and heated to 595 °C in order to serve as a reference for QD deposition without AnnCap or annealing time. For all other samples, $t_{Ann}$ includes the 180 s necessary for heating up from 530 °C to 595 °C and stabilizing this temperature.

The reference sample #A1 exhibits the lowest brightness, stressing

**Table 3.3.** Sample list for the determination of an optimized annealing procedure at 595 °C for low temperature (530 °C) QD growth on a jump-convex-inverse MMB. Mean Cps values marked with an asterisk were determined in the dedicated infrared setup.

| # | $d_{Ann}$ | $t_{Ann}$ | $t_{Ripe}$ | $Cps_{Mean}$ | $FSS_{Mean}$ |
|---|---|---|---|---|---|
| A1 | 0 nm | 0 s | 60 s | 750 | - |
| A2 | 5 nm | 180 s | 60 s | 950 | - |
| A3 | 10 nm | 180 s | 60 s | 1900 | - |
| A4 | 20 nm | 180 s | 60 s | 750 | - |
| A5 | 5 nm | 420 s | 60 s | 900 | - |
| A6 | 5 nm | 900 s | 60 s | 950/2200* | 40 µeV |
| A7 | 1.5 nm | 420 s | 60 s | 950 | - |
| A8 | 3 nm | 420 s | 60 s | 1150/2300* | 25 µeV |
| A9 | 3 nm | 900 s | 60 s | 900 | - |
| A10 | 5 nm | 900 s | 10 s | 6600* | 40 µeV |
| A11 | 5 nm | 900 s | 5 s | 5300* | 36 µeV |
| A12 | 5 nm | 420 s | 10 s | 6400* | 28 µeV |

the need for a proper AnnCap. For the shortest $t_{Ann}$ samples #A2, #A3 and #A4, the highest raw brightness count is observed for $d_{Ann}$=10 nm. This is, however, caused mainly by a strong background emission even before saturation (see Appendix 6.2). Further increasing the AnnCap thickness to 20 nm retains this effect but leads to an overall drop in brightness. The best emission is thus obtained for $d_{Ann}$=5 nm. Therefore, this value was used to compare different annealing times.
Here, the brightness stays constant over the whole range, indicating decent stability against temperature-induced diffusion. Since 5 nm constituted the thinnest AnnCap for the first batch and emission deteriorates for thicker values, thinner annealing caps were tested next. Samples #A7 with $d_{Ann}$=1.5 nm and #A8 with $d_{Ann}$=3 nm both show promising properties at medium $t_{Ann}$ of 420 s. However,

a decreased brightness is observed for sample #A9, with the highest annealing time. This signifies reduced temperature stability compared to $d_{Ann}$=5 nm, which was thus used for two structures grown with reduced QD ripening time. Nevertheless, sample #A8 was still investigated in the dedicated infrared setup to provide an additional reference point.
$t_{Ripe}$ turned out to have an immensely crucial effect on the emission brightness, which is a plausible observation since the ripening phase prominently dictates the formation of optically active QDs versus defected islands [217, 218]. A reduction of the ripening time from 60 s to 10 s triples the $Cps_{Mean}$ between the respective samples #A6 and #A10. Decreasing the ripening time further to 5 s has a counterproductive effect, though. Moreover, samples #A6, #A10 and #A11 all exhibit an unfavorable large FSS around 40 µeV, while only the $d_{Ann}$=3 nm sample #A8 displays a lowered value. Therefore, sample #A12 with a parameter combination of $d_{Ann}$=5 nm, $t_{Ann}$=420 s and $t_{Ripe}$=10 s was fabricated. This combination retains the high brightness and features a decently low $FSS_{Mean}$ of 28 µeV and is, hence, the final result of the first QD growth optimization step.
Precise calibration of deposition temperature has been reported to effectively reduce FSS for InAs QDs grown on metamorphic InGaAs [219]. Additionally, the parameter prominently influences indium diffusion and, consequently, QD size and area density [217]. Fig. 3.13 shows histograms of the FSS for samples with $T_{QD}$ varied between 520 °C and 570 °C. No overarching trend could be discerned from the measurements. However, specifically for $T_{QD}$ =550 °C, a substantial increase of values in the low, <10 µeV region is found. This finding is similar to Ref. [219], where this effect was observed at 545 °C. Apart from the FSS investigation, area density and brightness characteristics remained within the previously observed range. Therefore, $T_{QD}$ was set to the slightly elevated 550 °C. The corresponding minimal $FSS_{Mean}$ value of 19 µeV can be compared to literature data. It is on par with the 10 to 40 µeV range reported for InAs/GaAs QDs [220, 221]. More importantly, the MMB approach outperforms the InAs-QDs-on-InP-substrate counterpart in this regard, even after the

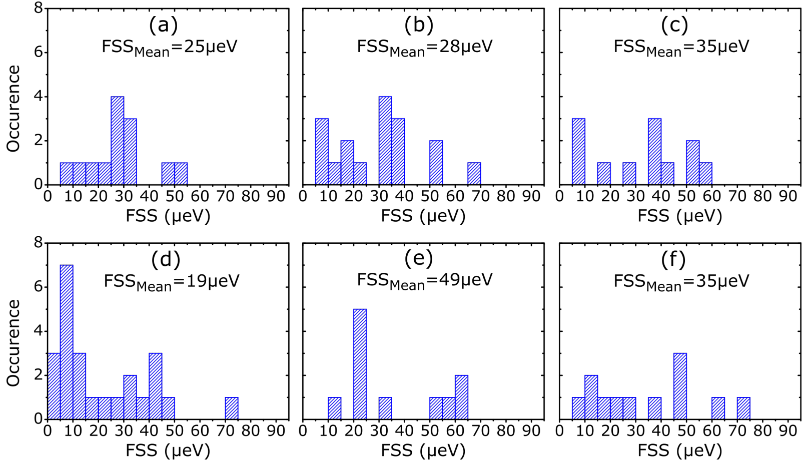


**Fig. 3.13.** Influence of QD deposition temperature on FSS. Histogram for $T_{QD}$: (a) 520 °C; (b) 530 °C; (c) 540 °C; (d) 550 °C; (e) 560 °C; (f) 570 °C

presented FSS reduction from 235 µeV to 29 µeV by implementing the droplet epitaxy technique shown in Ref. [62].
As a final step, the ripening time was revisited due to its crucial influence on the emission brightness. Fig. 3.14 shows the µ-PL spectra of multiple exemplary QDs from samples with varied ripening times. For the sample with a $t_{Ripe}$ of 7.5 s, 10 s and 15 s, the emission stays mostly similar in terms of brightness and linewidth. Furthermore, the FSS remains comparable with $FSS_{Mean,7.5s}$ =22 µeV, $FSS_{Mean,10s}$ =19 µeV and $FSS_{Mean,15s}$ =23 µeV. In contrast, increasing the ripening time to 20 s results in a substantial brightness deterioration by a factor of $\approx 3$. This drop corresponds to the respective improvement observed between samples #A6 (60 s) and #A10 (10 s) in table 3.3. A ripening time between 7.5 s and 15 s can thus be labelled as the favorable regime.

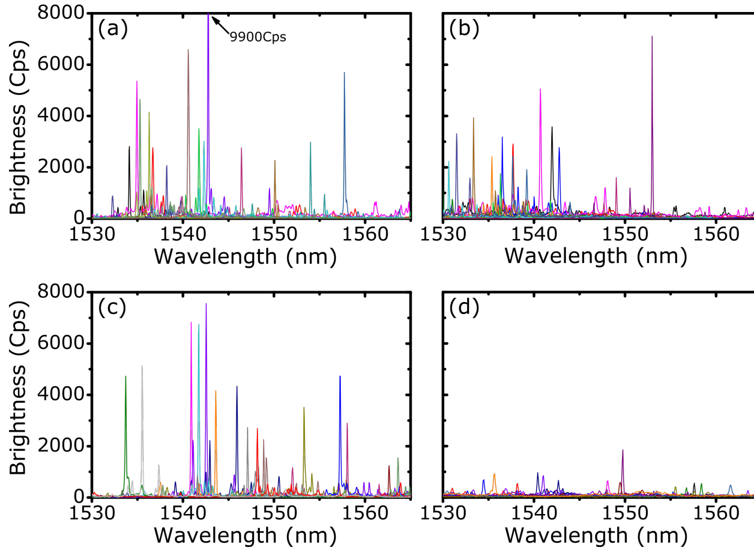


**Fig. 3.14.** μ-PL spectra of samples with different QD ripening times. $t_{Ripe}$: (a) 7.5 s; (b) 10 s; (c) 15 s; (d) 20 s. Note that the measurement was performed with polarisation optics; thus Cps has to be doubled to allow comparison with previous data.

**QD area density:** One essential characteristic of structures with QD-based active layers is the emitter density. Typically, in MOVPE, the density of InAs QDs on GaAs substrate is readily adjusted over several orders of magnitude via controlling the V/III ratio [222]. However, the deposition on an MMB could limit the effectiveness of this approach due to the surface morphology providing distinct nucleation sites and the presence of strain fields from underlying dislocations. Consequently, this makes the initial properties of the optimized QD recipe critically important.
Notably, AFM investigation of uncapped QDs is omitted due to the low transferability of measured properties like area density to the μ-PL data [82]. Therefore, exclusively μ-PL area scans were performed.

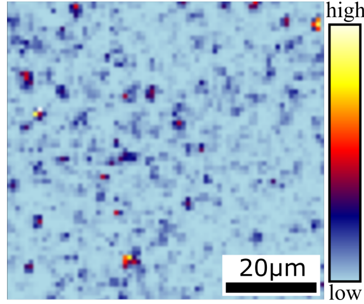


**Fig. 3.15.** 70 µm x 70 µm µ-PL map of emission inside the telecom C-band. Spots with high intensity are identified as QD positions. Evaluation of all distinct emitters results in an area density of $3 \cdot 10^6\,\mathrm{cm}^{-2}$.

This technique records integrated emission intensity inside the C-band at each position. A resulting 70 µm x 70 µm map for the final QD recipe is displayed in Fig. 3.15. By analyzing the number of distinct emission lines, an area density of $3 \cdot 10^6\,\mathrm{cm}^{-2}$ for optically active QDs can be derived. This signifies excellent conditions for addressing individual emitters during advanced quantum-optical measurements. Furthermore, no discernable clustering related to specific cross-hatch regions is observed but rather a uniform distribution. This implies that, within the examined scale, no sufficiently strong strain fields are present on the MMB surface to force the QD formation into a regular pattern [223].
The obtained area density can be discussed in the context of other results in the literature for telecom C-band QDs. The value at hand is most similar to the result of $1 \cdot 10^7\,\mathrm{cm}^{-2}$ reported for the MOVPE-grown, linear MMB in Ref.[82], which is sensible due to the closely related QD deposition conditions. In contrast, Ref.[80] reported a considerably higher density in the $10^9\,\mathrm{cm}^{-2}$ range for molecular beam epitaxy deposition. Here, a 2 µm aperture was necessary to discern distinct narrow emission lines. Even then, no complete spectral isolation was achieved, and instead, multiple QDs were present within

the PL spectrum. Finally, Skiba-Szymanska et al. stated a value of 2-4 $\cdot 10^8\,\mathrm{cm}^{-2}$ for their droplet epitaxy QDs on InP substrate [62].

**Error sources:** The measurement and analysis of a sufficient number of QD spectra in μ-PL to obtain statistically indisputable results is a tedious and time-consuming process. Thus, the considerable quantity of examined samples limits the number of QDs studied on each sample to around 15-25. Consequently, all reported $\mathrm{Cps}_{\mathrm{Mean}}$ and $\mathrm{FSS}_{\mathrm{Mean}}$ values have a high standard deviation of up to 50 %.
Furthermore, the parameter space for QD growth is considerably expanded relative to layer deposition because ripening and annealing time as well as capping thickness are added. Hence, no claim of completeness in terms of globally optimal deposition parameters can be made for the work at hand. Here, the V/III ratio can be given as an example. It influences indium mobility and can be most prominently used to control the QD area density [222]. However, a suitable QD density for single-photon application could be directly transferred from the InAs/GaAs base recipe and remained in a favorable range for all discussed samples. Therefore, only a brief stability check was performed for this parameter. A reduction from the default V/III value of 310 to 208 led to a similar brightness but increased the FSS to 30 μeV. Furthermore, an increase to 465 resulted in a ≈40 % drop in brightness. Thus, the original value of 310 was maintained, and an investigation featuring smaller step sizes was omitted. Growth time and material flux fall into the same category.
Therefore, additional work in understanding the influence of growth parameters on the formation of InAs QDs on top of a jump-convex-inverse InGaAs MMB will undoubtedly be valuable in the future.

## 3.4 Additional structural characterization

Considerable parts of the structural characterization are already discussed for the optimization procedure in section 3.2. This section aims to summarize and complement the structural data of the finalized QD/MMB design with 220 nm total InGaAs layer thickness below the QD and a 230 nm thick capping layer.

### 3.4.1 AFM

AFM scans of QD/MMB samples, which were stopped at different growth stages, are depicted in Fig. 3.16. Note that the cool-down time inside the reactor influences the surfaces for the presented ex-situ measurements despite the $AsH_3$ stabilization.
Fig. 3.16(a) shows the surface morphology after 30 nm jump, 130 nm convex and 60 nm inverse layer growth and hence represents the substrate for QD deposition. The RMS roughness is 2.46 nm and the cross-hatch is mostly isotropic between $[011]/[0\bar{1}\bar{1}]$ and $[0\bar{1}1]/[01\bar{1}]$ directions in accordance with the growth optimization. In Fig. 3.16(b), the QD and AnnCap deposition as well as the annealing have been performed before cooling down. While most smaller, potentially optically active QDs are buried at this stage, and larger islands should mostly be desorbed by the annealing step, remnants of the 3D layer are still visible. Furthermore, a reordering of the surface topography is observed. This results in an anisotropic cross-hatch, dominated by undulations in the $[01\bar{1}]$ direction with a wavelength of $0.8 \pm 0.1$ µm. Both features are erased after the deposition of the 220 nm thick capping layer, as shown in Fig. 3.16(c). The surface RMS is 4.76 nm, which is close to the expected roughness for a 445 nm thick $In_{0.273}GaAs$ layer with optimized growth parameters, as specified in section 3.2.1.6. Hence, the convex grading and the insertion of the QD layer have a negligible effect on the surface quality of the entire 445 nm structure.

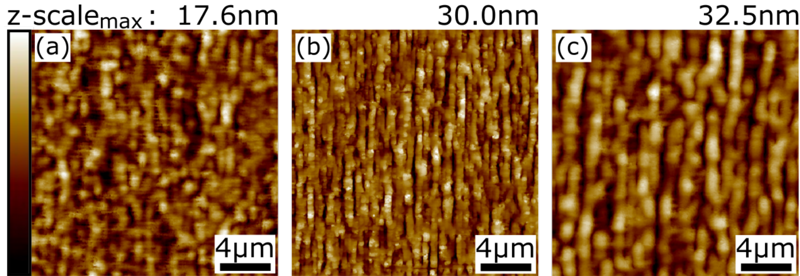


**Fig. 3.16.** AFM scans of the finalized QD/MMB structure at different growth stages. (a) 220 nm jump-convex-inverse MMB ; (b) QD on MMB with $d_{Ann}$ =5 nm and $t_{Ann}$ =420 s; (c) QD/MMB structure with 230 nm capping layer.

### 3.4.2 XRD

Fig. 3.17 displays RSMs around the (400) and (422) reflex of an exemplary DBR sample. Notably, similar RSMs have been used multiple times during the optimization process to determine indium content and relaxation.
The highest intensity peak at large $q_z$ stems from the GaAs substrate. It serves as a calibration point for all other peaks, which can be identified from their relative positioning. Closest to the GaAs, and with the second highest intensity, is the peak that originates from the pseudomorphic AlAs part of the DBR. All additional signal can be attributed to the InGaAs of the MMB. The related lattice constant and strain characteristics can be most handily attributed by analyzing the RSM in [422] direction on the right. Of the two remaining peaks, one is found in the low $q_x$ and $q_z$ region and far from the dashed line in the [422] direction marking complete relaxation. This position represents high indium content and considerable residual strain (70 % relaxation) and is thus identified as the top part of the convex layer and labelled accordingly. The remaining peak is located in the medium indium content region and almost fully relaxed (96 %) and

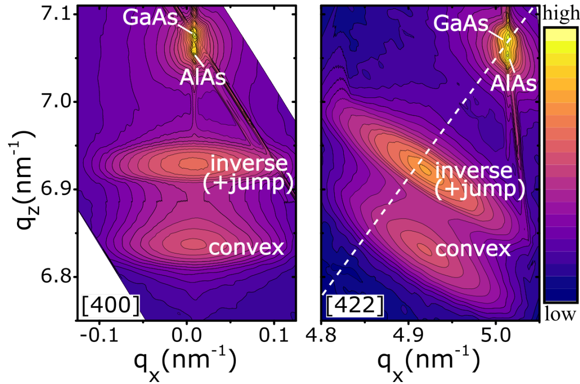


**Fig. 3.17.** RSMs around the (400) (left) and (422) (right) reflex of an exemplary QD/MMB/DBR sample measured via XRD. The intensity peaks from the MMB are labelled according to the structure section they can be identified with according to their respective design. The dashed line in the right panel marks the coordinates of complete relaxation. (Reproduced after [183], supplementary)

can thus be matched to the inverse layer. Both peaks have basically identical $q_x$ coordinates, which signifies in-plane lattice matching as designed.

Crystalline quality can be deduced by examining the broadening directions of the peaks in both RSMs. The significant broadening of both peaks, in $q_x$ direction in the [400] map combined with perpendicular to the dashed line in the [422] map, indicates a pronounced mosaicity of all InGaAs layers caused by dislocations and other defects. Additionally, a modest broadening in the $q_z$ direction in the [400] map plus parallel to the dashed line in the [422] map implies compositional distribution. For the convex layer peak, this feature can be easily attributed to the graded nature of this section. The inverse layer peak could be broadened by a contribution from the jump layer that can not be resolved separately. Alternatively, it could signify a slight inhomogeneity of the indium composition.

**Table 3.4.** Crystallographic tilt analysis of 100 nm InGaAs layers grown on pieces of a single GaAs wafer for TMIn flux, temperature and $AsH_3$ parameter sweeps. Sample T1 is listed in each group for better readability.

| # | TMIn flux | $AsH_3$ flux | $T_{growth}$ | tilt[011] | tilt[0$\bar{1}\bar{1}$] |
|---|---|---|---|---|---|
| T1 | 6.0 µmol/min | 3.0 mmol/min | 580 °C | 0.14 ° | 0.13 ° |
| T2 | 6.6 µmol/min | 3.0 mmol/min | 580 °C | 0.05 ° | 0.17 ° |
| T3 | 7.2 µmol/min | 3.0 mmol/min | 580 °C | 0.15 ° | 0.08 ° |
| T4 | 7.8 µmol/min | 3.0 mmol/min | 580 °C | 0.02 ° | 0.10 ° |
| T5 | 8.4 µmol/min | 3.0 mmol/min | 580 °C | 0.01 ° | 0.12 ° |
| T6 | 9.0 µmol/min | 3.0 mmol/min | 580 °C | 0.17 ° | 0.01 ° |
| T7 | 9.6 µmol/min | 3.0 mmol/min | 580 °C | 0.00 ° | 0.20 ° |
| T8 | 10.2 µmol/min | 3.0 mmol/min | 580 °C | 0.01 ° | 0.21 ° |
| T9 | 10.8 µmol/min | 3.0 mmol/min | 580 °C | 0.02 ° | 0.24 ° |
| T10 | 11.5 µmol/min | 3.0 mmol/min | 580 °C | 0.00 ° | 0.21 ° |
| T11 | 6.0 µmol/min | 3.0 mmol/min | 530 °C | 0.04 ° | 0.13 ° |
| T12 | 6.0 µmol/min | 3.0 mmol/min | 555 °C | 0.20 ° | 0.09 ° |
| T1 | 6.0 µmol/min | 3.0 mmol/min | 580 °C | 0.14 ° | 0.13 ° |
| T13 | 6.0 µmol/min | 3.0 mmol/min | 605 °C | 0.13 ° | 0.17 ° |
| T1 | 6.0 µmol/min | 3.0 mmol/min | 580 °C | 0.14 ° | 0.13 ° |
| T14 | 6.0 µmol/min | 4.5 mmol/min | 580 °C | 0.08 ° | -0.24 ° |
| T15 | 6.0 µmol/min | 6.0 mmol/min | 580 °C | 0.08 ° | 0.26 ° |

**Crystallographic tilt:** Another crystal property accessible by XRD is the lattice tilt relative to the substrate. In metamorphic layers, crystallographic tilt can arise from an imbalance of dislocation types and their associated burger vectors [224], and can hence provide information on the relaxation process. It has been previously reported to depend on the growth parameters of metamorphic InGaAs on GaAs [225].
During the XRD measurement, [011] versus [01$\bar{1}$] direction was consistently defined by the sample mounting. However, the [011] versus [0$\bar{1}\bar{1}$] symmetry can not be retraced. Therefore, positive values are

used to denote all [011], and a chirality switch is indicated by a change of sign.

Table 3.4 shows the tilt of various samples with a 100 nm thick InGaAs layer in exemplary groups of TMIn flux, temperature and $AsH_3$ parameter sweeps. A considerable tilt of up to 0.26 ° was measured. Sample groups #T1-#T10 and #T11-#T13 exhibit large fluctuations for both tilt directions with no visible coupling to one another or TMIn flux, respectively, temperature. While both of these groups preserve chirality, the $AsH_3$ sweep also shows a change of sign between samples #14 and #15.

Any influence of residual offcut uncertainty from different nominally [001] wafers can be excluded because all samples were grown on pieces of a single 3" wafer.

In conclusion, although measured with simple structures, no systematic behavior can be discerned from the data. Instead, the tilt values are attributed to predominantly random imbalances in dislocation nucleation during growth. Therefore, analysis of crystallographic tilt is not utilized for layer optimization or characterization of advanced structures.

### 3.4.3 STEM

STEM can be used for multiple aspects of structural analysis depending on the utilized contrasting method. In order to allow cross-section imaging, a QD/MMB/DBR sample has been prepared into a wedge shape by ion milling.

In Fig. 3.18, the position-sensitive material composition is visible through high-angle annular dark-field imaging showing the structure in Z-contrast. Therefore, aluminium/indium-containing layers appear dark/bright, while high gallium composition produces a grey shade. Consequently, the upper AlAs/GaAs pair of the DBR is plainly visible on the bottom, followed by the brighter jump layer transitioning into the convex part, apparent by a further gradual increase in brightness. Then the jump layer appears as a relatively darker region between the maximally bright top of the capping layer below and the likewise

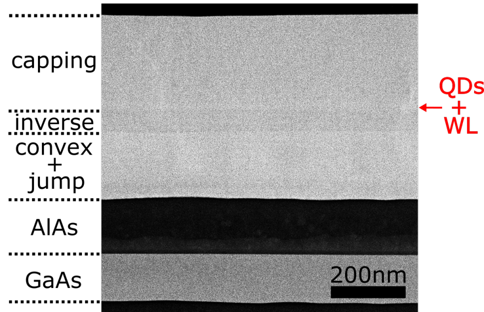


**Fig. 3.18.** STEM with high-angle annular dark-field imaging of a capped QD/MMB/DBR sample displaying the structure with elemental-type contrast. Cross-section view of {011}. The various layers inside the structure are identified and labelled.

bright QD/WL area above. The structure is then finished by the capping layer with medium indium content. The image also confirms an overall thickness of ≈450 nm with the QDs centered in the InGaAs section, as designed for λ-cavity compatibility. Furthermore, inverse and capping layers exhibit the same brightness value and hence indium content, as intended. The apparent difference between the layers is caused by simultaneous brightness contrast [226] due to the disparate brightness of their adjacent regions.
The bright-field method prominently detects defects in the crystal structure, including the associated strain field and atomic displacements. Fig. 3.19(a) shows a variety of defects inside the structure. At the AlAs/InGaAs interface, numerous MDs pointing into the image plane appear as black dots. This is consistent with the slip system producing <011> MDs due to the displayed {011} cross-section. Approximately 34 are found within the 800 nm image width, resulting in an average spacing of $d_{\text{MDs, measured}}$ ≈24 nm. In order to accommodate the lattice transition from GaAs to $In_{0.287}GaAs$, the strain-releasing

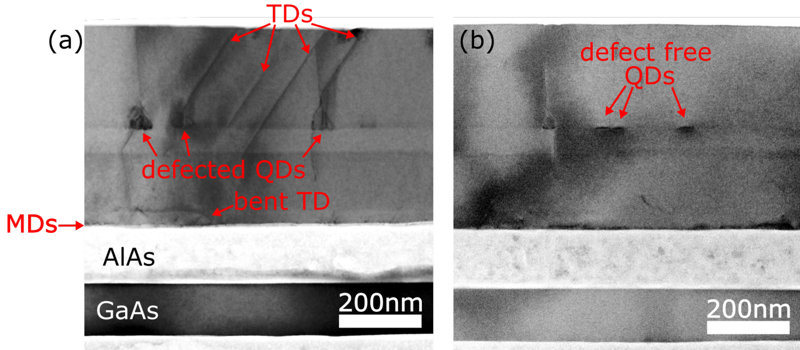


**Fig. 3.19.** STEM in bright-field contrast of a capped QD/MMB/DBR sample at two positions highlighting different structural aspects. Left: multiple kinds of defects. Right: defect-free QDs.

dislocation network has to contain MD with an average distance of

$$d_{\mathrm{MDs,calc}} = \frac{a_{\mathrm{In0.28}}}{\sqrt{2} \cdot f_{\mathrm{In0.28}}} \approx 20.4\,\mathrm{nm}, \tag{3.2}$$

with $a_{\mathrm{In0.28}}$ being the lattice constant of $\mathrm{In_{0.287}GaAs}$ and $f_{0.28}$ being its lattice mismatch to the GaAs substrate. Measured and calculated values are thus in good agreement, especially since the MMB design indeed promotes MD formation at the AlAs/InGaAs interface. However, some TDs might still develop inside the jump-convex region.
As expected, a multitude of TDs is originating from these MDs. Due to this high density, many of those TDs undergo a dislocation annihilation process (cf. [227]) within ≈50 nm, evinced by the dark tent-shaped structures in this region. Furthermore, a bent TD is visible, illustrating another defect reduction mechanism. Several 60° TDs lying in the typical [111] plane of the zincblende slip system are discernible in the upper half of the structure. Notably, their actual origin point is uncertain because an abrupt start inside the graded region could either signify an actual creation event at this position or represent a truncation from the thinning process. Due to the

undefined thickness of the scanned wedge position, no definitive value for the TD density can be determined, but a value in the $10^8\,\mathrm{cm}^2$ range, as predicted by theory [227], is feasible. These TDs are often associated with defected/incoherent QDs because they can serve as respective nucleation sites [228], and the defects inside the islands can glide into the adjacent layers. In contrast, Fig. 3.19(b) shows several defect-free QDs, which are supposedly the desired optically active species.
Finally, one aspect that has to be highlighted is the absence of undesirable phase separation, which has been reported in InGaAs MMBs with final indium composition >35 % and steep grading [150, 204].

## 3.5 Stability against growth parameter changes

The influence of various growth parameters on the MMB quality has already been examined extensively during the optimization process in section 3.2. However, the progression through parameter space has been primarily linear, while strong interdependencies could necessitate extensive re-iteration. This section addresses this issue by taking the final MMB recipe as a basis and introducing minor deviations to various parameters. The feedback of the structural properties is then examined, and either a new optimum is adapted, or the stability of the optimal value against small deviations is defined. This procedure also gives information on adjusting for typical machine-related drift over time. In any case, the possibility of local optima instead of global ones obviously remains nonetheless.

### 3.5.1 Jump-layer thickness

The default thickness of the jump layer is $d_{\mathrm{jump}}$ =30 nm, as established by experimentally determining the critical value for lattice relaxation per the proposed design. However, this premise has to be tested in terms of the principal function of the jump layer, which is,

**Table 3.5.** Variation of jump layer thickness and indium content for growth stage II samples with proper convex layer indium grading for C-band QD emission.

| # | $d_{jump}$ | TMIn flux | RMS | $In_{x,\ eff}$ |
|---|---|---|---|---|
| J1 | 30 nm | 8.4 µmol/min | 2.80 nm | 27.8 % |
| J2 | 20 nm | 8.4 µmol/min | 2.96 nm | 26.1 % |
| J3 | 10 nm | 8.4 µmol/min | 10.55 nm | 25.0 % |
| J4 | 50 nm | 8.4 µmol/min | 2.92 nm | - % |
| J5 | 30 nm | 7.2 µmol/min | 2.47 nm | 28.0 % |
| J6 | 30 nm | 6.0 µmol/min | 2.36 nm | 27.4 % |
| J7 | 30 nm | 10.2 µmol/min | 6.46 nm | 27.3 % |

together with the graded layer, providing correct lattice transition at minimal roughening. For this purpose, samples containing only jump plus convex layer were fabricated (cf. Fig. 3.1, growth stage II). The maximum indium grading content was set as established in section 3.2.3.
Samples #J1 to #J4 in table 3.5 show the impact of changing $d_{jump}$ on the roughness and the lattice constant transition ($In_{x,\ eff}$), with #J1 being the reference. Reducing the thickness of the jump layer from 30 nm to 20 nm increases the RMS moderately by 10 %. Additionally, the achieved lattice constant decreases considerably. This circumstance would have to be compensated by additional grading inside the convex layer, which in turn further increases the roughness. A continued reduction to 10 nm undermines the strain engineering and leads to a 375 % increase of the RMS to 10.55 nm. On the other end, a $d_{jump}$ of 50 nm marginally raises the roughness but is undesirable due to unnecessarily adding to the total thickness. In conclusion, the originally optimized value of $d_{jump}$ =30 nm remains the most favorable configuration.

### 3.5.2 Jump-layer indium content

The TMIn flux for the jump layer was set to 8.4 µmol/min (≘27.3 % indium content) based on Fig. 3.5, aiming for isotropic relaxation and avoiding the regime of diagonal ordering but with no clear phase transition. Therefore, a re-examination of this parameter at this point is particularly sensible.
The results are displayed in table 3.5 for samples #J5 to #J7. Note that the starting point of the grading was adjusted according to the altered TMIn flux of the jump layer. Sample #J1 is again the reference here. Evidently, the relaxation process is only insignificantly affected by this modification since $In_{x,\,\mathrm{eff}}$ remains essentially constant. Moreover, an increase in the flux leads to a substantial roughening by 130 %. On the other hand, a slight reduction to 7.2 µmol/min results in a moderate improvement of the RMS by around 12 %. A further reduction by the same interval as for sample #J6 reveals diminishing returns for this smoothening. However, for the entire 440 nm thick structure, the initial RMS reduction is overwritten by additional roughening. That effect is associated with a more anisotropic surface morphology and pronounced lattice tilt of 0.69 ° in the [011] direction. As a result, this observation supports the original decision made according to Fig. 3.5 of setting the jump-layers indium content to the value with the most balanced strain relaxation.

### 3.5.3 Constant V/III ratio

The optimal V/III ratio has been determined via the group-III precursor flow rates during the jump-layer optimization. However, TMIn flux is varied during grading and inverse/capping layer growth, while $AsH_3$ flux is kept constant. Consequently, the V/III ratio changes accordingly during those steps. Here, two modes of adapting the $AsH_3$ flux for the growth of a full 440 nm jci-MMB structure are investigated.
The first approach is to keep the proper V/III ratio constant. Here, the $AsH_3$ flux has to be consistently graded from 327 $\frac{\mu\mathrm{mol}}{\mathrm{min}}$ to 386 $\frac{\mu\mathrm{mol}}{\mathrm{min}}$

**Table 3.6.** Influence of reactor pressure on surface roughening of 440 nm thick jump-convex-inverse MMB structure.

| # | $p_{reactor, cap}$ | RMS |
|---|---|---|
| P1 | 100 mbar | 4.52 nm |
| P2 | 80 mbar | 7.69 nm |
| P3 | 120 mbar | 4.46 nm |
| P4 | 150 mbar | 4.44 nm |
| P5 | 190 mbar | 4.31 nm |

in the convex section. Then, during the inverse part, a minuscule increase to 330 $\frac{\mu mol}{min}$ compared to the default value is employed. The resulting sample showed ≈17 % smoothening to an RMS of 3.74 nm (reference: 4.52 nm).
This improvement could feasibly be increased by holding the TMIn/$AsH_3$-ratio constant instead. This approach necessitates larger variations in $AsH_3$ flux because the relative TMIn flux is changed more significantly during the grading than the combined group-III precursor flow. However, this structure leads to a roughness increase of ≈13 % to RMS=5.11 nm.
In conclusion, keeping the V/III ratio at the value determined for jump-layer growth by consistently adjusting the $AsH_3$ flux during the grading step ensures a more optimal diffusion resulting in a smoother surface. Furthermore, this effect is moderated by the full TMGa-plus-TMIn-to-$AsH_3$ ratio, despite the In atoms' greater surface mobility.

### 3.5.4 Reactor pressure

In contrast to other parameters, the reactor pressure has not been investigated during the initial optimization process due to its critical importance for the laminar flow. Nevertheless, it will be briefly examined in this section.
The samples grown for this purpose used the default $p_{reactor}$ =100 mbar during the growth of the jump-convex part as well as the first 20 nm

of the inverse layer. The remaining 260 nm of inverse/capping were then deposited at the altered pressure. Table 3.6 shows the impact of $p_{\text{reactor, cap}}$ on the surface roughening of these samples. A reduction to 80 mbar leads to a RMS increase of ≈70 %, rendering all other investigations into this parameter direction futile. On the other hand, ≤200 mbar is the limit for the high-pressure range due to the TMIn-bubbler evaporation ambiance being set to this value. Hence, samples #P3, #P4 and #P5 cover the total available parameter space in this direction. Here, no significant influence on the surface morphology, specifically roughness, can be observed.
Further investigation of the pressure parameter during the growth of the relaxation layers might be sensible. However, in the meantime, there is no reason to deviate from the default 100 mbar.

### 3.5.5 Growth rate

**Table 3.7.** Influence of growth rate on surface roughening of MMB structure with 180 nm thick jump-convex-inverse section and varied capping layer thickness. $d_{\text{total}}$ is the total structure thickness. Precursor fluxes refer to the capping layer growth. $AsH_3$ is adapted to keep the V/III ratio constant.

| # | TMIn flux | TMGa flux | $d_{\text{total}}$ | $\text{In}_x$ | RMS |
|---|---|---|---|---|---|
| G1 | 8.4 $\frac{\mu mol}{min}$ | 20.8 $\frac{\mu mol}{min}$ | 440 nm | 28.7 % | 4.52 nm |
| G2 | 12.6 $\frac{\mu mol}{min}$ | 31.2 $\frac{\mu mol}{min}$ | 440 nm | 29.5 % | 9.99 nm |
| G3 | 16.8 $\frac{\mu mol}{min}$ | 41.6 $\frac{\mu mol}{min}$ | 440 nm | - | opaque |
| G4 | 5.9 $\frac{\mu mol}{min}$ | 14.6 $\frac{\mu mol}{min}$ | 440 nm | 28.6 % | 3.59 nm |
| G5 | 8.4 $\frac{\mu mol}{min}$ | 20.8 $\frac{\mu mol}{min}$ | 1000 nm | - | 9.47 nm |
| G6 | 5.9 $\frac{\mu mol}{min}$ | 14.6 $\frac{\mu mol}{min}$ | 1000 nm | - | 8.39 nm |

Changing the growth rate at constant TMGa/TMIn ratio to control the surface diffusion was touched on during the optimization in section 3.2.1.2. There, it resulted in a substantial drift of the indium composition. This effect is however associated with the incorporation of bigger atoms into a compressively strained layer [188] and should

thus be inactive for the unstrained capping region. Therefore, varying the growth rate was investigated for structures with 180 nm of default jci layers and altered capping.
Samples #G2 and #G4 in table 3.7 indeed show a negligible indium drift compared to the reference #G1, and their roughness can hence be evaluated appropriately. Increasing the growth rate by a factor of 1.5 more than doubles the RMS, and an even faster deposition results in a roughness range that appears as an opaque surface to the naked eye for sample #G3. On the other hand, slower growth by a factor of 0.7 leads to an ≈20 % smoothening effect for 440 nm total structure thickness. Since the roughness becomes specifically detrimental at larger thicknesses (see section 3.5.7), the impact of reduced growth rate was also examined at 1000 nm. Here the altered sample #G6 only shows an ≈11 % RMS improvement compared to the reference #G5.
This unfavorable scaling at increased structure thickness could be attributed to the smoothening effect from a quasi-annealing process due to a longer time at elevated temperatures instead of modified surface diffusion. A combined investigation of annealing and growth rates might hence be sensible in the future.

### 3.5.6 Substrate offcut

Using a substrate with a defined offcut is favored by some applications [229, 230]. For the respective structures, this improves the crystalline quality and enables thicker DBRs. This option was thus tested by growing a 220 nm thick jump-convex-inverse MMB on a GaAs substrate with a 6 ° offcut in $[0\bar{1}\bar{1}]$ direction. An AFM comparison of the resulting surface topography with a reference deposited on a standard substrate is shown in Fig. 3.20. As expected, the surface morphology, which has previously been tuned to exhibit minimal asymmetry, is completely anisotropic for the sample featuring the miscut (Fig. 3.20(a)). The broken symmetry manifests in many closely spaced, irregular atomic steps aligned perpendicular to the offcut axis. Overall the features are much smaller, and the surface looks more

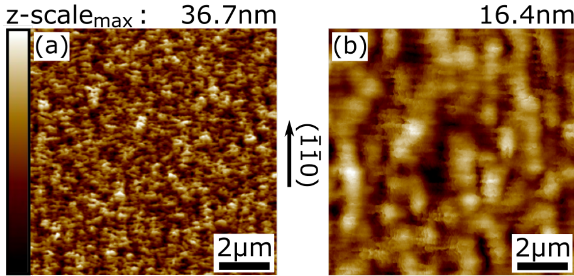


**Fig. 3.20.** AFM scans of 220 nm jump-convex-inverse MMB grown on substrate with (a)6 °, (b)0 ° offcut in [01̄1̄] direction.

finely grained than the reference in Fig. 3.20(b). This effect is partly caused by an imbalance of dislocation formation [231]. Furthermore, the pre-existing terraces are unfavorably added to the ones generated by the relaxation process. Lastly, the roughness almost doubles from $RMS_{Ref}$ =2.54 nm to $RMS_{6deg}$ =4.68 nm.
Utilizing offcut samples is hence not completely unfeasible. However, it would necessitate substantial benefits in other parts of the structure to justify the considerable loss of crystalline quality inside the MMB, which is not given for the applications at hand.

### 3.5.7 Total structure thickness

Although the target thickness for a λ-cavity InGaAs structure is 450 nm, several photonic devices necessitate a different value. Of the various sections comprising the device, the inverse and the capping layer are most readily varied because this leaves the strain engineering intact. Thus, this section investigates flexibility in terms of the thickness of those layers.

**Surface roughening:** The first investigated property is the nature of the progressive surface roughening, described in section 3.2.1.6, for the complete jump-convex-inverse MMB structure. For this purpose,

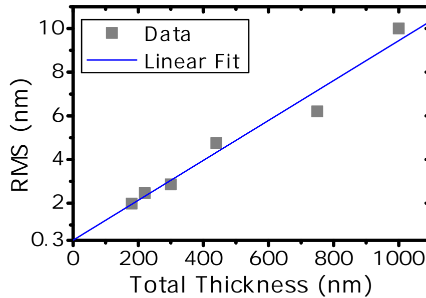


**Fig. 3.21.** Roughness of jump-convex-inverse MMB structure for which the total thickness is varied by changing the inverse plus capping region thickness. QD growth was omitted.

structures with default 30 nm+130 nm thick jump-convex region and varying inverse plus capping layer thickness were grown. QD growth was omitted to exclude its influence. The RMS over the total thickness is plotted in Fig. 3.21. As demonstrated by the linear fitting curve in blue with an $R^2$ of 0.9603, the roughening behavior is clearly still active for the unstrained layers up to a total thickness of 1000 nm. Therefore, while the effect is, in principle, obviously caused by the metamorphic growth mode, it is also uncoupled from the relaxation process itself, as discussed previously. The effective roughening coefficient is $\Delta\text{RMS} = 0.0091 \pm 8 \cdot 10^{-4}$, which is lower than reported in section 3.2.1.6 for ungraded layers due to the intermediate optimizations. Furthermore, a y-axis intercept at an RMS of $0.3{\pm}0.4$ nm close to the (0/0) point signifies that possible biasing contributions (from the metamorphic relaxation plus the base roughness of the wafer versus the critical thickness as the delayed starting point of the roughening) are counteracting each other for the complete structure. Thus, a proportional dependency can be assumed for the purpose of predicting the roughness of a specific MMB design. Lastly, advanced 2D/3D strain-sensitive experiments are expedient for a better understanding of this roughening phenomenon, e.g., analysis of the

degree of polarization in PL [232] or coherent X-ray multiangle Bragg projection ptychography [233].

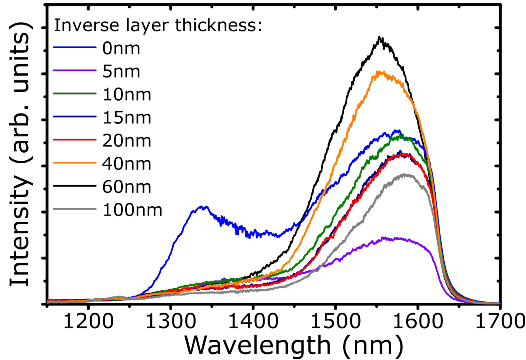


**Fig. 3.22.** Ensemble-PL spectra of QD/MMB samples with varying inverse layer thickness.

**Inverse layer thickness:** Whenever the design of the jump-convex-inverse MMB is changed, independent of the strain engineering, it has to be considered that the surface of this structure serves as substrate for the QD deposition. Due to the susceptible nature of the QDs, even slight variation, e.g., the progressive roughening discussed above, can greatly influence their formation.
Fig. 3.22 shows PL curves of samples with different inverse layer thicknesses. For increased reliability spectra at a total of five detection spots were measured and averaged. The 60 nm reference sample exhibits the brightest emission, which is somewhat expected, because this is the thickness used during the QD optimization. Completely omitting the inverse step and depositing the QD directly on top of the convex-layer is the most radical variation, since it changes the substrate nature from relaxed to residually strained. The curve shape is strongly affected and displays an additional bright peak around 1340 nm wavelength. Markedly, the sample still has considerable

emission inside the telecom C-band, with a reduction of only 40 % compared to the reference.
In contrast, including a thin inverse layer with 5 nm thickness leads to significant further deterioration of this emission and produces the overall dimmest sample. However, the slightly thicker designs with 10 nm/15 nm/20 nm of inverse layer remedy this effect and result in peaks with around 50 % of reference brightness. Furthermore, The QD ensemble emission is almost re-established for a 40 nm thick inverse layer. Lastly, an increase of the thickness beyond the reference value to 100 nm results in the second dimmest structure.
Obviously, brightness in ensemble PL is of secondary importance for the more critical properties connected to single-photon emission, because it can be caused by changing area density as well as single QD emission quality. Also no respective in-depth μ-PL investigation has been performed at this point. Nevertheless, the crucial point drawn from the measurement at hand is that the QD deposition is certainly influenced by any changes to its virtual substrate. This has to be considered for any modifications that are made for specific photonic cavity designs and might necessitate proper adaptation of the QD growth recipe in each case.

**Capping layer thickness:** Additional roughness caused by a thicker capping layer is less critical than for the inverse region, although it might complicate lithography processes at some point. However, more importantly, the process of progressively covering the QD layer has to be examined appropriately.
For this purpose, samples with a standard 220 nm thick jump-convex-inverse MMB, a default QD plus AnnCap section, and ascending capping layer thickness were grown. Entirely omitting any additional capping and stopping after the annealing step leads to the surface depicted in Fig. 3.23(a). At this point in the growth, the smaller optically active QDs are already covered, while larger InAs clusters are typically partly desorbed and redistributed during the annealing step [234]. Instead of the expected hole formation [235], the usual

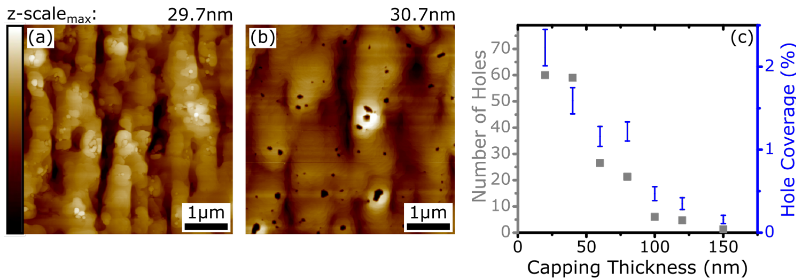


**Fig. 3.23.** AFM analysis of QD hole capping: (a) 5 µm x 5 µm scan of the surface after QD and AnnCap growth plus annealing. (b) Exemplary scan for 20 nm capping thickness showing approximately 60 distinct holes fully within the scanning area. (c) QD/MMB samples with varying capping layer thickness: Number of holes and percentage of hole area.

cross-hatch morphology is supplemented with several 2-5 nm high islands accumulating in the hillock regions. This observation can be explained by insufficient annealing time/temperature for complete desorption. These residual islands are responsible for the formation of holes during overgrowth.
Fig. 3.23(b) displays the surface after 20 nm capping layer. 60 distinct holes are fully visible as black circles within the scanning region covering ≈2.2 % of the total area. This morphology is caused by the high strain energy, specifically at the edge of the indium-rich islands [236]. Consequently, adatom migration away from the strained islands is enhanced, and the growth speed of lattice-matched $In_{0.287}GaAs$ on top is reduced [237]. This effect impedes an elimination of the holes via diffusion and necessitates a delayed closing from the sidewalls. In order to quantify this procedure, 5 µm x 5 µm AFM surface scans of the samples with progressive capping were analyzed by determining the number of holes and relative hole area. The result of this analysis is shown in Fig. 3.23(c). A steady decline in hole number and area is observed. At 100 nm thickness, the coverage is reduced by a factor of ≈5 to <0.5 %. Complete vanishing of the pattern is reached for

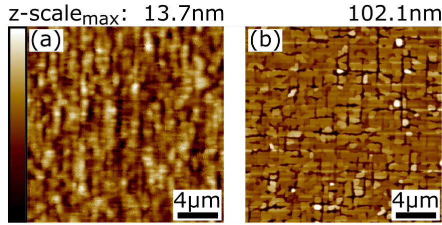


**Fig. 3.24.** AFM scans of 200 nm thick $In_{0.287}GaAs$ layers: (a) full growth process at 595 °C; (b) deposition at 595 °C followed by 20 min annealing at 710 °C.

around 150 nm of capping. At this point, slightly more than a single hole remains on average within the 5 µm x 5 µm area.
In conclusion, for structure design based on the proposed QD recipe, a minimal capping layer thickness of 100 nm to 150 nm is recommended.
**Error sources:** A correct masking for hole determination is complicated by the superimposed cross-hatch structure, causing an unreliable hole depth and edge level. For some AFM scans, it was impossible to set a masking filter z-level for all holes at once and necessitated a stitching approach for which multiple masks were set and their data combined. Moreover, for capping thicknesses >60 nm, three separate scans were evaluated for better averaging. The entire data set can be found in Appendix 6.3.

### 3.5.8 Annealing

Thermal annealing can be a powerful tool to heal defects inside crystalline layers [238] and influence the surface topography by inducing diffusion. On the other hand, detrimental effects like indium desorption have to be considered.

The first annealing test was performed to determine if the optimized growth temperature of 595 °C is only necessary to provide a nucleation layer [239, 240] and can be increased to the standard growth temperature of 710 °C at later stages. Fig. 3.24 shows AFM surface

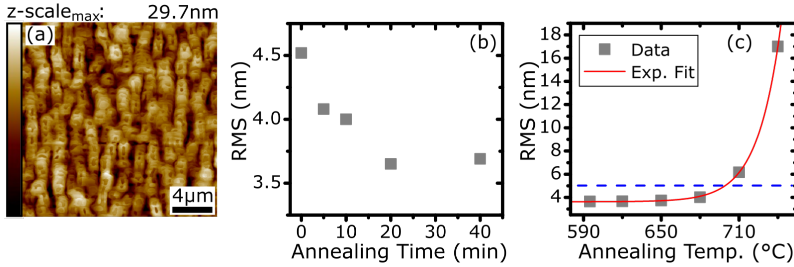


**Fig. 3.25.** Impact of annealing on surface roughness of jci-MMB: (a) AFM scan of the surface after 20 min of annealing at 595 °C of 440 nm structure with direct cooling down afterward. (b) Surface RMS of the structure being annealed for various times after 390 nm growth and 50 nm post-annealing deposition. (c) Surface RMS for 20 min annealing time at different temperatures. An exponential fitting curve is drawn in red. The dashed blue line marks the roughness level without annealing.

scans for 200 nm thick $In_{0.287}GaAs$ with and without heat treatment. The reference sample (Fig. 3.24(a)) exhibits an RMS of 1.86 nm, in line with previous results. In contrast, subjecting the layer to 710 °C for 20 min leads to significant surface quality degradation, as shown in Fig. 3.24(b), including a high RMS of 12.1 nm. Notably, the surface morphology is similar to the one observed for elevated initial growth temperatures (cf. Fig. 3.4(c), note the different scale). It can therefore be concluded that the smoothening effect at lower temperatures described in section 3.2.1.3 is unstable at 710 °C.
Next, the impact of annealing on the unstrained inverse/capping layer was investigated. Fig. 3.25(a) displays the surface of a 440 nm thick structure with full jci-design but omitted QD deposition, subjected to a 20 min growth interruption at 595 °C before cooling down. The typical cross-hatch structure is modified by shallow (2-10 nm) holes, which are elongated in $[01\bar{1}]$ direction, appearing centrally on top of the hillocks. The effect is connected with a RMS reduction of ≈7 %. This indicates a limited amount of levelling mass transport, which is, however, counteracted by the hole appearance. Inserting

the same growth interruption after 390 nm of grown structure and following it up with the remaining 50 nm capping deposition utilizes the smoothening more efficiently and results in ≈19 % reduced RMS. Additionally, the 50 nm post-annealing deposition re-establishes the default surface morphology by eliminating the holes. This procedure is thus used for further annealing studies as well.
The impact of different interruption times at 595 °C is shown in Fig. 3.25(b). A mostly linear smoothening is discovered between 0 min and 20 min annealing. This effect saturates for higher annealing times, and no additional RMS reduction was observed for 40 min of growth interruption. Therefore, the variation of annealing temperature was performed for a set time of 20 min. As displayed in Fig. 3.25(c), the best smoothening is obtained for basic $T_{\mathrm{Ann}}$ =595 °C, and the surface remains largely stable up to 650 °C. At even higher temperatures, the additional roughening effect escalates and exceeds the RMS without annealing. Notably, XRD measurements on the sample heated to 680 °C showed no change in the indium composition proving thermal stability in this regard.
The roughening behavior can be fitted by the function (red line)

$$\mathrm{RMS}(T_{\mathrm{Ann}}) = 3.63\,\mathrm{nm} + 0.004\,\mathrm{nm} \cdot \exp\left\{\frac{T_{\mathrm{Ann}} - 868.15\,\mathrm{K}}{17.9\,\mathrm{K}}\right\} \quad (3.3)$$

with an $\mathrm{R}^2$ of 0.9999. The excellent agreement of this function illustrates the thermal activation of the roughening process, i.e., the underlying exponential behavior of the surface diffusion. It is, however, insufficient to quantify the energy barrier via, e.g., Arrhenius analysis [241] because the observed value is the RMS instead of a reaction coefficient. More targeted measurements would be necessary in that case [242].
Nevertheless, the most important conclusion from this data is the limit for heating during a deoxidation step as preparation for the overgrowth of structured samples. While the default temperature of 710 °C is inaccessible, deoxidation of the InGaAs surface at 680 °C feasible and is utilized in section 4.3.

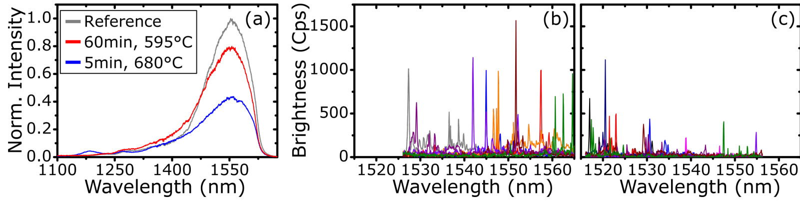


**Fig. 3.26.** Temperature stability of QD growth: (a) Ensemble PL spectra of QD/MMB structures with post-annealing after the capping layer deposition. (b) µ-PL of reference DBR sample with default QD recipe, 5 nm AnnCap and 7 min annealing at 595 °C. (c) µ-PL of DBR sample with additional 60 min post-annealing at 595 °C.

#### 3.5.8.1 QD temperature stability

The emission properties of the QDs grown with the final recipe in section 3.3 were only considered for direct cooling down after 220 nm capping layer deposition. However, various base structures for photonic devices necessitate further overgrowth. The stability of the QDs during this additional time at elevated temperatures is investigated here.
Fig. 3.26(a) shows ensemble spectra of the reference structure with direct cooling down compared to annealed samples. 60 min at 595 °C, the growth temperature of the capping layer, reduces the peak height by ≈20 %. Heating the structure to 680 °C for a brief 5 min has an even bigger impact and halves the emission intensity. This limited temperature budged for InAs QDs in (In)GaAs matrix is caused by continuous diffusion even after capping and typically also causes a blue shift [243], which is not observed here.
In order to evaluate the impact for single-photon applications, µ-PL measurements were performed because the brightness decrease could be caused by a reduction of QD area density as well as individual emission quality. Fig. 3.26 displays µ-PL QD spectra from DBR samples with (b) reference cooling down and (c) 60 min post-annealing at the 595 °C. The shift in wavelength is due to the fabrication tolerances of

the DBR. The brightness of typical emission lines is clearly negatively impacted by the additional heating period. This observation is critical for possible structural adaptations for photonic devices discussed in chapter 4. It increases the necessity for a second-generation QD recipe, possibly with larger QDs, for better resistance to diffusion processes [244].

Chapter 4

# Photonic devices

The aim of depositing QDs with C-band emission on top of a thin-film MMB was to unlock diverse approaches for the fabrication of high-quality single-photon sources. In this context, the final structure discussed in the previous chapter (3), namely 220 nm jci-MMB/QDs/230 nm cap, represents the most basic of all possible implementations. Depending on the targeted photonic device, several adaptations have to be made to the original design.
These growth adaptations, their corresponding devices, and a short overview of the resulting optical properties will be discussed in this chapter.
The optical measurements that are displayed in the following were performed by Cornelius Nawrath, Pascal Pruy and Raphael Joos. Electrical measurements were conducted by Julian Maisch, Michael Zimmer and Jonathan Ensslin. Structural fabrication was carried out by Stephanie Bauer, Sascha Kolatschek, Ponraj Vijayan, Michael Zimmer and Jens Jakschik.

## 4.1 Planar cavity with bottom DBR

The simplest approach to enhance extraction efficiency for a GaAs-based MOVPE-grown emitter is the addition of a bottom DBR. This structure forms only a very weak cavity in terms of Purcell enhancement and extraction efficiency. Nevertheless, this makes it an excellent

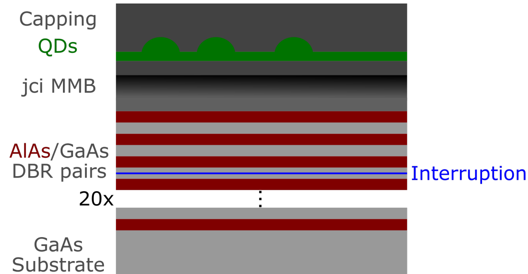


**Fig. 4.1.** Schematic drawing of the two-step growth process. The first 20 AlAs/GaAs pairs of the DBR are deposited in an Aixtron Close Coupled Showerhead©reactor. The final 3 pairs and the QD/MMB structure are grown in an AIX-200 horizontal reactor.

benchmark for QD properties since those are not overwritten by strong cavity characteristics. Furthermore, sufficient brightness can be delivered to allow for acceptable signal-to-noise ratios while measuring quantum optical figures of merit (e.g., single-photon purity). Lastly, as a planar cavity, it allows access to a large number of emitting QDs, making it suitable for recording emission data with sufficient statistics to enable reliable statements about the quality of the QDs.
Notably, the structure has already been extensively utilized during the QD growth recipe optimization in section 3.3, but its optical properties will be discussed in more detail here. Finally, the addition of the AlAs/GaAs DBR underlines the compatibility of the jci-MMB with typical AlGaAs functional layers.
The optical measurements in this section have been partly published in Ref. [183]; see also Ref. [245].

**Two-stage DBR growth:** To provide a stop-band centered around 1550 nm, each DBR pair has to consist of 114.6 nm GaAs plus 134.4 nm AlAs. This circumstance means that the necessary 20 (or more) pairs to reach sufficient reflectivity are more than 5 µm thick, which usually results in a considerable time and material investment for the

growth of this structure. Therefore, a two-step deposition process was implemented, as shown in Fig. 4.1.
Since the standard substrate size used for epitaxy in this work is 1/6 of a 2" wafer or 1/12 of a 3" wafer (approximately equal in total area), the first 20 DBR pairs were prepared on full 2"/3" wafers via an Aixtron Close Coupled Showerhead©reactor with high deposition rates. This first fabrication step was finished with 50 nm of GaAs to avoid critical oxidization of the upper AlAs layer. The wafer was then cleaved into pieces under normal atmospheric conditions, which could then be mounted separately into the reactor of the AIX-200. This machine was then used to deposit the 3 uppermost DBR pairs to ensure sufficient spacing between the growth interruption and the active layer inside the MMB/QD structure. Notably, 3 nm was added to the first GaAs layer to compensate for the losses during the deoxidation of the substrate.
This two-step hybrid growth procedure represents a considerable resource reduction, which allowed for the straightforward fabrication of a large number of QD/MMB/DBR structures.

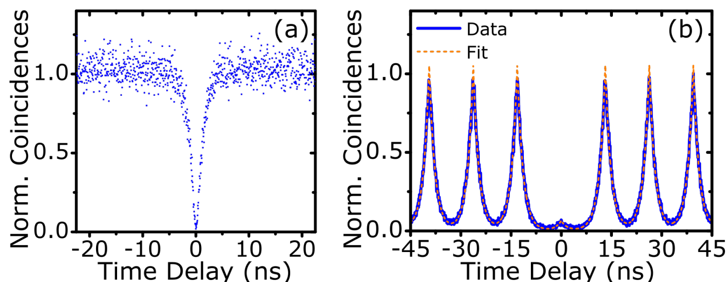


**Fig. 4.2.** Second-order auto-correlation measurement of exemplary QD transition lines: (a) cw excitation, (b) pulsed excitation.

### 4.1.1 Optical characterization

**Single-photon purity:** The ability of the QDs to provide pure single-photon emission was investigated first. For this purpose, second-order auto-correlation measurements in non-resonant excitation were performed. The data was acquired using superconducting nanowire single-photon detectors with an efficiency of $> 80\,\%$. It is displayed with a binning of 50 ps. Fig. 4.2(a) shows coincidence data from a QD emission line using a cw laser with a mean total count rate of 76.9 kcps and integrating for 45 min. A clear dip is visible around zero time delay, which signifies a strong anti-bunching as the hallmark of non-classical light. However, even more meaningful for prospective applications is the $g^{(2)}(\tau)$ under pulsed excitation displayed in Fig. 4.2(b). Here, a distinct suppression of the central peak can be observed, which coincides with only a minor bunching on time scales of up to $\pm 2.5\,\mu$s. Precise $g^{(2)}(0)$ values can be obtained by evaluating peak area, only applying a correction for detector dark counts. Comparing the zero time delay peak with the mean of multiple peaks in the Poisson level by taking the sum over all associated data point bins yields a value of $9.4(4)\,\%$. Alternatively, the pulse areas can be calculated through their contribution to the orange fit function. This evaluation results in $g^{(2)}(0) = 6.11(9)\,\%$. Performing this analysis for other QDs on the

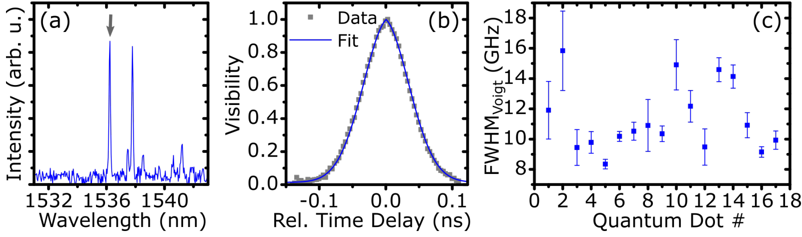


**Fig. 4.3.** Measurement of the linewidth for a QD/MMB/DBR structure via determination of the first-order coherence function $g^{(1)}(\tau)$ under continuous-wave, non-resonant excitation in saturation: (a) µ-PL spectrum of an exemplary QD transition. (b) $g^{(1)}(\tau)$ measurement data (grey) and fit function (blue) for the transition marked with an arrow in (a).
(c) Linewidths (FWHM) of 17 QD transitions. Values were calculated from Voigt fit functions of the corresponding measurements.

sample has found similar values. The detected single-photon purity substantially outperforms the results reported for the same excitation scheme and linear-MMB-based structures ($g^{(2)}(0) = 18.4(2)\,\%$) [82]. In addition to these high emission-quality QDs, a second species was discovered that makes up approximately 50 % of all observable QDs. The associated emission lines exhibited a similarly high brightness level in above-band cw excitation. However, a strong refilling on ns-timescales associated with a biexponential decay was observed. This effect leads to a peak overlap, and in its most extreme form manifests as second-order auto-correlation data in pulsed excitation measurements that looks similar to the cw case (see Appendix 6.4). A possible reason for this phenomenon are charged trap-states in the vicinity of these QDs, which are caused by crystal defects. This explanation is especially plausible due to the metamorphic nature of the matrix material and the associated dislocations.

**Linewidth via first-order correlation function:** In order to precisely evaluate the range of linewidths that the QD transition peaks exhibit beyond the resolution limit of the spectrometer, first-order

coherence measurements were performed in a free-space Michelson interferometer. Here, non-resonant, cw excitation was used to reach saturation conditions for the examined transition lines. The emission count rate was then determined as a function of the path delay relative to the current position of a motorized delay stage with a travel range of $\pm 75\,\mathrm{mm}$. Subsequently, the resulting data could be fitted with a sine function from which the visibility was extracted after taking into account the detector dark counts and the non-unity visibility of the setup due to alignment imperfections ($\sim 3\,\%$). This trace of the visibility over the relative temporal delay $\tau$ is proportional to the first-order coherence function $g^{(1)}(\tau)$. By fitting it with the Fourier transform of a Voigt function, both homogeneous (Lorentzian) and inhomogeneous (Gaussian) broadening are considered [246]. Fig. 4.3(a) and (b) show the µ-PL spectrum and the Voigt function fit of the visibility for an exemplary QD transition. The evaluated line is marked with a grey arrow in the spectrum. The analysis was performed for 17 distinct QDs, and all resulting linewidths are displayed in Fig. 4.3(c). The error bars indicate the uncertainty calculated via error propagation from the $1\sigma$ confidence bound of the fit routine. A mean value for $\mathrm{FWHM}_{\mathrm{Voigt}}$ of 11.3 GHz (46.7 $\mu$eV) with a standard deviation of 2.2 GHz (9.1 $\mu$eV) could be determined. Moreover, broadening contributions of $\gamma_{\mathrm{Gauß}} = 9.5 \pm 2.9\,\mathrm{GHz}$ and $\gamma_{\mathrm{Lorentz}} = 2.4 \pm 2.1\,\mathrm{GHz}$ could be established. All absolute FWHM values, as well as the ratio between homogeneous and inhomogeneous broadening, compare well with results obtained for QDs grown on a linearly-graded MMB [87].

**Fine-structure splitting:** The average FSS of the QDs has already been used as a quality measure for their deposition parameters in section 3.3. Here, a more comprehensive study with extended statistics is displayed for the final QD growth recipe.

Fig. 4.4(a) shows the µ-PL spectrum of an exemplary QD under non-resonant, cw excitation at saturation. Of the distinct emission lines, two are marked with a green and a red arrow. The energy

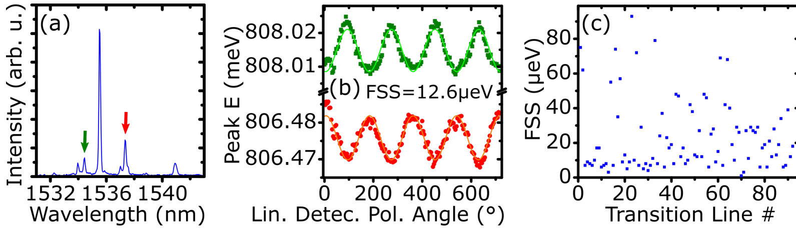


**Fig. 4.4.** Measurement of the FSS for QDs on MMB/DBR structure under cw, non-resonant excitation in saturation: (a) µ-PL spectrum of an exemplary QD. The analyzed transitions are marked with colored arrows. (b) Energetic position of the transition lines marked in panel A for varying linear detection polarization. The determined FSS for this pair is 12.6 µeV. (c) FSS of the transition lines of 26 exemplary QDs.

of these peaks can be determined via a Gaussian fit function. In Fig. 4.4(b), the resulting peak energy is plotted depending on the linear detection polarization angle for 180 spectra equally spaced for a range from 0 ° to 720 °. Oscillations with the same amplitude and a phase difference of 90 ° can be observed for the evaluated emission line pair. This behavior is the fingerprint of a biexciton-exciton pair. Actually, only 7 of the 26 investigated QD positions exhibited this clear-cut behavior. The energy oscillation of a single line without an appropriate partner was observed for the rest. Nevertheless, this data was still included in the results. The FSS value can then be calculated as twice the amplitude of the fitted sine function (12.6 µeV for the example). The outlined analysis has been performed for all 26 QD positions, and the results are displayed in Fig. 4.4(c). A mean FSS of 23.4 µeV with a standard deviation of 20.6 $\mu$eV can be extracted from the data. Furthermore, the detailed presentation of all data reveals that high FSS outliers strongly influence this value. Markedly, ≈37 % of the data points lie within the ≤10 µeV range, even though possible contributions from transition lines with FSS<1 µeV are excluded due to resolution limits. Another ≈23 % is located between 10 µeV and ≤20 µeV. Hence, a majority of QD possess FSS properties within the

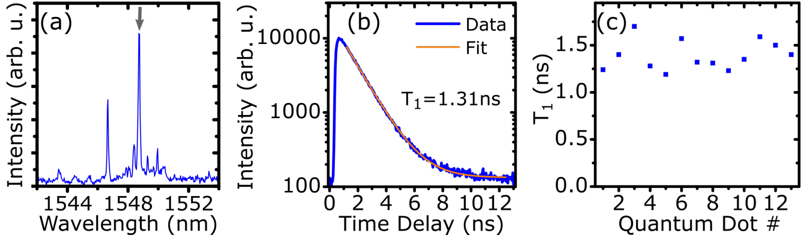


**Fig. 4.5.** Decay time measurements for QD/MMB/DBR structure: (a) μ-PL spectrum of an exemplary QD under pulsed, non-resonant excitation in saturation. (b) TCSPC data (blue) and fit (orange) of the decay time of the marked transition line in panel (a) under weak excitation. The determined $T_1$ for this transition is 1.31 ns. (c) Decay times of 13 exemplary QDs.

easily accessible range of prominent tuning schemes [247, 248], which makes these emitters promising candidates for low-FSS entanglement applications [249]. The presented statistic is also more favorable than for their high-quality droplet-etched InAs/InP counterparts [62]. Overall, InAs QDs grown on the thin jci-MMB exhibit similar quality in terms of low FSS as for deposition on a thicker linearly-graded MMB [82].

**Decay time:** The decay time is the last figure of merit analyzed for the weak planar cavity with bottom DBR. Here, QD positions were first located under pulsed, non-resonant excitation in saturation. A respective μ-PL spectrum can be seen in Fig 4.5(a). Subsequently, the brightest transition line, marked here with a grey arrow, is analyzed by measuring the decay trace via time-correlated single-photon counting (TCSPC) for weak excitation. The exemplary measurement is shown in Fig. 4.5(b). As expected, the detected counts exhibit a sharp rise shortly after the trigger pulse of the excitation laser. This feature is then followed by a small plateau caused by the time jitter of the charge carrier relaxation into the QD potential. Finally, exponential

decay is observed, which can be fitted accordingly (orange, solid line). In the case of a mono-exponential behavior, a single $1/e$-decay time $T_1$ can be extracted, which was true for 11 out of the 13 investigated exemplary QDs. Note that in order to equate the decay time with the radiative lifetime $T_1$, one has to assume negligible non-radiative decay channels. The full statistic is displayed in Fig. 4.5(c). The mean value is 1.39 ns with a standard deviation of 0.16 ns. Therefore, the decay time is largely similar to the values of $1.4 \pm 0.4$ ns [82] and $1.71 \pm 0.46$ ns [87] found for QDs deposited on a linearly-graded MMB.

In conclusion, a comparison of the optical figures of merit presented in this section with literature values for QD grown on an InGaAs MMB with linear design shows highly similar properties. At the same time, the jci-MMB exceeds its counterpart in terms of surface quality, flexibility, compatibility and integrability (cf. sections 3.4 and 3.5). These results represent an excellent foundation for the more advanced structures discussed in the following sections.

## 4.2 Planar cavity with bottom and top reflector

The next step for many fully MOVPE-grown photonic structures is the deposition of a top DBR in addition to the established bottom DBR. This is a standard design for the fabrication of Vertical-Cavity Surface-Emitting Lasers [250], which can also utilize telecom-wavelength QDs as an active laser medium [251]. Naturally, it also enhances single-photon emission properties [252]. Finally, this structure also serves as the planar base for the lithography of micro-pillar cavities [253].
The most straightforward approach for the metamorphic $In_{0.287}GaAs$ material system at hand is a lattice-matched $In_{0.271}AlAs/In_{0.287}GaAs$ top DBR. This configuration loses $\approx 30\,\%$ of contrast compared to AlAs/GaAs. However, with a $\Delta n$ of $\approx 0.36$, it still outperforms the alternatives on InP substrate, like InP/InGaAlAs with $\Delta n = 0.34$ and

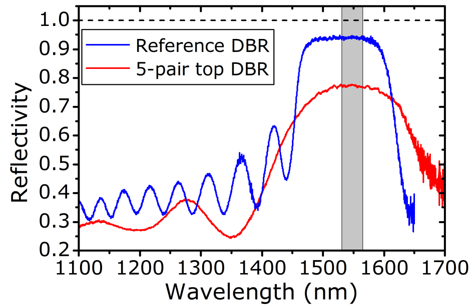


**Fig. 4.6.** Reflectivity measurements of reference 20-pair AlAs/GaAs DBR and 5-pair InGaAs/InAlAs DBR grown on top of jci-MMB. The telecom C-band is marked in gray.

InAlAs/InGaAlAs with $\Delta n = 0.3$ [172]. The potential to fabricate an efficient reflector with this approach is apparent once a high-quality growth of the respective layers has been achieved.
The first step was to grow InAlAs with the correct composition, for which the TMIn and $AsH_3$ flux were held constant, and the TMAl flux varied. Furthermore, the utilized structure consisted of the standard jump- and convex-layers, followed by 200 nm of InAlAs and capped with 30 nm of $In_{0.287}GaAs$ for oxidation protection. At 24.4 $\frac{\mu mol}{min}$, the XRD measurement revealed $In_{0.269}AlAs$ for the layer composition, which is very close to the calculated value and can thus be considered lattice-matched. This structure exhibits an RMS of 5.09 nm, which is considerably higher than the expected roughness for full realization with InGaAs of 3.85 nm (cf. section 3.5.7). Thus, a dedicated growth parameter optimization for InAlAs might be favorable but has been omitted here.
With both DBR materials available, a sample consisting of 450 nm jci MMB (without QDs; λ-cavity) and 5 pairs of 125 nm $In_{0.269}AlAs$ and 112 nm $In_{0.287}GaAs$ was fabricated. Here, the two thicknesses were estimated by extrapolation because there are no exact literature values for the optical density of the two materials at 1550 nm and 4 K. Since it

is bolstered by the semiconductor-air interface, calculations according to equation 2.20 predict a maximum reflectivity of ≈89 % for this structure. The respective room-temperature reflectivity-measurement, and a comparison to a standard 20-pair AlAs/GaAs DBR designed for the telecom C-band, are shown in Fig. 4.6. The 5-pair InGaAs/InAlAs DBR features a well-calibrated stopband position and a maximum reflectivity of ≈77 %, which is reasonably close to the theoretical value considering the reduced efficiency due to intermixing [254]. As expected, the stopband is less angular and displays a larger FWHM than the reference. However, although these optical properties are promising, the issue with the structure is its high roughness of RMS=19.2 nm. This excessive RMS results from the large thickness of >1 μm inducing progressive surface roughening as described in section 3.5.7. Therefore, at this point in time, sufficiently high numbers of top DBR pairs for a strong cavity confinement can not be deposited without rendering the surface unsuitable for lithography to produce, e.g., micropillars.

## 4.3 Gaußian-shaped cavity

A related alteration of the planar Fabry-Perot resonator with bottom and top DBR is the Gaußian-shaped cavity. This approach was first proposed in 2013 by Ding et al. [255] and can be seen as a refined form of the mesa structure [256, 257]. Due to smoothly curved sidewalls, the cavity exhibits high Q-factors and minimal mode volume. It is hence especially suitable to provide high-quality confinement for single-photon emitters like QDs. However, while the design and its corresponding simulations are auspicious, actual physical fabrication remains challenging. The first steps towards a realization for C-band QDs based on the jci-MMB can be found in Ref. [258]. The following chapter gives a summary of the sections that pertain to peculiarities of MOVPE overgrowth with an InGaAs/InAlAs top DBR.
The compatibility of the QD/jci-MMB design with AlAs/GaAs bottom DBRs and the λ-cavity thickness represents a good base for the construction of a Gaußian-shaped resonator. The respective

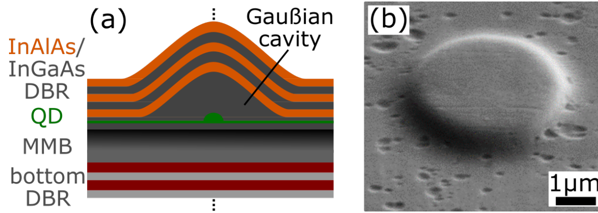


**Fig. 4.7.** (a) Schematic drawing of Gaußian-shaped cavity based on a jci-MMB with InAlAs/InGaAs top DBR. (b) SEM image of mesa structure with smooth Gaußian sidewalls after wet-chemical etching, before top DBR overgrowth.

schematic design, including an InAlAs/InGaAs top DBR, is displayed in Fig. 4.7(a). Simulations have shown that the ideal total cavity height is identical to the planar Fabry-Perot case at 450 nm. Therefore, any calibrated bottom DBR structure, as described in section 4.1, is an appropriate starting point for fabrication. Furthermore, the lens etching procedure described in Ref. [259] is readily adaptable to the InGaAs material system and the required cavity dimensions. Fabrication after wet-chemical etching, but before top DBR overgrowth, results in the structure shown in Fig. 4.7(b). Here, a slightly simplified design consisting of Gaußian-shaped sidewalls enveloping a micro-mesa was chosen. All elevated areas are sufficiently smooth, and the mesa height can be developed at the appropriate edge depth for confinement at 1550 nm wavelength. The holes in the etched region are most likely linked to the QD layer, as described for Fig. 3.23.
Consequently, the next step is MOVPE overgrowth. The first aspect that must be considered here is the necessary heating before layer deposition to remove the unintentional oxide layer from exposure to the atmosphere. Based on the results presented in section 3.5.8, to maintain surface stability, a temperature of up to 680 °C can be applied. This value is slightly below the default 710 °C used for GaAs wafer priming. Therefore, the deoxidation time was doubled from 5 min to 10 min to compensate for the lower set point. This proce-

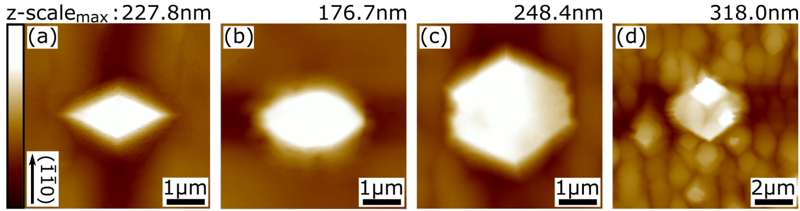


**Fig. 4.8.** AFM scans of Gaußian-shaped lens overgrowth.
Deposition of 257 nm $In_{0.287}GaAs$ with: (a) standard capping layer growth parameters, (b) increased temperature of 680 °C, (c) increased V/III ratio of 201. (d) Surface after growth of 4 pairs InAlAs/InGaAs top DBR.
The sideways indentations on the lower etching level are AFM measurement artifacts due to the tips scan direction.

dure proved sufficient for oxide removal. Another, even more critical constraint on the thermal budget is given by the QD stability, as described in section 3.5.8.1. However, this effect already occurs at far too low temperatures for feasible oxide removal. It is thus not further discussed in this section and will have to be solved by adapting the QD growth recipe.
A further challenge is preserving symmetry and Gaußian shape of the lens structure during overgrowth. For simplicity, actual InAlAs growth was omitted for this investigation because the indium diffusion is the dominating process that has to be optimized [260, 261]. Fig. 4.8(a) shows the etched and overgrown structure after depositing 257 nm of lattice-matched $In_{0.287}GaAs$, which is equal to the thickness of a single InAlAs/InGaAs DBR pair, with standard growth parameters. The structure exhibits a diamond-like shape, including an elongation by a factor of 2 in [011] compared to $[0\bar{1}\bar{1}]$ direction. Importantly, the sidewalls have a slope angle of ≈15 ° and are hence no pure facets. Nevertheless, the shape is caused by imbalanced facet growth speed. First, the base is four-sided due to faster lateral expansion in (011) than in (010) directions. However, this effect alone would result in a square geometry. The elongation is, therefore, likely induced by

an imbalance between the group-III-led $[111]/[1\bar{1}\bar{1}]$ facet system and the group-V-led $[1\bar{1}1]/[\bar{1}11]$ one. This fast deterioration of the lens shape through anisotropic faceting is clearly unsuitable for cavity purposes. As displayed in Fig. 4.8(b), an elevated growth temperature of 680 °C leads to less sharp edges and an overall rounder geometry. This is probably due to a more kink-driven atom incorporation at enhanced thermal activation [262]. Moreover, a regular hexagonal shape is produced at an increased V/III ratio. This geometry change manifests through the formation of pronounced $[0\bar{1}1]/[01\bar{1}]$ edges. As a consequence, the extension in $[1\bar{1}\bar{1}]$ direction equalizes to ≈2 µm, while the $[1\bar{1}1]$ dimension remains constant compared to the default case. This result can be assigned to suppressed diffusion of group-III atoms.

With the described progress in controlling the facet growth, deposition of a full InAlAs/InGaAs top DBR could be tackled. For two DBR pairs, the Gaußian lens shape is still mostly preserved, albeit with a considerably increased RMS of 10 nm. This proves that inserting an Al-containing layer is mostly straightforward once the In diffusion behavior is optimized. However, as displayed in Fig. 4.8(d), overgrowing four InAlAs/InGaAs pairs results in a sample surface dominated by underlying undulations and emerging hillocks. Therefore, similar to the planar case, the overarching roughening behavior (cf. section 3.5.7) foils the implementation of thick epitaxy on top of the QD/MMB cavity. Notably, one relevant deduction that can be made from these observations is that the protruding nature of the lens has no decisive impact on the source of the progressive roughening.

In any case, this challenge has to be solved first to enable the fabrication of Gaußian-shaped cavities with InAlAs/InGaAs epitaxy. However, the top DBR can alternatively be constructed by utilizing other material systems. More information on these approaches can be found in Ref. [258].

## 4.4 Circular Bragg grating cavity

A major goal of the jci-MMB design was to enable the fabrication of advanced photonic cavities for the telecom C-band. One such unlocked structure is the circular Bragg grating cavity. It is highly promising due to its low mode volume facilitating high Purcell enhancement and broadband increase of extraction efficiency.
A recent approach to fabricating circular Bragg grating cavities is via a flip-chip process in which the SC material is employed as a membrane [263]. Two adjustments must be made to the default QD/MMB structure for this role. One is the reduction of the total InGaAs section thickness from 450 nm to 360 nm. The other is inserting a 1000 nm thick $Al_{0.70}GaAs$ sacrificial layer between MMB and GaAs substrate. Both assignments were readily realized by exploiting the flexibility of inverse and capping layer thickness and utilizing the inherent compatibility of the jci-design with bottom AlGaAs structures. The main side-effect that has to be considered for this adapted design is the impact of the thinner inverse section on the QD deposition, as described for Fig. 3.22. Consequently, as mentioned before, a dedicated QD growth optimization for best emission quality would be advisable in the future.
The SEM scan of an exemplary circular Bragg grating structure realized in 360 nm thick metamorphic InGaAs via electron-beam lithography and chemical dry etching is displayed in Fig. 4.9(a). It has a trench width of 200 nm, a pitch of 560 nm and a central mesa diameter of 1174 nm. Combined with the membrane thickness, these dimensions result in a cavity mode wavelength inside the telecom C-band. Accordingly, the cavity peak in Fig. 4.9(b) is positioned at $\approx$1556 nm. The spectral mode under strong, non-resonant pumping has a FWHM of 9.7$\pm$1.8 nm, which corresponds to a Q-factor of $\approx$160. The circular Bragg grating structure has been fabricated without employing deterministic positioning techniques, which severely limits the probability for spatial matching of the integrated QD emitters [264].

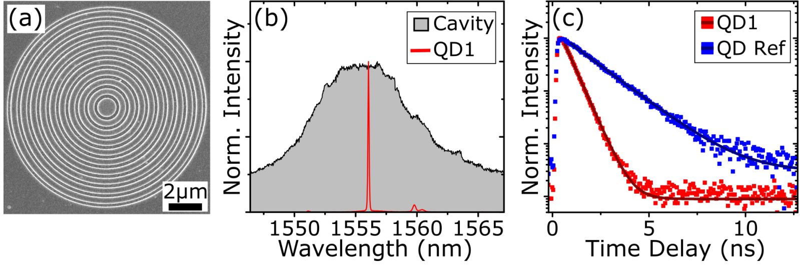


**Fig. 4.9.** Circular Bragg grating cavity based on jci-MMB (reproduced after [265]): (a) SEM top view of the fully fabricated structure. (b) Spectrum of the cavity mode under strong, non-resonant pumping with a FWHM of 9.7±1.8 nm. Overlapping emission under pulsed p-shell excitation of QD1 inside the cavity. (c) Semilogarithmic plot of TCSPC measurement on QD1 compared to reference QD located in the planar sample region. Includes fitting functions as darker lines.

Nevertheless, the cavity at hand contains the sufficiently well-positioned QD1. Furthermore, the emission spectrum of QD1 under pulsed p-shell excitation (red line) exhibits excellent wavelength matching to the cavity mode. The resulting Purcell enhancement is illustrated in Fig. 4.9(c). A decay time of 1.59 ns was measured for a reference QD located in the planar region of the sample, hence outside any cavity structures. This property is consistent with the value of 1.39±0.16 ns established in section 4.1, albeit in the upper decay time range. In contrast, QD1 exhibits a significantly shorter decay time of 0.52 ns, which entails a Purcell enhancement of ≈3. Further measurements on this device established a fiber-coupled single-photon count rate of 4.77 MHz at 76 MHz repetition rate of the excitation laser. The corresponding collection efficiency into the first optical element (NA= 0.6) is 17.4 %. This outstanding brightness coincides with excellent single-photon purity demonstrated by an analytical $g^{(2)}(0)$ of 0.7±0.4 %. Based on these figures of merit, the portrayed circular-Bragg-grating device constitutes the best-performing telecom C-band single-photon emitter reported at the time of this work. Specifically, this includes

all approaches realized via the InP material platform [266–270]. More detailed information on the optical properties of the circular Bragg grating device can be found in Ref. [265].

## 4.5 Grating outcoupler

Quantum integrated circuits are a promising platform for compact quantum information processing. Nevertheless, for some applications, like the linkage of distinct nodes, a stable fiber-to-chip connection is necessary. Here, grating couplers are favorable as they have shown high coupling efficiencies and good alignment tolerances for the SOI platform [271, 272]. In this work, the MOVPE growth concept of contributing an emitter at 1550 nm to this approach will be briefly outlined.

Naturally, grating coupler devices are critically characterized by their total efficiency in transferring light. Apart from the possibility of designing the grating in a certain way, using a backside mirror offers the prospect of increasing the coupling efficiency drastically. Record values of 0.5 dB were demonstrated using a back-etched Al mirror [272]. However, it is complex to realize such a reflective component via etching a hollow into the bottom material and subsequent metal deposition since it requires pinpoint processing from both substrate sides.

The layer structure displayed in Fig. 4.10 is the base of an alternative, monolithic path. Here, all necessary layers are monolithically deposited on GaAs substrate first. The $Al_{0.95}GaAs$/GaAs pairs are then transformed into an $Al_2O_3$/GaAs backside DBR via wet thermal oxidation. The larger refractive index contrast compared to the conventional AlAs/GaAs material system results in a 10-times broader stopband, while on the other hand, only 5 pairs are needed. This allows high reflectivity at sufficiently large angles of incidence to reflect all the light otherwise transmitted into the substrate back toward the coupling interface. The next layer is $\geq$800 nm thick $Al_{0.95}GaAs$, which is also designated for oxidation and will constitute the cladding layer.

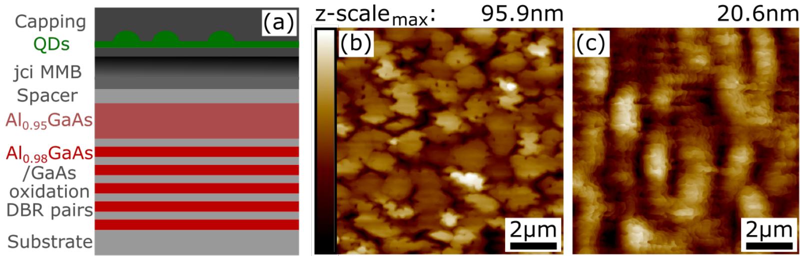


**Fig. 4.10.** MOVPE deposition of the base structure for grating outcouplers: (a) Schematic drawing of planar layers designed for oxidized DBR bottom reflector and the oxidized cladding layer. (b) AFM scan of the sample surface without GaAs spacer. (c) AFM scan of the sample surface with 40 nm GaAs spacer.

After 0-40 nm of GaAs spacer, the jci-MMB is deposited, followed by QDs and cap. The overall InGaAs region has a thickness of 340 nm to 360 nm depending on the exact design of the outcoupler structure. The impact of the GaAs spacer is illustrated in the difference between Figs. 4.10(b) and (c). In the first one, the AFM scan of the full structure but without a spacer is shown. It displays a flake-like surface morphology with a large RMS of 12.9 nm. This topography is almost certainly arising due to the surface waviness of the AlGaAs layers disturbing the metamorphic relaxation process. Generally, the small lattice mismatch between the GaAs substrate and AlGaAs allows the epitaxy of thick layers without exceeding the critical thickness and switching into the metamorphic regime. Nevertheless, the strain build-up inside these layers and the influence of impurities leads to surface undulations for large thicknesses, especially on exactly oriented substrates [273, 274].
For the case at hand, this effect markedly constitutes the limits of the jci-MMBs compatibility with the AlGaAs material system. Both, 1000 nm of $Al_{0.70}GaAs$ (circular Bragg grating cavity), and 134.4 nm of AlAs after 22 pairs of 114.6 nm GaAs/134.4 nm AlAs (bottom DBR structure) are suitable for immediate InGaAs deposition. Nonetheless,

800 nm of $Al_{0.95}GaAs$ on top of 5 pairs of 250 nm $Al_{0.98}GaAs$ and 114.6 nm GaAs apparently exceeded this tolerance threshold. The described waviness effect can, however, be compensated by sufficient pure GaAs deposition. Therefore, a 40 nm GaAs spacer layer was inserted between the AlGaAs and the InGaAs section for the sample displayed in Figs. 4.10(c). Evidently, this procedure is sufficient to smoothen the AlGaAs undulations enough to allow MMB growth with re-established typical surface morphology with an RMS of 3.62 nm.

## 4.6 PIN diode

The transition from optical to electrical excitation is a logical next step for the QD/MMB structure. For this purpose, a respective positive-intrinsic-negative (PIN) diode structure has to be realized. However, the epitaxy of doped metamorphic InGaAs is especially challenging because of its simultaneous role as high-quality MMB. As shown in section 3.2, the available growth parameter space is considerably limited. In the following, multiple options for each doped layer are explored by growing 500 nm of InGaAs on undoped GaAs substrate. All non-dopant precursor fluxes are adopted from the final values in the jump layer optimization. The samples are analyzed via 4-contact rectangular Van der Pauw Hall measurement. The goal is then to design and fabricate a complete PIN diode sample. Finally, electrical and optical measurements are performed to determine the quality of the structures.

### 4.6.1 p-side doping

The first investigated p-dopant was carbon. It is a prime choice for a PIN structure containing delicate QDs, because of its low-diffusion properties in GaAs-based material systems [275]. Additionally, it allows for very high doping concentrations ($> 1 \cdot 10^{20}\,\mathrm{cm}^{-3}$) [276].
In MOVPE, the organic groups released after pyrolysis can be utilized as a carbon source. This effect is typically observed for low

**Table 4.1.** Samples for the investigation of $CBr_4$ carbon doping in 500 nm thick InGaAs.

| # | $CBr_4$ flux | TMIn flux | $In_x$ | RMS | carrier density |
|---|---|---|---|---|---|
| D1 | 0 $\frac{\mu mol}{min}$ | 8.4 $\frac{\mu mol}{min}$ | 26.4 % | 3.32 nm | $< 5 \cdot 10^{16}\,cm^{-3}$ |
| D2 | 1.0 $\frac{\mu mol}{min}$ | 10.3 $\frac{\mu mol}{min}$ | 27.5 % | 3.17 nm | $2.92 \cdot 10^{17}\,cm^{-3}$ |
| D3 | 4.8 $\frac{\mu mol}{min}$ | 14.4 $\frac{\mu mol}{min}$ | 26.7 % | 4.79 nm | $4.53 \cdot 10^{17}\,cm^{-3}$ |
| D4 | 10.3 $\frac{\mu mol}{min}$ | 10.3 $\frac{\mu mol}{min}$ | 7.4 % | 0.86 nm | – |

temperatures and low V/III ratio [277], which makes it feasible for the metamorphic InGaAs used in this thesis. Therefore, the first step was to fabricate a layer without active doping. The result is shown as sample #D1 in table 4.1. No detectable doping concentration was measured, which signifies minimal carbon incorporation. However, in turn, this means that the intrinsic layer of the PIN structure can be fabricated using the previously optimized growth parameters. Markedly, the RMS of 3.32 nm for this InGaAs layer on undoped substrate is significantly lower than the extended reference on default GaAs:Si (4.6 nm). This behavior is unintuitive because Si-doped wafers are typically of superior quality than undoped ones [1]. The effect is possibly caused by the unintentional presence of surfactants [278] due to impurities being flushed out of the wafer during heated oxide layer removal. Alternatively, a higher density of TDs in the substrate could catalyze the relaxation by serving as additional nucleation centers for MDs [197]. Further investigation is certainly advisable.
In a more conventional approach, $CBr_4$ can be used as an external carbon source. Here, a carrier concentration of $2.92 \cdot 10^{17}\,cm^{-3}$ was measured for a flux of 1.0 $\frac{\mu mol}{min}$. However, from this point, multiplying the $CBr_4$ flux 5-fold only increased the doping level by a factor of ≈1.5. This indicates a maximal reachable p-doping level within the constraints of the MMB growth parameters of around $4.5 \cdot 10^{17}\,cm^{-3}$, which is insufficient for most applications. In Ref. [279], Keiper et al. were able to reach $1.6 \cdot 10^{19}\,cm^{-3}$ at V/III= 2, $T = 500\,°C$ and

[1] http://www.axt.com/site/index.php?q=node/34

**Table 4.2.** Zinc and Silicon doping levels and RMS roughness for various precursors fluxes in 500 nm thick $In_{0.265}GaAs$.

| Dopant | # | precursor flux | carrier density | RMS |
|---|---|---|---|---|
| none | D1 | $0.0\ \frac{\mu mol}{min}$ | $< 5 \cdot 10^{16}\ cm^{-3}$ | 3.32 nm |
| Zinc | D5 | $6.75\ \frac{\mu mol}{min}$ | $6.47 \cdot 10^{17}\ cm^{-3}$ | 4.21 nm |
| | D6 | $13.5\ \frac{\mu mol}{min}$ | $1.66 \cdot 10^{18}\ cm^{-3}$ | 3.87 nm |
| | D7 | $52.6\ \frac{\mu mol}{min}$ | $2.09 \cdot 10^{19}\ cm^{-3}$ | 3.00 nm |
| Silicon | D8 | $4.47\ \frac{nmol}{min}$ | $3.34 \cdot 10^{17}\ cm^{-3}$ | 4.08 nm |
| | D9 | $8.94\ \frac{nmol}{min}$ | $6.53 \cdot 10^{17}\ cm^{-3}$ | 4.07 nm |
| | D10 | $44.7\ \frac{nmol}{min}$ | $4.50 \cdot 10^{18}\ cm^{-3}$ | 4.11 nm |

$0.069\ \frac{nm}{s}$ for $In_{0.53}GaAs$. However, they also reported significantly decreasing values for higher temperatures, V/III ratios and growth speeds, all of which is the case for the structures at hand. Furthermore, while the roughness remains stable for low $CBr_4$ fluxes, a considerably enhanced RMS is observed for sample #D3. This effect coincides with a modification of the surface morphology (see Appendix 6.5). Finally, another unfavorable aspect of $CBr_4$ is its strong back-etching effect on InGaAs that influences growth rate and composition [280]. This circumstance necessitated an adaptation of the TMIn flux to stabilize the indium content to ≈27 % for samples #D1, #D2 and #D3. A counterexample with insufficient indium compensation is displayed as sample #D4. Here, XRD measurements showed a severe In content reduction to 7.4 %, which also explains the considerably lower roughness. Therefore, carbon was dismissed as a viable p-dopant for the jci-MMB.

The next candidate is zinc, which exhibits a much stronger diffusion behavior [281], but can be applied, without considering back-etching or passive sources within the reactor. The DMZn fluxes with the resulting carrier concentrations of 3 samples are displayed in table 4.2. First off, a maximum doping level in the $10^{19}\ cm^{-3}$ range was reached, which is a sufficient level for most purposes. Furthermore, a comparison between samples #D5 and #D6 shows that doubling the precursor

flux increased the carrier concentration by a factor of ≈2.6. In sample #D6, a further quadrupling of DMZn supply led to an additional ≈12.6-times increase. This super-linear dependency signifies a strong interaction of zinc with lattice defect sites, which is consistent with the literature [282, 283]. The notion is reinforced by the fact that surface roughening is observed for low zinc concentrations that transitions to a slight smoothening effect for higher doping levels. Furthermore, the effect coincides with a pronounced mosaicity in the [011] direction, which is visible in the respective RSMs (see Appendix 6.6).
The applied dopant level of sample #D7 was then cross-checked for usage in the full 450 nm jci-MMB structure. Here, ≈11 % smoothening relative to the reference with RMS=4.52 nm was observed, which is consistent with the 10 % difference between samples #D7 and #D1. Furthermore, the strong mosaicity prevented a precise determination of indium contents and strain situation via XRD. Overall, the observed changes in surface topography and crystal quality will likely disturb QD growth. Consequently, zinc doping of the MMB has to be considered carefully, especially for the region below the QDs.

### 4.6.2 n-side doping

Silicon is the focus for n-side doping since it is the default choice for shallow n-dopant in GaAs and exhibits only a slight diffusion behavior [284]. Nevertheless, the amphoteric nature of Si in InGaAs [285, 286] prompts additional attention.
First tests were performed using $SiH_4$ as precursor. However, the optimized MMB growth temperature of 595 °C proved too low for efficient pyrolysis. This finding is in line with other studies, specifically in combination with $AsH_3$, as was the case here [287]. Therefore, $SiH_4$ was discarded as a precursor choice and substituted with the low-temperature compatible $Si_2H_6$ alternative.
The resulting carrier density and surface roughness for three different precursor fluxes is displayed for samples #D8, #D9 and #D10 in table 4.2. A comparison shows that the doping concentration behaves proportionally to the applied $Si_2H_6$ flow in the examined range. More-

over, the highest measured value of $4.50 \cdot 10^{18}\,\mathrm{cm}^{-3}$ is sufficient for most applications. At the same time, it stays well below the maximum stable activation limit in $In_{0.53}GaAs$ of $\approx 1.50 \cdot 10^{19}\,\mathrm{cm}^{-3}$ [288]. This limit is associated with a considerably enhanced Si diffusion [289] that should be strictly avoided for QD structures.
Furthermore, the Si doping causes 24 % roughening compared to the undoped reference. However, this effect is caused by the general presence of silicon during layer growth and is independent from the actual amount. Additionally, the surface topography is maintained even at higher concentrations, and HRXRD measurements of the Si-doped layer show no discernable deviations in terms of indium content and relaxation. Finally, the cross-check for the doped (#D10 level) 450 nm jci-MMB structure shows a consistent increase of the RMS by ≈22 %.
In conclusion, Si-doping allows to supply sufficient and flexible carrier concentrations and influences the surface topography predictably. This makes it the best material among the examined candidates for doping the InGaAs layer below the QDs in terms of preserving crystalline quality.

### 4.6.3 PIN diode structure

With the above-defined p- and n-doped as well as intrinsic InGaAs layers, the construction of an entire 450 nm PIN structure was tackled. According to the results above, the most straightforward design starts with a GaAs:Si substrate. Two samples with different intrinsic layer thicknesses were grown with this approach. In the first sample, the MMB is Si-doped ($4.50 \cdot 10^{18}\,\mathrm{cm}^{-3}$ ) up to 40 mm below the QD layer. Following another intrinsic spacer layer, the Zn-doped cap is deposited with a similar doping level of $1.66 \cdot 10^{18}\,\mathrm{cm}^{-3}$, except for the upper 20 nm. That section is doped with $2.09 \cdot 10^{19}\,\mathrm{cm}^{-3}$ to allow for lower contact resistance. This represents a design aiming at minimal intrinsic layer thickness (90 nm total) and is schematically depicted in Fig. 4.11(a). As an alternative, a sample with maximum intrinsic region design was grown. Here, the GaAs:Si is retained, but n-doping of the MMB is completely omitted. Additionally, the p-region is

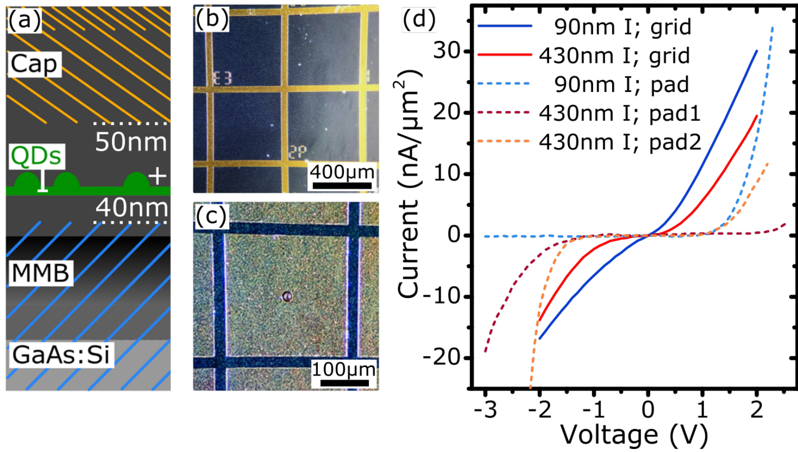


**Fig. 4.11.** Design and investigation of PIN structure:
(a) Schematic of the doped QD/MMB structure. The blue/orange shaded area marks the Si/Zn-doped region. (b) Light microscope picture of grid top-contact. (c) Light microscope picture of pad top-contact. (d) I-V curves of samples with different intrinsic layer thickness and grid/pad contacting.

realized solely through the highly Zn-doped 20 nm thick upper contact layer. Consequently, the intrinsic region of this sample has a total thickness of 430 nm.

For all investigated structures, the n-side contact was implemented by coating the bottom side of the GaAs:Si substrate with gold. However, two different contacting techniques were employed for the p-side. For the first one, a gold grid with 460 μm mesh width is applied on the surface, of which an exemplary section is displayed in Fig. 4.11(b). In this approach, the whole structure is linked and hence forms one single top-contact. This has the advantage that, in principle, the entire sample area can be addressed simultaneously through just one external connection. The second contacting technique uses pad structures, as shown in Fig. 4.11(c). This design utilizes the 250 μm x 250 μm square for wire bonding. Most of this area is insulated from the SC surface,

and the actual current is restricted to the 20 µm diameter window in the center (air-post contacting [290]). This allows for a much more purposeful application of current to a small defined area. However, the drawback is that each pad has to be contacted separately, which limits the examinable area.
For both samples, two 5 mm x 5 mm sample pieces were fabricated, with grid and pad contacting, respectively. The I-V curves of contacted 5 mm x 5 mm sample pieces from both structures are shown in Fig. 4.11(d). The solid lines show the behavior of contacting via a grid. A characteristic diode curve shape is visible to some extent for the sample with a thick intrinsic layer, although with almost no discernable breakdown voltage. However, the sample with the thin insulation section configuration exhibits an almost ohmic response. These observations suggest a damaged intrinsic layer [291]. This explanation is feasible for the structure at hand since, due to the large-scale contacting, a single macroscopic defect could short-circuit the whole system. Moreover, the metamorphic growth could contribute additional week spots due to the introduced lattice dislocations. In line with this explanation, the characteristic curves measured for pad contacting show a pronounced diode behavior independent of the intrinsic layer thickness. Here, the restricted electric current area significantly reduces the impact of localized defects. Nevertheless, the electrical properties of the PIN areas are still markedly dissimilar. This is illustrated by the fact that the two investigated pad contacts on the sample with thick intrinsic layer produce distinctly different curves. More emphatically, the best stability against breakdown current is counter-intuitively observed for the thinner intrinsic layers.
That said, no EL emission could be measured for any sample regardless of the undoped layer or contacting configuration. Furthermore, only the sample with 430 nm intrinsic region showed PL emission around 1550 nm. Therefore, the lack of EL could possibly be traced back to Si diffusion/segregation optically deactivating the QDs. More details can be found in Ref. [292].
All in all, in this chapter, multiple dopant options for the jci-MMB could be excluded, and others were narrowed down. Nevertheless,

the investigation is still rudimentary in terms of carrier concentration and layer thicknesses at this point. Moreover, advanced techniques could also be applied, e.g., delta doping [293]. Furthermore, providing contacting for EL is only one aspect of doped layers, and specific focus could be laid on designs for passive or active stabilization of the QD environment with the goal of reducing the emission linewidth [48, 161].

Chapter 5

# Summary and Outlook

In this thesis, a thin-film InGaAs MMB approach was utilized to fabricate self-assembled InAs QDs serving as single-photon emitters at the technologically important telecom C-band around 1550 nm. Since the structure is based on a GaAs substrate, this allowed full compatibility with the AlGaAs material system for the insertion of functional layers below the InGaAs section. This flexibility adequately enabled the construction of various advanced photonic cavities. Their feasibility and potential for combination with the QD/MMB structure could be evaluated. The presented analysis and optimization of MOVPE growth, as well as device fabrication, lays the groundwork for the development of high-quality non-classical light sources.

As the first step, a non-linear MMB design was introduced with three main goals in mind:

1. Provide the optimal strain environment for InAs QD emission in the telecom C-band.
2. Minimize the necessary layer dimension for the required transition of lattice constant with the aim of staying below $\lambda/2$ optical thickness.
3. Achieve sufficient crystalline and surface quality to facilitate lithography fabrication processes.

The proposed design was comprised of a jump in indium content to initiate the relaxation process quickly. Next followed a convex-up

grading section that rapidly increases the lattice constant further without inducing 3D growth modes. Lastly, the layout was completed with an unstrained inverse composition layer to stabilize the strain environment, and enable flexibility in setting the total thickness.
This jump-convex-inverse design was then realized for an $In_xGa_{1-x}As$ MMB grown via MOVPE. The conducted extensive growth optimization assessed parameters like precursor fluxes, temperature and V/III ratio. This process was mainly guided by AFM and XRD scans providing surface topography, roughness, and relaxation conditions. The final version of the jump layer consists of 30 nm $In_{0.262}GaAs$, grown with 0.49 nm/s at 595 °C and a V/III ratio of 11. Moreover, the grading section reaches a maximum indium content of 38.2 % at ≈72.5 % relaxation within 130 nm. Finally, the inverse and capping layers are 60 nm, respectively 230 nm thick, and are comprised of fully relaxed lattice-matched $In_{0.287}GaAs$. This composition is calibrated to provide the optimal strain matrix for InAs QDs emitting around 1550 nm.
Nevertheless, the QD growth recipe had to be adapted for this particular virtual substrate. Key parameters are a TMIn flux of 9.4 µmol/min for 4 s with a V/III ratio of 310. This material supply results in a low area density for optically active QDs of $3 \cdot 10^6\,\mathrm{cm}^{-2}$, hence an excellent range to address single emitters. Additionally, a deposition temperature of 550 °C minimized shape asymmetry and, thus, exciton fine-structure splitting. Moreover, the ripening time proved the most critical parameter to achieve high brightness, and a range between 7.5 s and 15 s could be determined as favorable. The ripening process was supplemented by combining a 5 nm annealing cap with 420 s annealing time at 595 °C.
Next, the completed, capped QD/MMB system was examined with various methods. AFM scans of the 450 nm thick InGaAs structure revealed an RMS of 4.76 nm and no detrimental influence of inserting the QD layer. Furthermore, analyzing the strain situation in reciprocal space maps recorded via XRD showed all expected peaks in accordance with the design. Finally, STEM scans displayed typical MD and TD characteristics of MMB structures and subtle interactions

with the QDs. Markedly, an absence of phase separation could be reported.
After that, an examination of the growth parameter specificity was performed. In other words, an optimization revision for the full jci-MMB plus capped QDs structure to evaluate their stability against specification drift and identify routes for further enhancement of crystalline quality. Firstly, for the jump layer, neither thickness nor composition shows feasible ways of improvement by changing the default values. Next, a reactor pressure of 100 mbar already constitutes the best regime within the reachable range of the MOVPE machine. Furthermore, a slower growth rate displays a favorable smoothening mainly for thin structures but a diminished effect beyond 450 nm. In this context, the observed linear progressive roughening has to be discussed. Depending on total thickness, this effect develops at a rate of 0.91 nm RMS per 100 nm for data from 180 nm to 1000 nm. It is most likely caused by buried strain fields and impedes the fabrication of thick structures. Furthermore, a negative influence on the performance of the presented QD recipe was determined for deviations from the default inverse layer thickness of 60 nm. Likewise, AFM analysis revealed the formation of holes in the surface for thin QD capping, which can be sufficiently closed after 100-150 nm of InGaAs material. Lastly, the jci-MMB exhibited excellent structural thermal stability up to a temperature of 680 °C. This property unlocks the possibility for fabrication processes that are demanding in this regard, e.g., MOVPE overgrowth. In contrast, however, the QD layer proved susceptible to longer times at elevated temperatures as well as short additional heating steps.
In the final part, a variety of device approaches was assessed. First of all, a QD/MMB/DBR sample was utilized for a more in-depth characterization of QD emitter properties, in addition to the brightness considerations of the previous chapters. An auto-correlation measurement performed in pulsed above-band excitation demonstrated a single-photon purity characterized by a $g^{(2)}(0)$ of 6.11(9) %. Furthermore, an average linewidth of $\mathrm{FWHM}_{\mathrm{Voigt}} = 11.3 \pm 2.2$ GHz was determined via analysis of first-order correlation functions. This

broadening is dominated by an inhomogeneous Gaußian contribution. Time-correlated single-photon counting measurements revealed $T_1 = 1.39 \pm 0.16$ ns as the mean decay time for the ≈85 % of investigated QDs for which mono-exponential behavior could be fitted. Lastly, for the fine-structure splitting, an average value of 23.4 µeV with a standard deviation of 20.6 µeV was extracted by scanning the shift of distinct transition lines depending on the detection polarization angle. Notably, ≈60 % of all examined emission lines exhibit a FFS in the ≤20 µeV range. This constitutes a promising starting point for complementary tuning techniques with subsequent applications in biexciton-exciton cascade schemes. In conclusion, all observed optical characteristics compare well against InAs QDs fabricated on linear MMBs as well as pure GaAs and InP substrates.

Other prospective photonic structures that were evaluated are either planar or Gaußian-shaped cavities featuring an additional top DBR. Here, the previously mentioned roughening of thick layers prohibited a high-quality solution within the current MMB design and material system.

However, much better compatibility was found with the thin-membrane-based circular-Bragg-grating-cavity approach. In this case, the jci-MMB could provide the necessary layout of ≤360 nm InGaAs with the QDs embedded in the center and the AlGaAs etch-stop layer required for processing. As a result, a record-setting single-photon emitting device could be fabricated. It featured a decent Purcell factor of ≈ 3, and was able to produce a fiber-coupled single-photon count rate of 4.77 MHz at an excitation rate of 76 MHz due to a collection efficiency into the first optical element (NA= 0.6) of 17.4 %. Simultaneously, the reported emission exhibited an outstanding single-photon purity, characterized by an analytical $g^{(2)}(0)$ of 0.7±0.4 %.

Moreover, investigations associated with the construction of grating outcouplers revealed the limit of the jci-MMBs compatibility for direct deposition on AlGaAs. In particular, the introduced pre-strain for layers simultaneously having a thickness beyond 800 nm and an aluminium content larger than 95 % critically disturbs the calibrated metamorphic relaxation. Nevertheless, it could be shown that this

restriction can be readily remedied by inserting a thin ($\leq$40 nm) GaAs spacer layer.
Finally, possible doping routes for the InGaAs MMB and capping were explored with two main objectives. First, avoid influencing the relaxation process and crystalline quality. Second, suppress dopant diffusion to prevent foreign atoms from reaching the sensitive QDs, specifically for doped layers within close proximity.
Regarding the p-side, carbon doping could be excluded in passive and active ($CBr_4$ precursor) forms due to its strong impact on indium composition. Moreover, zinc significantly interacted with the InGaAs surface morphology, causing a moderate $\approx$26 % RMS increase for small influx and a minor $\approx$11 % smoothening at high concentrations. On the other hand, n-doping via silicon resulted in consistent $\approx$22 % surface roughening independent of specific doping concentration. The first attempts to construct a full PIN diode revealed the necessity to confine the active zones to small areas to attain proper characteristic curves. Furthermore, the lack of observable EL at this point warrants a more in-depth investigation for the sake of understanding the behavior of the doped QD/MMB system.
In conclusion, the introduced jci-MMB design and its MOVPE-grown InGaAs realization proved a reliable and flexible solution to attain high-quality single-photon emission from InAs QDs inside the telecom C-band. The presented results constitute a major step in enabling the fabrication of devices for communication applications that require non-classical light.

## Outlook:

In many regards, however, the tackled field of utilizing InGaAs MMB substrates for low-density QD deposition via MOVPE is still in its infancy. Nevertheless, the acquired experience could favorably be transferred into further purposeful investigations with the goal of enhancing the system's applicability.
First of all, a thorough understanding and subsequent elimination of the observed progressive roughening effect would unlock approaches

featuring thicker InGaAs/InAlAs structures above the QD section. Among others, this includes geometric microlenses [294], micropillars [295] and Gaußian-shaped cavities [255]. Furthermore, the jci-MMB design has displayed sensible adaptability in terms of thickness and thermal budget without disturbing the strain relaxation process. However, this can not be said for the sensitive QDs, which were affected by most examined influences. One solution could be implementing a QD recipe focusing on increased robustness against, e.g., fabrication steps at elevated temperatures. Here, diffusion-driven depletion in high indium concentration regions is likely a major factor, which could be counteracted by aiming for larger QDs by controlling the AnnCap thickness. A complementary route would be a dedicated optimization of the QD deposition for promising designs with adapted layer thicknesses, like circular Bragg grating cavities. Lastly, a proper handle on doped metamorphic InGaAs layers, specifically in proximity to the QDs layer, would open up exciting possibilities. In particular, this pertains to understanding the interaction of QDs with single/few dopant atoms diffusing into their lattice structure and distinctly preventing this process. In the end, a meticulously constructed PIN diode would enable electrically driven emission and electric stabilization of the charge environment inside the photonic cavities and hence decidedly boost sought-after properties like indistinguishability [161].
Overall, several promising short- and long-term developments are in reach for the InAs QDs plus thin-film MMB approach. Based on the demonstrated properties and potential advancement, this system clearly constitutes an auspicious route for constructing single-photon light sources fulfilling all the technological requirements for the realization of full-scale quantum communication.

# Zusammenfassung und Ausblick; deutsch:

In der vorliegenden Dissertation wurde ein Ansatz aufbauend auf einem InGaAs Dünnschicht metamorphen Puffer (MMB) verwendet, um selbstorganisierte InAs-Quantenpunkte (engl. quantum dots, QDs) herzustellen, die als Einzelphotonen-Emitter im technologisch wichtigen C-Band der Telekommunikation um 1550 nm dienen. Da die Struktur auf einem GaAs-Substrat basiert, ermöglichte dies eine vollständige Kompatibilität mit dem AlGaAs-Materialsystem für das Einfügen von funktionalen Schichten unterhalb des InGaAs-Abschnitts. Diese Flexibilität erlaubte die Konstruktion verschiedener fortschrittlicher photonischer Kavitäten. Deren Realisierbarkeit und das Potenzial für die Kombination mit der QD/MMB-Struktur konnten evaluiert werden. Die vorgestellte Analyse und Optimierung des MOVPE-Wachstums sowie der Bauelementeherstellung legt den Grundstein für die Entwicklung hochwertiger nicht-klassischer Lichtquellen.

Im ersten Schritt wurde ein nichtlineares MMB-Design eingeführt, mit drei Hauptzielen vor Augen:

1. Eine optimale Verspannungsumgebung für die Emission von InAs-QDs im C-Band zur Verfügung stellen.
2. Minimierung der erforderlichen Schichtdimension für den Übergang der Gitterkonstante mit dem Ziel, unterhalb einer optischen Dicke von $\lambda/2$ zu bleiben.
3. Ausreichende Kristall- und Oberflächenqualität erzielen um eine Einbindung in lithographische Herstellungsverfahren zu ermöglichen.

Das vorgeschlagene Design umfasste einen sprunghaften Anstieg des Indiumgehalts um den Entspannungsprozess zügig einzuleiten. Danach folgte ein konvexer Anstieg, der die Gitterkonstante möglichst schnell weiter erhöht ohne 3D-Wachstumsmodi zu induzieren. Schließlich wurde das Layout mit einer unverspannten Schicht mit inverser Zusammensetzung abgeschlossen, um die Verspannungsumgebung zu stabilisieren und eine flexible Einstellung der Gesamtdicke zu ermöglichen.

Dieses sprung-konvex-inverse Design wurde dann für einen mittels MOVPE gewachsen $In_xGa_{1-x}As$ MMB realisiert. Die durchgeführte umfangreiche Wachstumsoptimierung bewertete Parameter wie Ausgangsstoffflüsse, Temperatur und V/III Verhältnis. Dieser Prozess wurde hauptsächlich durch AFM- und XRD-Scans begleitet, welche die Oberflächentopografie, die Rauheit und die Relaxationsbedingungen aufzeigten. Die finale Version der Sprungschicht besteht aus 30 nm $In_{0,262}GaAs$, gewachsen mit 0,49 nm/s bei 595 °C und einem V/III-Verhältnis von 11. Außerdem erreicht der konvexe Bereich einen maximalen Indiumgehalt von 38,2 % bei ≈72,5 % Relaxation innerhalb von 130 nm. Abschließend sind die inverse und die deckende Schicht 60 nm bzw. 230 nm dick und bestehen aus vollständig entspanntem, gitterangepasstem $In_{0,287}GaAs$. Diese Zusammensetzung ist kalibriert um die optimale Verspannungsmatrix für InAs-QDs zu erhalten, die bei 1550 nm emittieren.
Gleichwohl musste das QD-Wachstumsrezept für dieses virtuelles Substrat angepasst werden. Die wichtigsten Parameter sind ein TMIn-Fluss von 9,4 µmol/min für 4 s bei einem V/III-Verhältnis von 310. Diese Materialzufuhr führt zu einer geringen Flächendichte für optisch aktive QDs von $3 \cdot 10^6\,cm^{-2}$. Folglich ein ausgezeichneter Bereich, um Einzelemitter anzusprechen. Desweiteren reduziert eine Abscheidungstemperatur von 550 °C die Asymmetrie und damit die Exzitonen Feinstrukturaufspaltung. Darüber hinaus erwies sich die Reifungszeit als der kritischste Parameter zum Erreichen einer hohen Helligkeit und ein Bereich zwischen 7,5 s und 15 s konnte als vorteilhaft ermittelt werden. Der Reifungsprozess wurde durch die Kombination einer 5 nm Glühkappe mit 420 s Ausglühzeit bei 595 °C ergänzt.
Anschließend wurde das fertige, bedeckte QD/MMB-System mit verschiedenen Methoden untersucht. AFM-Scans der 450 nm dicken InGaAs-Struktur zeigten einen RMS von 4,76 nm und keinen nachteiligen Einfluss durch das Einfügens der QD-Schicht. Darüber hinaus zeigte die Analyse der Dehnungssituation in reziproken Raumkarten, die mittels XRD aufgezeichnet wurden, alle erwarteten Peaks in Übereinstimmung mit dem Design. Schließlich zeigten STEM-Scans MMB-typische Merkmale von Versetzungsfehlstellen und Gleitfehlstellen und

deren subtile Wechselwirkungen mit den QDs. Insbesondere konnte keine Phasentrennung festgestellt werden.
Anschließend wurde eine Untersuchung zur Spezifität der Wachstumsparameter durchgeführt. Mit anderen Worten, eine Optimierungsprüfung für die vollständige sprung-konvex-inverse MMB plus bedeckte QDs-Struktur, um deren Stabilität gegenüber Spezifikationsdrift zu bewerten und Wege zur weiteren Verbesserung der kristallinen Qualität zu identifizieren. Bei der Sprungschicht lassen sich weder bei der Dicke noch der Zusammensetzung durch eine Abweichung von den Standardwerten Verbesserungen erzielen. Außerdem stellt ein Reaktordruck von 100 mbar bereits das beste Regime der MOVPE-Maschine dar. Des Weiteren erzeugt eine geringere Wachstumsrate eine vorteilhafte Glättung vor allem für dünne Strukturen, aber einen verminderten Effekt jenseits von 450 nm. In diesem Zusammenhang muss die beobachtete lineare progressive Aufrauhung diskutiert werden. Abhängig von der Gesamtdicke entwickelt sich dieser Effekt mit einer Rate von 0,91 nm RMS pro 100 nm für Datenpunkte von 180 nm bis 1000 nm. Er wird höchstwahrscheinlich durch vergrabene Verspannungsfelder verursacht und erschwert die Herstellung von dicken Strukturen. Überdies wurde ein negativer Einfluss auf die Leistung der vorgestellten QD-Rezeptur bei Abweichungen von der standardmäßigen inversen Schichtdicke von 60 nm festgestellt. Ebenso zeigte die AFM-Analyse die Bildung von Löchern in der Oberfläche für dünne QD-Kappen, die nach 100-150 nm InGaAs-Material ausreichend geschlossen werden konnten. Schließlich zeigte der sprung-konvex-inverse MMB eine ausgezeichnete strukturelle thermische Stabilität bis zu einer Temperatur von 680 °C. Diese Eigenschaft erschließt die Möglichkeit für Herstellungsprozesse, die in dieser Hinsicht anspruchsvoll sind, z. B. MOVPE-Überwachsen. Im Gegensatz dazu erwies sich die QD-Schicht jedoch als anfällig gegenüber längeren Zeiten bei erhöhten Temperaturen sowie kurzen zusätzlichen Heizschritten.
Im letzten Teil wurden verschiedene Bauelemente untersucht. Zunächst wurde eine QD/MMB/DBR-Probe für eine eingehendere Charakterisierung der QD-Emittereigenschaften herangezogen, zusätzlich zu den Helligkeitsbetrachtungen aus den vorangegangenen Kapiteln.

Eine Autokorrelationsmessung bei gepulster Überbandanregung zeigte eine Einzelphotonenreinheit die durch eine $g^{(2)}(0)$ von 6,11(9) % gekennzeichnet ist. Außerdem wurde eine mittlere Linienbreite von $\mathrm{FWHM_{Voigt}} = 11.3 \pm 2.2$ GHz durch Analyse der Korrelationsfunktionen erster Ordnung ermittelt. Diese Verbreiterung wird von einem inhomogenen Gaußschen Beitrag dominiert. Zeitkorrelierte Messungen der Einzelphotonenzählung ergaben $T_1 = 1.39 \pm 0.16$ ns als die mittlere Abklingzeit für die ≈85 % der untersuchten QDs, bei denen ein monoexponentielles Verhalten gefittet werden konnte. Schließlich wurde für die Feinstrukturaufspaltung ein Durchschnittswert von 23,4 µeV mit einer Standardabweichung von 20,6 µeV extrahiert, indem die Verschiebung verschiedener Übergangslinien in Abhängigkeit vom Polarisationswinkel der Detektion ermittelt wurde. Es ist hervorzuheben, dass ≈60 % aller untersuchten Emissionslinien eine Feinstrukturaufspaltung im Bereich ≤20 µeV aufweisen. Dies ist ein vielversprechender Ausgangspunkt für ergänzende Tuning-Techniken mit daraus folgenden Anwendungen in Biexziton-Exziton-Kaskadenschemata. Zusammenfassend lässt sich sagen, dass alle beobachteten optischen Eigenschaften positiv vergleichbar sind mit denen von InAs-QDs basierend auf linearen MMBs sowie reinen GaAs und InP Substraten.
Andere in Frage kommende photonische Strukturen, die bewertet wurden, sind sowohl planare als auch Gauß-förmige Kavitäten mit einem zusätzlichem oberen DBR. Die bereits erwähnte Aufrauhung dicker Schichten verhindert hier eine hochwertiges Lösungskonzept innerhalb des aktuellen MMB-Designs und Materialsystems.
Eine wesentlich bessere Kompatibilität wurde jedoch mit den auf Dünnschichtmembranen basierenden kreisförmigen Bragg-Gitter Kavitäten festgestellt. In diesem Fall konnte der sprung-konvex-inverse MMB die notwendige Anordnung von ≤360 nm InGaAs, mittigen QDs und einer für die Verarbeitung erforderliche AlGaAs-Ätzstoppschicht zur Verfügung stellen. Als Ergebnis konnte ein rekordbrechendes Einzelphotonen emittierendes Bauelement hergestellt werden. Es wies einen respektablen Purcell-Faktor von ≈3 auf und konnte, dank einer Sammlungseffizienz im ersten optischen Element ($\mathrm{NA} = 0,6$) von 17,4 %, eine fasergekoppelte Einzelphotonenzählrate von 4,77 MHz bei

einer Anregungsrate von 76 MHz erzielen. Zugleich wies die gemessene Emission eine hervorragende Einzelphotonenreinheit auf, gekennzeichnet durch ein analytisches $g^{(2)}(0)$ von 0,7±0,4 %.
Darüber hinaus zeigten Untersuchungen im Zusammenhang mit der Konstruktion von Auskopplern Grenzen auf bezüglich der direkten Abscheidung des MMBs auf AlGaAs. Insbesondere die Vorverspannung von Schichten, die gleichzeitig eine Dicke von mehr als 800 nm und einen Aluminiumgehalt größer 95 % aufweisen, stört die kalibrierte metamorphe Relaxation. Es konnte jedoch gezeigt werden, dass sich diese Einschränkung durch Einfügen einer dünnen ($\leq$40 nm) GaAs-Abstandsschicht unkompliziert beheben lässt.
Schließlich wurden mögliche Dotierungsrouten für den InGaAs-MMB und die Bedeckungsschicht untersucht, mit zwei Hauptzielen. Erstens sollte eine Beeinflussung des Relaxationsprozesses und der kristallinen Qualität vermieden werden. Zweitens sollte eine Diffusion der Dotierung unterdrückt werden, um zu verhindern, dass Fremdatome die empfindlichen QDs erreichen, insbesondere aus dotierten Schichten in deren unmittelbarer Nähe.
Was die p-Seite betrifft, so könnte die Kohlenstoffdotierung in passiver und aktiver (Ausgangsstoff $CBr_4$) Ausführung ausgeschlossen werden, da sie sich stark auf den Indiumgehalt auswirkt. Außerdem interagierte Zink erheblich mit der InGaAs Oberflächenmorphologie und verursachte einen moderaten $\approx$26 % RMS-Anstieg bei niedrigen und eine geringfügige $\approx$11 %-ige Glättung bei hohen Konzentrationen. Auf der anderen Seite führte die n-Dotierung mittels Silizium zu einer konsistenten $\approx$22 % Oberflächenaufrauhung unabhängig von der spezifischen Dotierungskonzentration. Die ersten Versuche, eine vollständige PIN-Diode zu konstruieren, zeigten die Notwendigkeit auf, die aktive Zone auf kleine Bereiche zu beschränken, um verwertbare Kennlinien zu erhalten. Das Ausbleiben einer beobachtbaren Elektrolumineszenz an diesem Punkt sollte in Zukunft eine eingehendere Untersuchung des Verhalten des dotierten QD/MMB-Systems motivieren.
Zusammenfassend lässt sich sagen, dass das vorgestellte sprung-konvex-inverse MMB-Design und seine mittels MOVPE gewachsene InGaAs-

Realisierung sich als zuverlässige und flexible Lösung zur Bereitstellung hochwertiger Einzelphotonenemission von InAs-QDs im C-Band erwiesen haben. Die vorgestellten Ergebnisse sind ein wichtiger Schritt Richtung Herstellung von Bauelementen für Kommunikationsanwendungen, die nicht-klassisches Licht benötigen.

## Ausblick:

In vielerlei Hinsicht steckt das Feld der Nutzung von InGaAs MMB Substraten für die Abscheidung von QDs mit geringer Dichte mittels MOVPE aber noch in den Kinderschuhen. Nichtsdestotrotz könnten die hier gewonnenen Erfahrungen in weitere gezielte Untersuchungen einfließen, um die Anwendbarkeit des Systems zu verbessern.
Zunächst einmal ist ein gründliches Verständnis und die anschließende Beseitigung des beobachteten progressiven Aufrauhungseffekts fraglos empfehlenswert. Dies würde Designs mit dickeren InGaAs/InAlAs-Strukturen oberhalb des QD-Abschnitts ermöglichen. Dazu gehören unter anderem geometrische Mikrolinsen [294], Mikrosäulen [295] und Gauß-förmige Kavitäten [255]. Darüber hinaus hat das sprung-konvex-inverse MMB-Design eine hervorragende Anpassungsfähigkeit in Bezug auf Dicke und Temperaturresistenz gezeigt, wobei der Relaxationsprozess ungestört blieb. Dies kann jedoch nicht über die empfindlichen QDs gesagt werden, die von den meisten untersuchten Einflüssen stark beeinträchtigt wurden. Eine Lösung könnte die Implementierung einer QD-Rezeptur sein, die auf erhöhte Robustheit gegenüber z.B. Herstellungsschritten bei erhöhten Temperaturen abzielt. Hier ist die diffusionsgetriebene Verarmung in Regionen mit hoher Indiumkonzentration wahrscheinlich ein wichtiger Faktor, dem entgegenwirkt werden könnte indem man größere QDs durch Kontrolle der Glühkappendicke anstrebt. Ein zusätzlicher Weg wäre eine gezielte Optimierung der QD-Abscheidung für vielversprechende Designs mit angepassten Schichtdicken, wie z. B. kreisförmige Bragg-Gitter Kavitäten. Schließlich würde eine tiefgreifende Kontrolle über dotierte metamorphe InGaAs-Schichten, speziell in der Nähe der QD-Schicht, spannende Möglichkeiten eröffnen. Dies gilt insbesondere für

das Verständnis der Wechselwirkung von QDs mit einzelnen/wenigen Dotieratomen die in ihre Gitterstruktur diffundieren und einem Verhindern dieses Prozesses. Letztendlich würde eine sorgfältig konstruierte PIN-Diode elektrisch angeregte Emission und die entsprechende Stabilisierung der Ladungsumgebung im Inneren der photonischen Kavitäten ermöglichen. Damit einhergehende Eigenschaften wie Ununterscheidbarkeit könnten so entscheidend verbessert werden [161]. Insgesamt sind mehrere vielversprechende kurz- und langfristige Entwicklungen des InAs-QDs plus Dünnschicht-MMB Ansatzes in Reichweite. Aufgrund der nachgewiesenen Eigenschaften und des potenziellen Fortschritts ist dieses System eindeutig ein vielversprechender Weg für den Bau von Einzelphotonenlichtquellen, die alle technologischen Anforderungen erfüllen.

## Acknowledgement

I would like to thank:

- Frank Bertram and Gordon Schmidt from the Otto-von-Guericke-Universität Magdeburg for providing the STEM images.
- Sergej Vollmer and Stefan Hepp for discussion around MOVPE process performance and cooperative machine maintenance.
- Jelde Elling for performing the SEM measurements.
- Ann-Kathrin Knabel for her advice on colour schemes with high recognisability and comprehensibility for schematics and graphs.

Chapter 6

# Appendix

## 6.1 XRR example

The XRR analysis method has been used to accurately determine the thickness of InGaAs layers with constant indium composition. Additionally, a reference value to the AFM data was obtained for the RMS roughness.

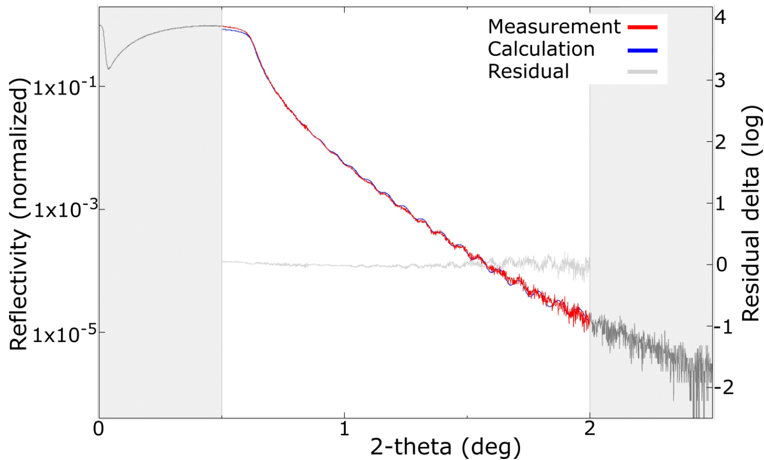


**Fig. 6.1.** XRR scan data with simulated fitting curve and residual fit-error of $In_{0.31}GaAs$ with 100 nm nominal thickness on GaAs substrate. The fit provides a thickness of 102.87(3) nm and an RMS of 1.549(3) nm.

## 6.2 µ-PL spectrum with strong background

Some of the QD recipes investigated in section 3.3 exhibited considerable background. This effect produced a bias into the brightness analysis of individual QD emission lines.

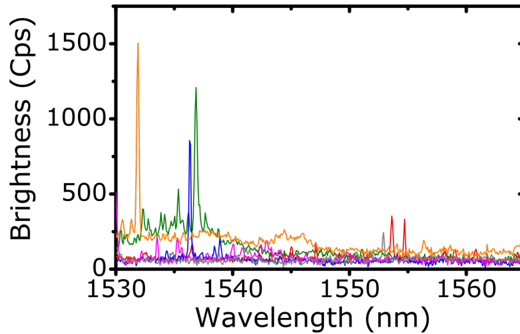


**Fig. 6.2.** µ-PL spectrum at half-saturation of QD/MMB/DBR sample with 10 nm AnnCap and 60 s ripening time showing strong background emission.

## 6.3 Hole analysis QD overgrowth

The hole number and area coverage during consecutive overgrowth of the QD layer was analysed by masking the respective AFM scans. Since the undulations caused by the metamorphic cross-hatch morphology introduce additional levels into the surface, sometimes multiple complementing masks were necessary.

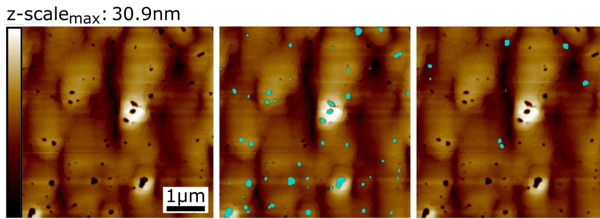


**Fig. 6.3.** AFM scan analysis of QD sample with 20 nm capping layer.
left: raw scan. The scale is valid for all scans.
right: masked scan(s) showing the holes in cyan.

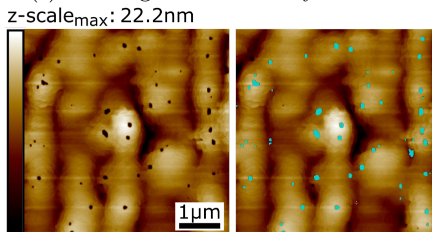


**Fig. 6.4.** AFM scan analysis of QD sample with 40 nm capping layer.
left: raw scan. The scale is valid for all scans.
right: masked scan(s) showing the holes in cyan.

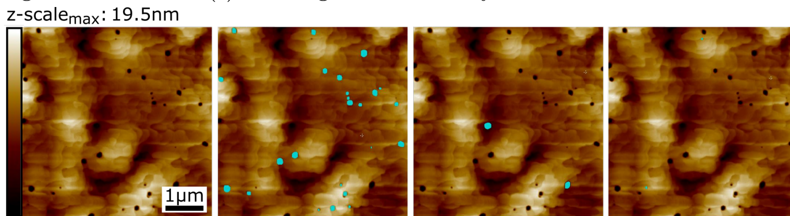


**Fig. 6.5.** AFM scan-A analysis of QD sample with 60 nm capping layer.
left: raw scan. The scale is valid for all scans.
right: masked scan(s) showing the holes in cyan.

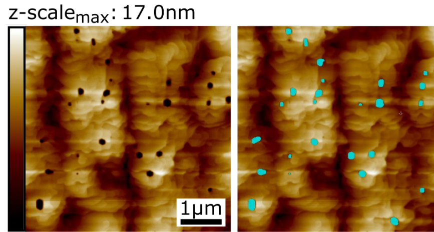


**Fig. 6.6.** AFM scan-B analysis of QD sample with 60 nm capping layer.
left: raw scan. The scale is valid for all scans.
right: masked scan(s) showing the holes in cyan.

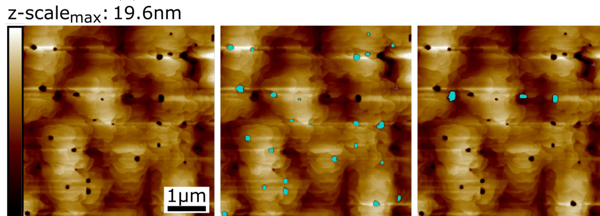


**Fig. 6.7.** AFM scan-A analysis of QD sample with 80 nm capping layer.
left: raw scan. The scale is valid for all scans.
right: masked scan(s) showing the holes in cyan.

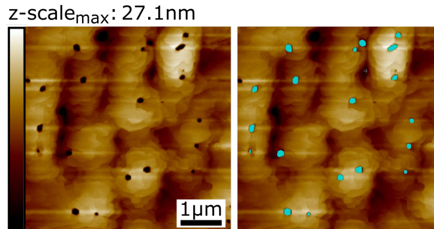


**Fig. 6.8.** AFM scan-B analysis of QD sample with 80 nm capping layer.
left: raw scan. The scale is valid for all scans.
right: masked scan(s) showing the holes in cyan.

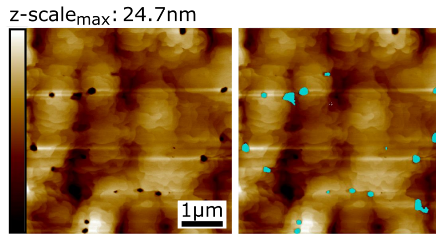


**Fig. 6.9.** AFM scan-C analysis of QD sample with 80 nm capping layer.
left: raw scan. The scale is valid for all scans.
right: masked scan(s) showing the holes in cyan.

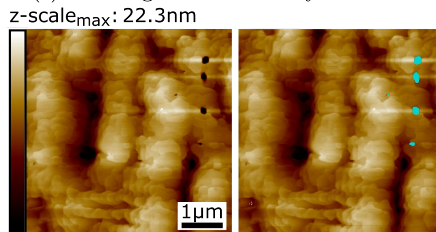


**Fig. 6.10.** AFM scan-A analysis of QD sample with 100 nm capping layer.
left: raw scan. The scale is valid for all scans.
right: masked scan(s) showing the holes in cyan.

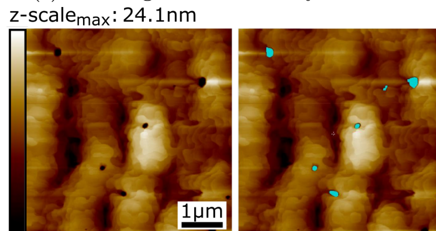


**Fig. 6.11.** AFM scan-B analysis of QD sample with 100 nm capping layer.
left: raw scan. The scale is valid for all scans.
right: masked scan(s) showing the holes in cyan.

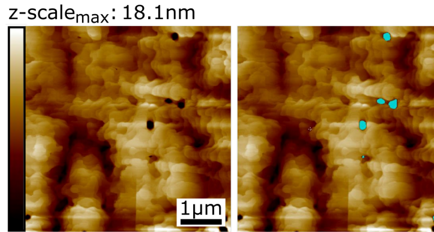


**Fig. 6.12.** AFM scan-C analysis of QD sample with 100 nm capping layer.
left: raw scan. The scale is valid for all scans.
right: masked scan(s) showing the holes in cyan.

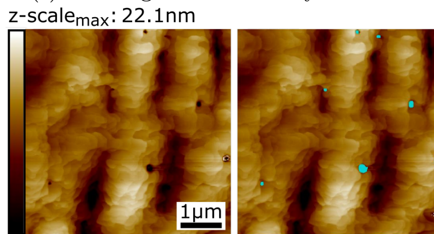


**Fig. 6.13.** AFM scan-A analysis of QD sample with 120 nm capping layer.
left: raw scan. The scale is valid for all scans.
right: masked scan(s) showing the holes in cyan.

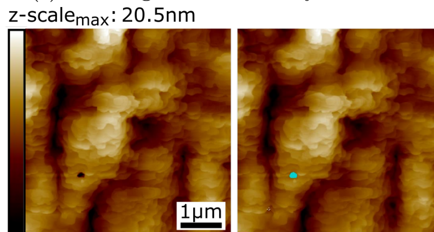


**Fig. 6.14.** AFM scan-B analysis of QD sample with 120 nm capping layer.
left: raw scan. The scale is valid for all scans.
right: masked scan(s) showing the holes in cyan.

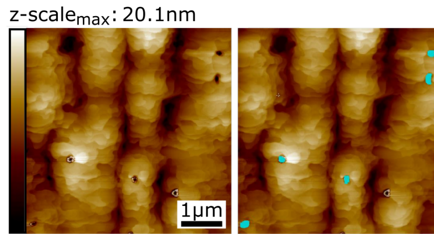


**Fig. 6.15.** AFM scan-C analysis of QD sample with 120 nm capping layer.
left: raw scan. The scale is valid for all scans.
right: masked scan(s) showing the holes in cyan.

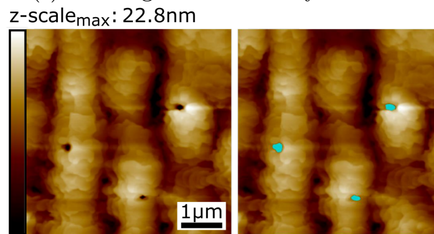


**Fig. 6.16.** AFM scan-A analysis of QD sample with 150 nm capping layer.
left: raw scan. The scale is valid for all scans.
right: masked scan(s) showing the holes in cyan.

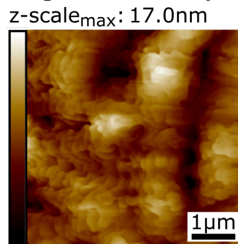


**Fig. 6.17.** AFM scan-B analysis of QD sample with 150 nm capping layer.
Only the raw scan is shown. Zero holes were detected at the scan position.

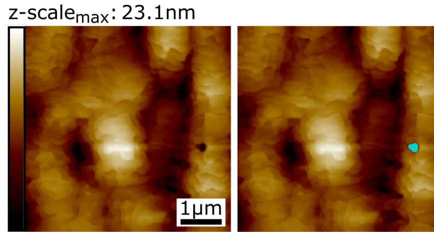


**Fig. 6.18.** AFM scan-C analysis of QD sample with 150 nm capping layer.
left: raw scan. The scale is valid for all scans.
right: masked scan(s) showing the holes in cyan.

## 6.4 Refilling in pulsed second-order auto-correlation measurement

A considerable percentage of the investigated QD emission lines showed a peculiar behavior in their pulsed second-order auto-correlation measurements. The curve shape is similar to the cw excitation case. An effect that is ascribed to strong refilling.

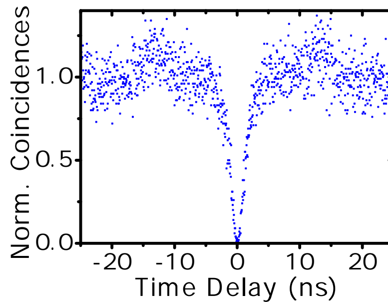


**Fig. 6.19.** Second-order auto-correlation data of exemplary QD from refilling species. The measurement was performed in pulsed excitation. The shape of the graph takes the expected form for cw excitation.

## 6.5 Surface morphology $CBr_4$ doping

The surface structure of carbon doped metamorphic InGaAs layers is dominated by back-etching effects.

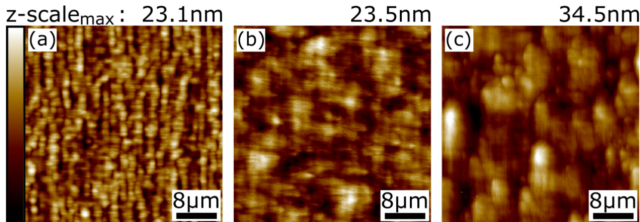


**Fig. 6.20.** AFM scans of 500 nm thick Carbon doped InGaAs using a $CBr_4$ flux of (a) 0 $\frac{\mu mol}{min}$, (b) 1.0 $\frac{\mu mol}{min}$ and (c) 4.8 $\frac{\mu mol}{min}$.

## 6.6 XRD of zinc doped InGaAs

Zinc doping of metamorphic InGaAs layers as well as full jci-structures strongly influences their crystalline structure. An effect that can be clearly observed in RSMs measured via XRD in the form of peak broadening.

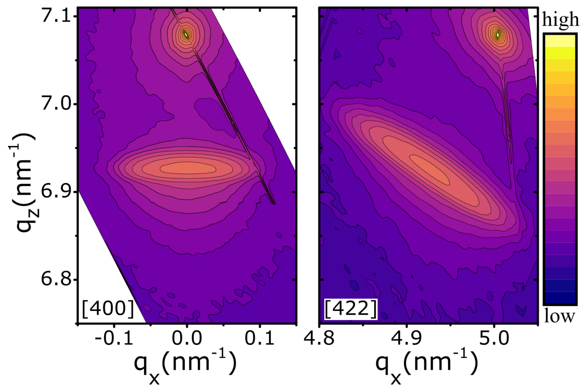


**Fig. 6.21.** RSMs around the (400) (left) and (422) (right) reflex of 500 nm zinc doped InGaAs with $2.09 \cdot 10^{19}\,cm^{-3}$ carrier concentration measured via XRD.

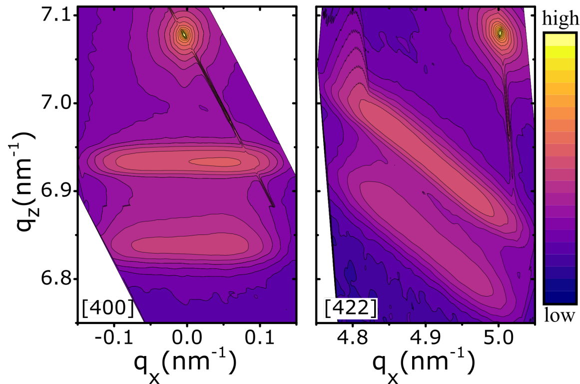


**Fig. 6.22.** RSMs around the (400) (left) and (422) (right) reflex of 450 nm zinc doped jci-MMB structure measured via XRD.

## 6.7 AFM of zinc and silicon doped InGaAs

The influence of zinc and silicon doping on the surface morphology of metamorphic InGaAs was analysed via AFM. Introducing zinc into the layers showed significant impact, while the presence of different levels of silicon exhibited no influence.

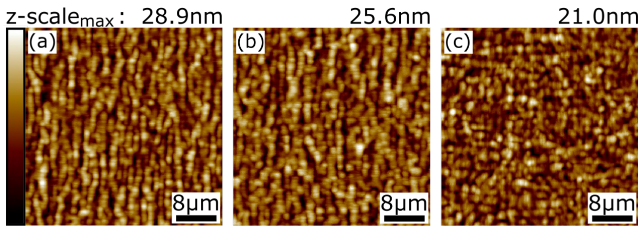


**Fig. 6.23.** AFM scans of 500 nm thick Zinc doped InGaAs using a DMZn flux of (a) 6.75 $\frac{\mu mol}{min}$, (b) 13.5 $\frac{\mu mol}{min}$ and (c) 52.6 $\frac{\mu mol}{min}$.

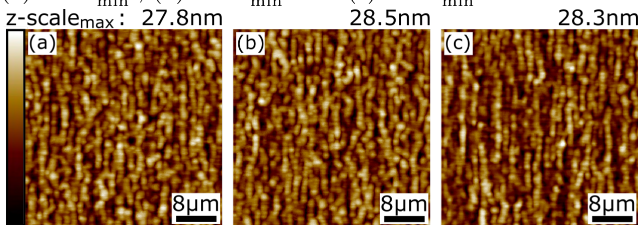


**Fig. 6.24.** AFM scans of 500 nm thick Silicon doped InGaAs using a $Si_2H_6$ flux of (a) 4.47 $\frac{nmol}{min}$, (b) 8.94 $\frac{nmol}{min}$ and (c) 44.7 $\frac{nmol}{min}$.

## 6.8 RSM analysis program

RSMs of various metamorphic structured were evaluated with the help of the following python program. It includes a data reader, purger and converter, a peak finder, and a content determination plus relaxation algorithm.

```
from scipy.optimize import leastsq
#import numpy as np
import matplotlib.pyplot as plt
import sys

import os
import glob
import numpy as np
#from matplotlib.pyplot import figure, show, savefig
from matplotlib import cm, colors
from numpy import ma
# import pylab as plt
#from matplotlib.colors import BoundaryNorm
#from matplotlib.ticker import MaxNLocator
#from mpl_toolkits.mplot3d import Axes3D
import copy
import scipy.optimize
from lmfit import minimize, Minimizer, Parameters,
                              Parameter, report_fit
from operator import itemgetter


def twoD_Gaussian_model_lm(pars, x, y, data):  # Gauss-
                              Funktion fuer Fitvorgang
# unpack parameters:
#  extract .value attribute for each parameter
parvals = pars.valuesdict()
amp0 = parvals['Amp_sub']
x0 = parvals['px_sub']
y0 = parvals['py_sub']
sigma0x = parvals['sigma_x_sub']
sigma0y = parvals['sigma_y_sub']
theta0 = parvals['theta_sub']
amp1 = parvals['Amp_buf']
x1 = parvals['px_buf']
y1 = parvals['py_buf']
sigma1x = parvals['sigma_x_buf']
sigma1y = parvals['sigma_y_buf']
theta1 = parvals['theta_buf']

a0 = (np.cos(theta0) ** 2) / (2 * sigma0x ** 2) + (np.sin(
                              theta0) ** 2) / (2 * sigma0y
                              ** 2)
```

```
b0 = -(np.sin(2 * theta0)) / (4 * sigma0x ** 2) + (np.sin(
                                2 * theta0)) / (4 * sigma0y
                                ** 2)
c0 = (np.sin(theta0) ** 2) / (2 * sigma0x ** 2) + (np.cos(
                                theta0) ** 2) / (2 * sigma0y
                                ** 2)

a1 = (np.cos(theta1) ** 2) / (2 * sigma1x ** 2) + (np.sin(
                                theta1) ** 2) / (2 * sigma1y
                                ** 2)
b1 = -(np.sin(2 * theta1)) / (4 * sigma1x ** 2) + (np.sin(
                                2 * theta1)) / (4 * sigma1y
                                ** 2)
c1 = (np.sin(theta1) ** 2) / (2 * sigma1x ** 2) + (np.cos(
                                theta1) ** 2) / (2 * sigma1y
                                ** 2)

model = (amp0 * np.exp(- (a0 * ((x - x0) ** 2) + 2 * b0 *
                                (x - x0) * (y - y0) + c0 * ((
                                y - y0) ** 2))) + (
amp1 * np.exp(- (a1 * ((x - x1) ** 2) + 2 * b1 * (x - x1)
                                * (y - y1) + c1 * ((y - y1)
                                ** 2)))))

return (model - data)


def twoD_Gaussian_model(x, y, params):  # Gauss-Funktion
                                fuer Plot

# avoid integer problems
amp0 = float(params[0])
x0 = float(params[1])
y0 = float(params[2])
sigma0x = float(params[3])
sigma0y = float(params[4])
theta0 = float(params[5])
amp1 = float(params[6])
x1 = float(params[7])
y1 = float(params[8])
sigma1x = float(params[9])
sigma1y = float(params[10])
theta1 = float(params[11])
```

```
a0 = (np.cos(theta0) ** 2) / (2 * sigma0x ** 2) + (np.sin(
                             theta0) ** 2) / (2 * sigma0y
                             ** 2)
b0 = -(np.sin(2 * theta0)) / (4 * sigma0x ** 2) + (np.sin(
                             2 * theta0)) / (4 * sigma0y
                             ** 2)
c0 = (np.sin(theta0) ** 2) / (2 * sigma0x ** 2) + (np.cos(
                             theta0) ** 2) / (2 * sigma0y
                             ** 2)

a1 = (np.cos(theta1) ** 2) / (2 * sigma1x ** 2) + (np.sin(
                             theta1) ** 2) / (2 * sigma1y
                             ** 2)
b1 = -(np.sin(2 * theta1)) / (4 * sigma1x ** 2) + (np.sin(
                             2 * theta1)) / (4 * sigma1y
                             ** 2)
c1 = (np.sin(theta1) ** 2) / (2 * sigma1x ** 2) + (np.cos(
                             theta1) ** 2) / (2 * sigma1y
                             ** 2)

return (amp0 * np.exp(- (a0 * ((x - x0) ** 2) + 2 * b0 * (
                             x - x0) * (y - y0) + c0 * ((y
                              - y0) ** 2))) + (
amp1 * np.exp(- (a1 * ((x - x1) ** 2) + 2 * b1 * (x - x1)
                             * (y - y1) + c1 * ((y - y1)
                             ** 2)))))


def DeTex_artifact_purge(data):  # Uebersaettigten
                             Substrat-Peak-Scan bereinigen

datapoints = np.swapaxes(data, 0, 1)
max_layer = max(datapoints, key=lambda item: item[2])

data_purged_swap = [[0, 0, 0]]
for datapoints in datapoints:
if max_layer[0] == datapoints[0] and (datapoints[1] <
                             max_layer[1] - 0.1 or
                             datapoints[1] > max_layer[1]
                             + 0.1):
data_purged_swap = np.append(data_purged_swap, [[
                             datapoints[0], datapoints[1],
                              0.1]], axis=0)
else:
```

```
data_purged_swap = np.append(data_purged_swap, [datapoints
                              ], axis=0)
data_purged_swap = np.delete(data_purged_swap, 0, 0)
data_purged = np.swapaxes(data_purged_swap, 0, 1)

return data_purged


def RSM_data_fitter(data, save_name, theta_start):  # Kern
                              -Auswertefunktion

# Daten entpacken, sortieren und Matrix-Dimension fuer
                              weitere Verarbeitung anpassen
datapoints = np.swapaxes(data, 0, 1)
datapoints_sort = datapoints[np.lexsort((datapoints[:, 1],
                               datapoints[:, 0]))]
data_sort = np.swapaxes(datapoints_sort, 0, 1)
xs = data_sort[0]
ys = data_sort[1]
zs = data_sort[2]
zs[zs < 0] = 1.0e-10  # Unphysikalische, negative
                              Randwerte entfernen

np.savetxt(save_name + '.txt', np.c_[xs, ys, zs])

maximum = np.max(zs)

xmin = np.min(xs)
xmax = np.max(xs)

ymin = np.min(ys)
ymax = np.max(ys)

# Start Parameter mit Maxfind
max_layer = max(datapoints, key=lambda item: item[2])
datapoints2 = [[0, 0, 0]]
for datapoints in datapoints:  # Daten um Substratpeak auf
                               0.1 setzen

if max_layer[0] - 0.5 * (xmax - xmin) < datapoints[0] <
                              max_layer[0] + 0.5 * (xmax -
                              xmin) and max_layer[
1] - 0.1 * (ymax - ymin) < datapoints[1] < max_layer[1] +
                              0.5 * (ymax - ymin):
```

```
datapoints2 = np.append(datapoints2, [[datapoints[0],
                              datapoints[1], 0.1]], axis=0)
else:
datapoints2 = np.append(datapoints2, [datapoints], axis=0)

max_buffer = max(datapoints2, key=lambda item: item[2])  #
                               Max in neuer Liste sollte
                              Buffer Layer sein

print(max_layer)
print(max_buffer)

# Startwerte Peakbreite entsprechend Erfahrungswerten
                              setzen
sigma_x = (0.0002, 0.002)
sigma_y = (0.0002, 0.002)

# Startparameter aus Maxfind und Erfahrungswerten
params = Parameters()
params['Amp_sub'] = Parameter(name='Amp_sub', value=
                              max_layer[2], min=10000, max=
                              1e8)
params['px_sub'] = Parameter(name='px_sub', value=
                              max_layer[0], min=xmin, max=
                              xmax)
params['py_sub'] = Parameter(name='py_sub', value=
                              max_layer[1], min=ymin, max=
                              ymax)
params['sigma_x_sub'] = Parameter(name='sigma_x_sub',
                              value=sigma_x[0], min=0)
params['sigma_y_sub'] = Parameter(name='sigma_y_sub',
                              value=sigma_y[0], min=0)
params['theta_sub'] = Parameter(name='theta_sub', value=0,
                               min=-np.pi / 2, max=np.pi /
                              2)
params['Amp_buf'] = Parameter(name='Amp_buf', value=
                              max_buffer[2], min=10, max=
                              1e6)
params['px_buf'] = Parameter(name='px_buf', value=
                              max_buffer[0], min=xmin, max=
                              xmax)
params['py_buf'] = Parameter(name='py_buf', value=
                              max_buffer[1], min=ymin, max=
                              ymax)
```

```
params['sigma_x_buf'] = Parameter(name='sigma_x_buf',
                            value=sigma_x[1], min=0)
params['sigma_y_buf'] = Parameter(name='sigma_y_buf',
                            value=sigma_y[1], min=0)
params['theta_buf'] = Parameter(name='theta_buf', value=
                            theta_start, min=-np.pi / 2,
                            max=np.pi / 2)

# der entscheidende Fit-Schritt
fitter = Minimizer(twoD_Gaussian_model_lm, params,
                            fcn_args=(xs, ys, zs))
result = fitter.minimize(method='leastsq')

# Fitwerte auslesen und ausgeben
Amp_sub = result.params['Amp_sub'].value
px_sub = result.params['px_sub'].value
py_sub = result.params['py_sub'].value
sigma_x_sub = result.params['sigma_x_sub'].value
sigma_y_sub = result.params['sigma_y_sub'].value
theta_sub = result.params['theta_sub'].value
Amp_buf = result.params['Amp_buf'].value
px_buf = result.params['px_buf'].value
py_buf = result.params['py_buf'].value
sigma_x_buf = result.params['sigma_x_buf'].value
sigma_y_buf = result.params['sigma_y_buf'].value
theta_buf = result.params['theta_buf'].value

return (
Amp_sub, px_sub, py_sub, sigma_x_sub, sigma_y_sub,
                            theta_sub, Amp_buf, px_buf,
                            py_buf, sigma_x_buf,
                            sigma_y_buf,
theta_buf, xmin, xmax, ymin, ymax)

def data_converter(filename_a, data_full):  # 1D/DeTex-
                            Daten einlesen und in qx/qz
                            konvertieren
header_read_004 = open(filename_a)
head_004 = header_read_004.readlines()[:14]
gonio_origin_004 = head_004[8].split()
omega_origin_004 = float(gonio_origin_004[4])

# xs_a, ys_a, zs_a = np.loadtxt(filename_a, unpack=True)
# data_a = np.array([xs_a, ys_a, zs_a])
```

```
data_a = DeTex_artifact_purge(data_full)

data_a_conv = [1 / 1.540593 * (np.cos(np.pi / 180.0 * (
                              data_a[1] - (omega_origin_004
                               + data_a[0]))) - np.cos(
np.pi / 180.0 * (omega_origin_004 + data_a[0]))), 1 / 1.
                              540593 * (
np.sin(np.pi / 180.0 * (data_a[1] - (omega_origin_004 +
                              data_a[0]))) + np.sin(
np.pi / 180.0 * (omega_origin_004 + data_a[0]))), data_a[2
                              ]]
return (data_a_conv)

def fit_parameter_printer(fitted_parameters,
                              reziprocal_point):  # Print-
                              Ausgabe zum vergleichen
                              managen
print("fitted parameters", reziprocal_point)
print("Amp_sub", reziprocal_point, fitted_parameters[0])
print("px_sub", reziprocal_point, fitted_parameters[1])
print("py_sub", reziprocal_point, fitted_parameters[2])
# print("sigma_x_sub_004:", sigma_x_sub_004)
# print("sigma_y_sub_004:", sigma_y_sub_004)
print("Amp_buf", reziprocal_point, fitted_parameters[6])
print("px_buf", reziprocal_point, fitted_parameters[7])
print("py_buf", reziprocal_point, fitted_parameters[8])


# print("sigma_x_buf_004:", sigma_x_buf_004)
# print("sigma_y_buf_004:", sigma_y_buf_004)

def data_stitcher(data_sub,data_buf):   # bei viel In-
                              Gehalt die Maps
                              zusammensetzen
xs_a, ys_a, zs_a = np.loadtxt(data_sub, unpack=True)
xs_b, ys_b, zs_b = np.loadtxt(data_buf, unpack=True)
data_full = np.array([xs_a, ys_a, zs_a])
# np.savetxt("224map_data_half.txt", data_b)
data_full = np.append(data_full, [xs_b, ys_b, zs_b], axis=
                              1)
# np.savetxt("224map_data.txt", data_b)
return(data_full)

############## 0 Degree maps
```

```
# Filename aus Kommandozeile
filename_004_0deg_sub = sys.argv[2]
filename_004_0deg_buf = sys.argv[1]

data_004_0deg_stitched = data_stitcher(
                             filename_004_0deg_sub,
                             filename_004_0deg_buf)

data_004_0deg_conv = data_converter(filename_004_0deg_sub,
                              data_004_0deg_stitched)

filename_224_0deg_sub = sys.argv[6]
filename_224_0deg_buf = sys.argv[5]

data_224_0deg_stitched = data_stitcher(
                             filename_224_0deg_sub,
                             filename_224_0deg_buf)

data_224_0deg_conv = data_converter(filename_224_0deg_sub,
                              data_224_0deg_stitched)

origin_data_004_0deg = 'origin_data_004_0deg'
origin_data_224_0deg = 'origin_data_224_0deg'

# Kern-Auswertefunktion aufrufen und Fitparameter auslesen
fitted_parameters_004_0deg = RSM_data_fitter(
                             data_004_0deg_conv,
                             origin_data_004_0deg,
0.0)  # , xmin, xmax, ymin, ymax [12-15]
fit_parameter_printer(fitted_parameters_004_0deg, "
                             _004_0deg:")

fitted_parameters_224_0deg = RSM_data_fitter(
                             data_224_0deg_conv,
                             origin_data_224_0deg,
-np.pi / 4.0)  # xmin_b, xmax_b, ymin_b, ymax_b  [12-15]
fit_parameter_printer(fitted_parameters_224_0deg, "
                             _224_0deg:")

############ 90 Degree maps

filename_004_90deg_sub = sys.argv[4]
filename_004_90deg_buf = sys.argv[3]
```

```
data_004_90deg_stitched = data_stitcher(
                             filename_004_90deg_sub,
                             filename_004_90deg_buf)

data_004_90deg_conv = data_converter(
                             filename_004_90deg_sub,
                             data_004_90deg_stitched)

filename_224_90deg_sub = sys.argv[8]
filename_224_90deg_buf = sys.argv[7]

data_224_90deg_stitched = data_stitcher(
                             filename_224_90deg_sub,
                             filename_224_90deg_buf)

data_224_90deg_conv = data_converter(
                             filename_224_90deg_sub,
                             data_224_90deg_stitched)

origin_data_004_90deg = 'origin_data_004_90deg'
origin_data_224_90deg = 'origin_data_224_90deg'

fitted_parameters_004_90deg = RSM_data_fitter(
                             data_004_90deg_conv,
                             origin_data_004_90deg,0.0)  #
                              , xmin, xmax, ymin, ymax [12
                             -15]
fit_parameter_printer(fitted_parameters_004_90deg, "
                             _004_90deg:")

fitted_parameters_224_90deg = RSM_data_fitter(
                             data_224_90deg_conv,
                             origin_data_224_90deg,-np.pi
                             / 4.0)  # xmin_b, xmax_b,
                             ymin_b, ymax_b  [12-15]
fit_parameter_printer(fitted_parameters_224_90deg, "
                             _224_90deg:")


# Grid-Plot der Gauss-Funktion um Plausibilitaet des Fits
                             zu checken
def RSM_plotter(fitted_parameters):
x_fit = np.arange(fitted_parameters[12], fitted_parameters
```

```
                                    [13], 0.0001)
y_fit = np.arange(fitted_parameters[14], fitted_parameters
                                    [15], 0.0002)
x_fit, y_fit = np.meshgrid(x_fit, y_fit)
z_fit = twoD_Gaussian_model(x_fit, y_fit,
                                    fitted_parameters)
z_fit[z_fit < 0.1] = 0.1

# np.savetxt("z_fit", np.c_[z_fit])

CS = plt.contourf(x_fit, y_fit, z_fit, 50, cmap=plt.cm.
                                    rainbow, aspect='auto',
norm=colors.LogNorm(vmin=0.1, vmax=fitted_parameters[0]))
# plt.colorbar()
return CS


fig = plt.figure()
fig.add_subplot(221, aspect="auto")
CS_004_0deg = RSM_plotter(fitted_parameters_004_0deg)

fig.add_subplot(222, aspect="auto")
CS_224_0deg = RSM_plotter(fitted_parameters_224_0deg)

# plt.colorbar()
fig.add_subplot(223, aspect="auto")
CS_004_90deg = RSM_plotter(fitted_parameters_004_90deg)

fig.add_subplot(224, aspect="auto")
CS_224_90deg = RSM_plotter(fitted_parameters_224_90deg)

plt.show()


def alpha_correction(fitted_parameters_004,
                                    fitted_parameters_224,
                                    direction):
# Fit-Ergebnisse uebergeben
q_s_par_004 = fitted_parameters_004[1]

q_s_ver_004 = fitted_parameters_004[2]

q_l_par_004 = fitted_parameters_004[7]
```

```
q_l_ver_004 = fitted_parameters_004[8]

q_s_par_224 = fitted_parameters_224[1]

q_s_ver_224 = fitted_parameters_224[2]

q_l_par_224 = fitted_parameters_224[7]

q_l_ver_224 = fitted_parameters_224[8]

# Maps auf Substrat-Referenz eichen
q_l_par_004 = q_l_par_004 - q_s_par_004
q_l_ver_004 = q_l_ver_004 + (4 / aGaAs - q_s_ver_004)
q_s_par_004 = 0.0
q_s_ver_004 = 4 / aGaAs

q_l_par_224 = q_l_par_224 + (2 * np.sqrt(2) / aGaAs -
                             q_s_par_224)
q_l_ver_224 = q_l_ver_224 + (4 / aGaAs - q_s_ver_224)
q_s_par_224 = 2 * np.sqrt(2) / aGaAs
q_s_ver_224 = 4 / aGaAs

# Tilt-Winkel bestimmen
alpha = np.arctan(np.abs(q_s_par_004 - q_l_par_004) / (4 /
                              aGaAs - np.abs(q_s_ver_004 -
                              q_l_ver_004)))

if q_l_par_004 < 0:
alpha = - alpha
# else:

print('alpha*10^2', direction, alpha * 180 / np.pi * 100)

# Rotating asymmetric reflex (224) by alpha around (000)

# Rotation matrix

Mrot = np.array([[np.cos(alpha), -np.sin(alpha)], [np.sin(
                             alpha), np.cos(alpha)]])

# print(Mrot)

# Vector: (000) -> uncorrected layer peak in RSM(004)
```

```
q_004_uncorr = np.array([0 / aGaAs, 4 / aGaAs]) + np.array
                            ([q_l_par_004 - q_s_par_004,
                            q_l_ver_004 - q_s_ver_004])

# print(q_004_uncorr)

# Vector: (000) -> uncorrected layer peak in RSM(224)
q_224_uncorr = np.array([2 * np.sqrt(2) / aGaAs, 4 / aGaAs
                            ]) + np.array(
[q_l_par_224 - q_s_par_224, q_l_ver_224 - q_s_ver_224])

# print(q_224_uncorr)

# Execution of rotation

q_004_corr = Mrot.dot(q_004_uncorr)

q_224_corr = Mrot.dot(q_224_uncorr)

# print(direction, q_004_corr)
# Lattice mismatch in (001) direction, see Chauveau et al.

mismatch_vertical = -0.5 * ((q_004_corr[1] - q_s_ver_004)
                            / (4 / aGaAs + q_004_corr[1]
                            - q_s_ver_004) + (
q_224_corr[1] - q_s_ver_224) / (4 / aGaAs + q_224_corr[1]
                            - q_s_ver_224))

# print('mismatch_004:',mismatch_004)

# Lattice mismatch in (hkl) direction, see Chauveau et al.

mismatch_parallel = -(q_224_corr[0] - q_s_par_224) / (2 *
                            np.sqrt(2) / aGaAs +
                            q_224_corr[0] - q_s_par_224)

# print('mismatch_224:', mismatch_224)

return (mismatch_vertical, mismatch_parallel)


# Materialkonstanten
aGaAs = 5.65325
```

```
aInAs = 6.0583

poisson_InAs = 0.35

poisson_GaAs = 0.31

mismatch_004_0deg, mismatch_224_0deg = alpha_correction(
                             fitted_parameters_004_0deg,
                             fitted_parameters_224_0deg, '
                             0deg:')

mismatch_004_90deg, mismatch_224_90deg = alpha_correction(
                             fitted_parameters_004_90deg,
                             fitted_parameters_224_90deg,
'90deg:')

# Complete lattice mismatch assuming phi = 0 and phi = 90
                             have same lattice mismatch

# Poisson ratio initializing

content = 0.25

poisson_InGaAs = content * poisson_InAs + (1 - content) *
                             poisson_GaAs

# print(content, poisson_InGaAs)

iteration = 15

for i in range(iteration):
mismatch = ((1 - poisson_InGaAs) / (1 + poisson_InGaAs)) *
                              0.5 * (mismatch_004_0deg +
                             mismatch_004_90deg) + (
poisson_InGaAs / (1 + poisson_InGaAs)) * (
                             mismatch_224_0deg +
                             mismatch_224_90deg)

content = mismatch * aGaAs / (aInAs - aGaAs)

poisson_InGaAs = content * poisson_InAs + (1 - content) *
                             poisson_GaAs

#     if i == iteration - 1:
```

```
# print(mismatch)
# print(content)
# print(poisson_InGaAs)

# print('mismatch:', mismatch)

print('In content:', 100 * content, '%')
# print('Poisson ratio:', poisson_InGaAs)

# Degree of relaxation

aInGaAs_relaxed = aInAs - (1 - content) * (aInAs - aGaAs)
# print('lattice InGaAs:' , aInGaAs_relaxed)

relaxation_0deg = mismatch_224_0deg * aGaAs / (
                             aInGaAs_relaxed - aGaAs)

print('Relaxation_0deg:', 100 * relaxation_0deg, '%')

relaxation_90deg = mismatch_224_90deg * aGaAs / (
                             aInGaAs_relaxed - aGaAs)

print('Relaxation_90deg:', 100 * relaxation_90deg, '%')
```

# List of Figures


2.1 Construction of the zincblende lattice for GaAs . . . . 27
2.2 Density of states for materials with reduced dimensions 29
2.3 Schematic drawing of the MOVPE machine layout . . 31
2.4 (a) Schematic construction of the contact angle for a partial wetting case. (b) Surface processes during crystal growth via epitaxy. . . . . . . . . . . . . . . . . 35
2.5 Equilibrium phase diagram of depositing a foreign material on a substrate . . . . . . . . . . . . . . . . . . . 37
2.6 Schematic drawing for cubic crystal geometry of depositing a compressively strained heterolayer on a mismatched substrate . . . . . . . . . . . . . . . . . . . . 39
2.7 Misfit dislocation behavior along ⟨110⟩ directions at the interface between a zincblende heteroepitaxial layer and the substrate . . . . . . . . . . . . . . . . . . . . 40
2.8 Content grading designs based on a linear function and resulting misfit dislocation area density . . . . . . . . 44
2.9 Discrete energy states of a QD and respective excitation diagram . . . . . . . . . . . . . . . . . . . . . . . . 49
2.10 Consecutive steps of QD shape manipulation after initial SK growth phase formation . . . . . . . . . . . . . 50
2.11 Schematic drawing of AFM measurement principle . . 53
2.12 Bragg condition underlying XRD measurement and Rigaku XRD device . . . . . . . . . . . . . . . . . . . 55
2.13 Schematic drawing of PL measurement setup . . . . . 57

3.1 Schematic drawing of the jump-convex-inverse InGaAs MMB design . . . . . . . . . . . . . . . . . . . . . . . . 60
3.2 AFM analysis of 50 nm thick InGaAs layers with varying indium content grown at 710 °C . . . . . . . . . . . 63
3.3 Evaluation of the increase in surface roughness of InGaAs using a TMIn flux around 6 µmol/min . . . . . 65
3.4 AFM analysis of the temperature dependence of 100 nm thick InGaAs layers with a TMIn flux of 6.0 µmol/min 67
3.5 AFM analysis of 100 nm thick InGaAs layers with varying indium content grown at 580 °C . . . . . . . . 69
3.6 Temperature-dependent roughness of 100 nm thick InGaAs layers with a TMIn flux of 8.4 µmol/min . . . . 71
3.7 Strain relaxation and surface roughness depending on thickness of $In_{0.264}GaAs$ layers . . . . . . . . . . . . . 72
3.8 AFM surface scans of $In_{0.264}GaAs$ layers with varying thickness grown at 595 °C . . . . . . . . . . . . . . . . 73
3.9 Surface roughness of 400 nm thick $In_{0.262}GaAs$ layer with final jump layer TMGa/TMIn fluxes and varied V/III ratio via $AsH_3$ flux. . . . . . . . . . . . . . . . . 75
3.10 Indium content function of a 125 nm thick graded InGaAs layer transitioning from 26.2 % to 39.2 % . . . 77
3.11 Comparison between AFM scans of various $In_xGa_{1-x}As$ grading profiles to reach 13.2 µmol/min TMIn flux . . 78
3.12 Optimization of the inverse step indium content for QD emission at 1550 nm . . . . . . . . . . . . . . . . . . 82
3.13 Influence of QD deposition temperature on FSS. Histogram for $T_{QD}$ . . . . . . . . . . . . . . . . . . . . . . . 88
3.14 µ-PL spectra of samples with different QD ripening times 89
3.15 70 µm x 70 µm µ-PL map of emission inside the telecom C-band . . . . . . . . . . . . . . . . . . . . . . . . . . 90
3.16 AFM scans of the finalized QD/MMB structure at different growth stages . . . . . . . . . . . . . . . . . . 93
3.17 RSMs around the (400) (left) and (422) (right) reflex of an exemplary QD/MMB/DBR sample . . . . . . . 94

3.18 STEM with high-angle annular dark-field imaging of a capped QD/MMB/DBR sample . . . . . . . . . . . . . 97
3.19 STEM in bright-field contrast of a capped QD/MMB/DBR sample . . . . . . . . . . . . . . . . . . . . . . . . . 98
3.20 AFM scans of jump-convex-inverse MMB grown on a (un-)tilted substrate . . . . . . . . . . . . . . . . . . . . 105
3.21 Roughness of jump-convex-inverse MMB structure for which the total thickness is varied by changing the inverse plus capping region thickness. . . . . . . . . . . 106
3.22 Ensemble-PL spectra of QD/MMB samples with varying inverse layer thickness. . . . . . . . . . . . . . . . . . 107
3.23 AFM analysis of QD hole capping . . . . . . . . . . 109
3.24 AFM scans of 200 nm thick $In_{0.287}GaAs$ layers . . . . 110
3.25 Impact of annealing on surface roughness of jci-MMB 111
3.26 Temperature stability of QD growth . . . . . . . . . . 113

4.1 Schematic drawing of the two-step growth process for QD/MMB/DBR structures . . . . . . . . . . . . . . . 116
4.2 Second-order auto-correlation measurement of exemplary QD transition lines . . . . . . . . . . . . . . . . . 118
4.3 Measurement of the linewidth for a QD/MMB/DBR structure via determination of the first-order coherence function . . . . . . . . . . . . . . . . . . . . . . . . . 119
4.4 Measurement of the FSS for QDs on MMB/DBR structure under cw, non-resonant excitation in saturation . 121
4.5 Decay time measurements for QD/MMB/DBR structure 122
4.6 Reflectivity measurements of a 5-pair InGaAs/InAlAs DBR grown on top of jci-MMB . . . . . . . . . . . . . 124
4.7 Gaußian-shaped cavity schematic and SEM . . . . . . 126
4.8 AFM scans of Gaußian-shaped lens overgrowth . . . . 127
4.9 Circular Bragg grating cavity based on jci-MMB . . . 130
4.10 MOVPE deposition of the base structure for grating outcouplers . . . . . . . . . . . . . . . . . . . . . . . . 132
4.11 Design and investigation of PIN structure . . . . . . . 138

6.1 XRR scan data with simulated fitting curve and residual fit-error of $In_{0.31}GaAs$ . . . 155
6.2 µ-PL spectrum at half-saturation of QD/MMB/DBR sample showing strong background emission . . . 156
6.3 AFM scan analysis of QD sample with 20 nm capping layer . . . 157
6.4 AFM scan analysis of QD sample with 40 nm capping layer . . . 157
6.5 AFM scan-A analysis of QD sample with 60 nm capping layer . . . 157
6.6 AFM scan-B analysis of QD sample with 60 nm capping layer . . . 158
6.7 AFM scan-A analysis of QD sample with 80 nm capping layer . . . 158
6.8 AFM scan-B analysis of QD sample with 80 nm capping layer . . . 158
6.9 AFM scan-C analysis of QD sample with 80 nm capping layer . . . 159
6.10 AFM scan-A analysis of QD sample with 100 nm capping layer . . . 159
6.11 AFM scan-B analysis of QD sample with 100 nm capping layer . . . 159
6.12 AFM scan-C analysis of QD sample with 100 nm capping layer . . . 160
6.13 AFM scan-A analysis of QD sample with 120 nm capping layer . . . 160
6.14 AFM scan-B analysis of QD sample with 120 nm capping layer . . . 160
6.15 AFM scan-C analysis of QD sample with 120 nm capping layer . . . 161
6.16 AFM scan-A analysis of QD sample with 150 nm capping layer . . . 161
6.17 AFM scan-B analysis of QD sample with 150 nm capping layer . . . 161

6.18 AFM scan-C analysis of QD sample with 150 nm capping layer . . . 162
6.19 Second-order auto-correlation data of exemplary QD from refilling species . . . 162
6.20 AFM scans of 500 nm thick Carbon doped InGaAs using $CBr_4$ . . . 163
6.21 RSMs around the (400) (left) and (422) (right) reflex of 500 nm zinc doped InGaAs . . . 164
6.22 RSMs around the (400) and (422) reflex of 450 nm zinc doped jci-MMB structure . . . 164
6.23 AFM scans of 500 nm thick Zinc doped InGaAs using DMZn . . . 165
6.24 AFM scans of 500 nm thick Silicon doped InGaAs using $Si_2H_6$ . . . 165

# List of Tables

3.1 Investigation of different growth rates for 100 nm thick InGaAs layers grown at 710 °C. . . . . . . . . . . . . . . 66
3.2 Convex grading layers with varying thicknesses and grading rates . . . . . . . . . . . . . . . . . . . . . . . . 80
3.3 Sample list for the determination of an appropriate annealing procedure . . . . . . . . . . . . . . . . . . . . . 86
3.4 Crystallographic tilt analysis . . . . . . . . . . . . . . . . 95
3.5 Variation of jump layer thickness and indium content for growth stage II samples . . . . . . . . . . . . . . . . 100
3.6 Influence of reactor pressure on surface roughening of 440 nm thick jump-convex-inverse MMB structure. . . 102
3.7 Influence of growth rate on surface roughening of MMB structure with 180 nm thick jump-convex-inverse section and varied capping layer thickness . . . . . . . . . 103

4.1 Samples for the investigation of $CBr_4$ carbon doping in 500 nm thick InGaAs. . . . . . . . . . . . . . . . . . . 134
4.2 Zinc and Silicon doping levels and RMS roughness for various precursors fluxes in 500 nm thick $In_{0.265}GaAs$. 135

# Publications

- *Thin-film InGaAs metamorphic buffer for telecom C-band InAs quantum dots and optical resonators on GaAs platform.*
  R. Sittig, C. Nawrath, S. Kolatschek, S. Bauer, R. Schaber, J. Huang, P. Vijayan, P. Pruy, S. L. Portalupi, M. Jetter, P. Michler, Nanophotonics, **11.6**, 1109-1116 (2022)

- *Bright Purcell Enhanced Single-Photon Source in the Telecom O-Band Based on a Quantum Dot in a Circular Bragg Grating.*
  S. Kolatschek, C. Nawrath, S. Bauer, J. Huang, J. Fischer, R. Sittig, M. Jetter, S. L. Portalupi, P. Michler, Nano Letters, **21(18)**, 7740-7745 (2021)

- *Realization of a tunable fiber-based double cavity system.*
  T. Herzog, S. Böhrkircher, S. Both, S. Fischer, R. Sittig, M. Jetter, S. L. Portalupi, T. Weiss, P. Michler, Phys. Rev. B, **102(23)**, 235306 (2020)

- *High emission rate from a Purcell-enhanced, triggered source of pure single photons in the telecom C-band.*
  C. Nawrath, R. Joos, S. Kolatschek, S. Bauer, P. Pruy, F. Hornung, J. Fischer, J. Huang, P. Vijayan, R. Sittig, M. Jetter, S. L. Portalupi, P. Michler, arXiv preprint, **2207.12898**, (2022)

- *Deterministic Storage and Retrieval of Telecom Quantum Dot Photons Interfaced with an Atomic Quantum Memory.*
  S. E. Thomas, L. Wagner, R. Joos, R. Sittig, C. Nawrath, P. Burdekin, T. Huber-Loyola, S. Sagona-Stophel, S. Höfling, M. Jetter, P. Michler, I. A. Walmsley, S. L. Portalupi, P. M. Ledingham, arXiv preprint, **2303.04166**, (2023)

# Curriculum Vitae

## Personal

| | |
|---|---|
| Full name | Robert Sittig |
| Born | December 1, 1989 in Stuttgart |

## Education (school)

| | |
|---|---|
| 1996/10 | Grundschule Gaisburg, Stuttgart |
| 2000/10 | Lessing-Gymnasium, Winnenden |
| 2009/06 | Degree: Abitur |

## Education (academic)

| | |
|---|---|
| 2010/10 | University of Stuttgart,<br>Bachelor student in Physics |
| 2013/09 | Degree: B.Sc. in Physics |
| 2013/10 | University of Stuttgart,<br>Master student in Physics |
| 2015/12 | Degree: M.Sc. in Physics |
| 2017/09 | Institut für Halbleiteroptik und<br>Funktionelle Grenzflächen,<br>Ph.D. candidate |

# Bibliography

[1] Otto Jespersen. *Language: Its nature, development, and origin*. Routledge, 2013.

[2] Stephen C Levinson and Judith Holler. The origin of human multi-modal communication. *Philosophical Transactions of the Royal Society B: Biological Sciences*, 369(1651):20130302, 2014.

[3] John Crawfurd. On the origin and history of written language. *Transactions of the Ethnological Society of London*, 5:96–104, 1867.

[4] Wayne M Senner. *The origins of writing*. U of Nebraska Press, 1991.

[5] Harold Innis. Media in ancient empires. In *Communication in History*, pages 15–23. Routledge, 2018.

[6] Robert K Logan. *The alphabet effect*. New York: Morrow, 1986.

[7] Shelton A Gunaratne. Paper, printing and the printing press: A horizontally integrative macrohistory analysis. *Gazette (Leiden, Netherlands)*, 63(6):459–479, 2001.

[8] Fran Rees. *Johannes Gutenberg: Inventor of the printing press*. Capstone, 2006.

[9] Andrew Erskine. Culture and power in ptolemaic Egypt: The Museum and Library of Alexandria. *Greece & Rome*, 42(1):38–48, 1995.

[10] Daniel Heller-Roazen. Tradition's destruction: On the library of Alexandria. *October*, 100:133–153, 2002.

[11] Elizabeth L Eisenstein. The printing press as an agent of change. *Cambridge: Cambridge*, 1985.

[12] Chul-Young Lee and Jae-Woong Yoon. A Study on the Facility Layout and Signal-fire Stand of Border Signal-fire in Chosun Dynasty. *Journal of Architectural History*, 15(5):41–56, 2006.

[13] Lasafam Iturrizaga. Historical telecommunication in the Hindukush-Karakoram-Himalayas: An ancient early warning system for glacier lake outbursts. In *EGU General Assembly Conference Abstracts*, pages EPSC2016–7902, 2016.

[14] SJ Brookes and J Baker. Signalling intent: beacons, lookouts and military communications. Liverpool University Press, 2015.

[15] William Bernhard Tegetmeier. *The Homing Or Carrier Pigeon...* George Routledge, 1871.

[16] Alberto E Minetti. Efficiency of equine express postal systems. *Nature*, 426(6968):785–786, 2003.

[17] Yrjö Kaukiainen. Shrinking the world: Improvements in the speed of information transmission, c. 1820–1870. *European Review of Economic History*, 5(1):1–28, 2001.

[18] Lewis Coe. *The telegraph: A history of Morse's invention and its predecessors in the United States.* McFarland, 2003.

[19] Kenneth G Bartlett. Social impact of the radio. *The Annals of the American Academy of Political and Social Science*, 250(1):89–97, 1947.

[20] William H Dutton. The social impact of emerging telephone services. *Telecommunications Policy*, 16(5):377–387, 1992.

[21] Stuart J Kaplan. The impact of cable television services on the use of competing media. *Journal of Broadcasting & Electronic Media*, 22(2):155–165, 1978.

[22] Manuel Castells. The impact of the internet on society: a global perspective. *Change*, 19:127–148, 2014.

[23] Robert Waterman McChesney. *Communication revolution: Critical junctures and the future of media*. New Press, 2007.

[24] Everett M Rogers et al. *Communication technology*. Simon and Schuster, 1986.

[25] Thomas Jakobsen. A fast method for cryptanalysis of substitution ciphers. *Cryptologia*, 19(3):265–274, 1995.

[26] Chris Christensen. Cryptography of the Vigenère Cipher. *proceedings of Computer Sciences Corporation*, pages 1–18, 2006.

[27] Rajdeep Bhanot and Rahul Hans. A review and comparative analysis of various encryption algorithms. *International Journal of Security and Its Applications*, 9(4):289–306, 2015.

[28] Alan Gordon Smith. *The Babington Plot*. Macmillan, 1936.

[29] Nigel P Smart. The enigma machine. In *Cryptography Made Simple*, pages 133–161. Springer, 2016.

[30] Stephen Wiesner. Conjugate coding. *ACM Sigact News*, 15(1):78–88, 1983.

[31] Charles Bennet. Quantum cryptography: Public key distribution and coin tossing. In *Proc. of IEEE Int. Conf. on Comp. Sys. and Signal Proc., Dec. 1984*, 1984.

[32] William K Wootters and Wojciech H Zurek. A single quantum cannot be cloned. *Nature*, 299(5886):802–803, 1982.

[33] DGBJ Dieks. Communication by EPR devices. *Physics Letters A*, 92(6):271–272, 1982.

[34] Charles H Bennett, Gilles Brassard, and N David Mermin. Quantum cryptography without Bell's theorem. *Physical Review Letters*, 68(5):557, 1992.

[35] Hoi-Kwong Lo, Marcos Curty, and Kiyoshi Tamaki. Secure quantum key distribution. *Nature Photonics*, 8(8):595–604, 2014.

[36] Charles H Bennett, Gilles Brassard, Claude Crépeau, and Marie-Hélene Skubiszewska. Practical quantum oblivious transfer. In *Annual international cryptology conference*, pages 351–366. Springer, 1991.

[37] Anne Broadbent and Christian Schaffner. Quantum cryptography beyond quantum key distribution. *Designs, Codes and Cryptography*, 78(1):351–382, 2016.

[38] Artur K Ekert. Quantum Cryptography and Bell's Theorem. In *Quantum Measurements in Optics*, pages 413–418. Springer, 1992.

[39] Benoit Darquié, Matthew PA Jones, Jos Dingjan, Jerome Beugnon, Silvia Bergamini, Yvan Sortais, Gaetan Messin, Antoine Browaeys, and Philippe Grangier. Controlled single-photon emission from a single trapped two-level atom. *Science*, 309(5733):454–456, 2005.

[40] Xiao-Liu Chu, Stephan Götzinger, and Vahid Sandoghdar. A single molecule as a high-fidelity photon gun for producing intensity-squeezed light. *Nature Photonics*, 11(1):58–62, 2017.

[41] Xin Wang, Adam Miranowicz, Hong-Rong Li, and Franco Nori. Multiple-output microwave single-photon source using superconducting circuits with longitudinal and transverse couplings. *Physical Review A*, 94(5):053858, 2016.

[42] Zubin Jacob, Igor Smolyaninov, and Evgenii E Narimanov. Single photon gun: Radiative decay engineering with metamaterials.

In *Frontiers in Optics*, page PDPB6. Optical Society of America, 2009.

[43] Alexander Lohrmann, BC Johnson, JC McCallum, and Stefania Castelletto. A review on single photon sources in silicon carbide. *Reports on Progress in Physics*, 80(3):034502, 2017.

[44] Sébastien Pezzagna, Detlef Rogalla, Dominik Wildanger, Jan Meijer, and Alexander Zaitsev. Creation and nature of optical centres in diamond for single-photon emission—overview and critical remarks. *New Journal of Physics*, 13(3):035024, 2011.

[45] Pascale Senellart, Glenn Solomon, and Andrew White. High-performance semiconductor quantum-dot single-photon sources. *Nature Nanotechnology*, 12(11):1026–1039, 2017.

[46] Xin Cao, Michael Zopf, and Fei Ding. Telecom wavelength single photon sources. *Journal of Semiconductors*, 40(7):071901, 2019.

[47] H Vural, J Maisch, I Gerhardt, M Jetter, SL Portalupi, and P Michler. Characterization of spectral diffusion by slow-light photon-correlation spectroscopy. *Physical Review B*, 101(16):161401, 2020.

[48] PW Fry, JJ Finley, LR Wilson, A Lemaitre, DJ Mowbray, MS Skolnick, M Hopkinson, G Hill, and JC Clark. Electric-field-dependent carrier capture and escape in self-assembled InAs/GaAs quantum dots. *Applied Physics Letters*, 77(26):4344–4346, 2000.

[49] Peter Michler. *Single semiconductor quantum dots*, volume 28. Springer, 2009.

[50] L Seravalli, M Minelli, P Frigeri, P Allegri, V Avanzini, and S Franchi. The effect of strain on tuning of light emission energy of InAs/InGaAs quantum-dot nanostructures. *Applied Physics Letters*, 82(14):2341–2343, 2003.

[51] Govind P Agrawal. *Fiber-optic communication systems.* John Wiley & Sons, 2012.

[52] A Hospodkova, E Hulicius, J Oswald, J Pangrac, T Mates, K Kuldova, K Melichar, and T Šimeček. Properties of MOVPE InAs/GaAs quantum dots overgrown by InGaAs. *Journal of Crystal Growth*, 298:582–585, 2007.

[53] L Seravalli, C Bocchi, G Trevisi, and P Frigeri. Properties of wetting layer states in low density InAs quantum dot nanostructures emitting at 1.3 μm: Effects of InGaAs capping. *Journal of Applied Physics*, 108(11):114313, 2010.

[54] Matthias Paul, Jan Kettler, Katharina Zeuner, Caterina Clausen, Michael Jetter, and Peter Michler. Metal-organic vapor-phase epitaxy-grown ultra-low density InGaAs/GaAs quantum dots exhibiting cascaded single-photon emission at 1.3 μm. *Applied Physics Letters*, 106(12):122105, 2015.

[55] Toshiyuki Miyazawa, Kazuya Takemoto, Yoshiki Sakuma, Shinichi Hirose, Tatsuya Usuki, Naoki Yokoyama, Motomu Takatsu, and Yasuhiko Arakawa. Single-photon generation in the 1.55 μm optical-fiber band from an InAs/InP quantum dot. *Japanese Journal of Applied Physics*, 44(5L):L620, 2005.

[56] Muhammad Danang Birowosuto, Hisashi Sumikura, Shinji Matsuo, Hideaki Taniyama, Peter J van Veldhoven, Richard Nötzel, and Masaya Notomi. Fast Purcell-enhanced single photon source in 1550 nm telecom band from a resonant quantum dot-cavity coupling. *Scientific Reports*, 2(1):1–5, 2012.

[57] T Müller, J Skiba-Szymanska, AB Krysa, J Huwer, M Felle, Matthew Anderson, RM Stevenson, J Heffernan, David Alastair Ritchie, and AJ Shields. A quantum light-emitting diode for the standard telecom window around 1550nm. *Nature Communications*, 9(1):1–6, 2018.

[58] M Anderson, T Müller, J Skiba-Szymanska, AB Krysa, J Huwer, RM Stevenson, J Heffernan, DA Ritchie, and AJ Shields. Gigahertz-clocked teleportation of time-bin qubits with a quantum dot in the telecommunication C-band. *Physical Review Applied*, 13(5):054052, 2020.

[59] M Anderson, T Müller, J Skiba-Szymanska, AB Krysa, J Huwer, RM Stevenson, J Heffernan, DA Ritchie, and AJ Shields. Coherence in single photon emission from droplet epitaxy and Stranski–Krastanov quantum dots in the telecom C-band. *Applied Physics Letters*, 118(1):014003, 2021.

[60] Cyril Paranthoen, Charly Platz, Gautier Moreau, Nicolas Bertru, Olivier Dehaese, Alain Le Corre, Patrice Miska, Jacky Even, Hervé Folliot, Christophe Labbe, et al. Growth and optical characterizations of InAs quantum dots on InP substrate: towards a 1.55 µm quantum dot laser. *Journal of Crystal Growth*, 251(1-4):230–235, 2003.

[61] Ł Dusanowski, M Syperek, P Mrowiński, W Rudno-Rudziński, J Misiewicz, A Somers, S Höfling, M Kamp, JP Reithmaier, and G Sęk. Single photon emission at 1.55 µm from charged and neutral exciton confined in a single quantum dash. *Applied Physics Letters*, 105(2):021909, 2014.

[62] Joanna Skiba-Szymanska, R Mark Stevenson, Christiana Varnava, Martin Felle, Jan Huwer, Tina Müller, Anthony J Bennett, James P Lee, Ian Farrer, Andrey B Krysa, et al. Universal growth scheme for quantum dots with low fine-structure splitting at various emission wavelengths. *Physical Review Applied*, 8(1):014013, 2017.

[63] Shumin Wang. *Lattice engineering: technology and applications*. CRC Press, 2012.

[64] John E Ayers. Low-temperature and metamorphic buffer layers. *Handbook of Crystal Growth*, pages 1007–1056, 2015.

[65] J Tersoff. Dislocations and strain relief in compositionally graded layers. *Applied Physics Letters*, 62(7):693–695, 1993.

[66] V Krishnamoorthy, YW Lin, and RM Park. Application of “critical compositional difference”concept to the growth of low dislocation density ($< 10^4/\mathrm{cm}^2$) $\mathrm{In}_x\mathrm{Ga}_{1-x}$ As (x $\leq$ 0.5) on GaAs. *Journal of Applied Physics*, 72(5):1752–1757, 1992.

[67] M Haupt, K Köhler, P Ganser, S Emminger, S Müller, and W Rothemund. Growth of high quality $\mathrm{Al}_{0.48}\mathrm{In}_{0.52}\mathrm{As}/\mathrm{Ga}_{0.47}\mathrm{In}_{0.53}$ As heterostructures using strain relaxed $\mathrm{Al}_x\mathrm{Ga}_y\mathrm{In}_{1-x-y}\mathrm{As}$ buffer layers on GaAs. *Applied Physics Letters*, 69(3):412–414, 1996.

[68] Robert H Saul. Effect of a $\mathrm{GaAs}_x\mathrm{P}_{1-x}$ Transition Zone on the Perfection of GaP Crystals Grown by Deposition onto GaAs Substrates. *Journal of Applied Physics*, 40(8):3273–3279, 1969.

[69] Y-C Xin, LG Vaughn, LR Dawson, A Stintz, Y Lin, LF Lester, and DL Huffaker. InAs quantum-dot GaAs-based lasers grown on AlGaAsSb metamorphic buffers. *Journal of Applied Physics*, 94(3):2133–2135, 2003.

[70] Tedi Kujofsa and John E Ayers. Equilibrium lattice relaxation and misfit dislocations in continuously- and step-graded $\mathrm{In}_x\mathrm{Ga}_{1-x}\mathrm{As}$/GaAs (001) and $\mathrm{GaAs}_{1-y}\mathrm{Py}$/GaAs (001) metamorphic buffer layers. *International Journal of High Speed Electronics and Systems*, 24(03n04):1520009, 2015.

[71] Shiro Sakai. New method to relax thermal stress in GaAs grown on Si substrates. *Applied Physics Letters*, 51(14):1069–1071, 1987.

[72] H Horikawa, Y Ogawa, Y Kawai, and M Sakuta. Heteroepitaxial growth of InP on a GaAs substrate by low-pressure metalorganic vapor phase epitaxy. *Applied Physics Letters*, 53(5):397–399, 1988.

[73] Alexander A Chernov. *Modern crystallography III: crystal growth*, volume 36. Springer Science & Business Media, 2012.

[74] D Lee, MS Park, Z Tang, H Luo, R Beresford, and CR Wie. Characterization of metamorphic $In_xAl_{1-x}As/GaAs$ buffer layers using reciprocal space mapping. *Journal of Applied Physics*, 101(6):063523, 2007.

[75] H Choi, Y Jeong, J Cho, and MH Jeon. Effectiveness of nonlinear graded buffers for In(Ga,Al)As metamorphic layers grown on GaAs (001). *Journal of Crystal Growth*, 311(4):1091–1095, 2009.

[76] Tedi Kujofsa and John E Ayers. Lattice relaxation and misfit dislocations in nonlinearly graded $In_xGa_{1-x}As/GaAs$ (001) and $GaAs_{1-y}P_y/GaAs$ (001) metamorphic buffer layers. *Journal of Vacuum Science & Technology B, Nanotechnology and Microelectronics: Materials, Processing, Measurement, and Phenomena*, 32(3):031205, 2014.

[77] S Xhurxhi, F Obst, D Sidoti, B Bertoli, T Kujofsa, S Cheruku, JP Correa, PB Rago, EN Suarez, FC Jain, et al. S-graded buffer layers for lattice-mismatched heteroepitaxial devices. *Journal of Electronic Materials*, 40(12):2348–2354, 2011.

[78] NN Ledentsov, AR Kovsh, AE Zhukov, NA Maleev, SS Mikhrin, AP Vasil'ev, ES Semenova, MV Maximov, Yu M Shernyakov, NV Kryzhanovskaya, et al. High performance quantum dot lasers on GaAs substrates operating in 1.5 μm range. *Electronics Letters*, 39(15):1126–1128, 2003.

[79] NN Ledentsov, VA Shchukin, T Kettler, K Posilovic, D Bimberg, L Ya Karachinsky, A Yu Gladyshev, MV Maximov, II Novikov, Yu M Shernyakov, et al. MBE-grown metamorphic lasers for applications at telecom wavelengths. *Journal of Crystal Growth*, 301:914–922, 2007.

[80] ES Semenova, R Hostein, G Patriarche, O Mauguin, L Largeau, I Robert-Philip, A Beveratos, and A Lemaître. Metamorphic approach to single quantum dot emission at 1.55 μ m on GaAs substrate. *Journal of Applied Physics*, 103(10):103533, 2008.

[81] L Seravalli, G Trevisi, P Frigeri, and C Bocchi. Low Density Metamorphic Quantum Dot structures with emission in the 1.3–1.55 μm window. In *Journal of Physics: Conference Series*, volume 245, page 012074. IOP Publishing, 2010.

[82] Matthias Paul, Fabian Olbrich, Jonatan Höschele, Susanne Schreier, Jan Kettler, Simone Luca Portalupi, Michael Jetter, and Peter Michler. Single-photon emission at 1.55 μm from MOVPE-grown InAs quantum dots on InGaAs/GaAs metamorphic buffers. *Applied Physics Letters*, 111(3):033102, 2017.

[83] CJR Sheppard. Approximate calculation of the reflection coefficient from a stratified medium. *Pure and Applied Optics: Journal of the European Optical Society Part A*, 4(5):665, 1995.

[84] Fabian Olbrich, Jonatan Höschele, Markus Müller, Jan Kettler, Simone Luca Portalupi, Matthias Paul, Michael Jetter, and Peter Michler. Polarization-entangled photons from an InGaAs-based quantum dot emitting in the telecom C-band. *Applied Physics Letters*, 111(13):133106, 2017.

[85] Katharina D Zeuner, Matthias Paul, Thomas Lettner, Carl Reuterskiöld Hedlund, Lucas Schweickert, Stephan Steinhauer, Lily Yang, Julien Zichi, Mattias Hammar, Klaus D Jöns, et al. A stable wavelength-tunable triggered source of single photons and cascaded photon pairs at the telecom C-band. *Applied Physics Letters*, 112(17):173102, 2018.

[86] Katharina D Zeuner, Klaus D Jons, Lucas Schweickert, Carl Reuterskiöld Hedlund, Carlos Nunez Lobato, Thomas Lettner, Kai Wang, Samuel Gyger, Eva Scholl, Stephan Steinhauer, et al. On-demand generation of entangled photon pairs in the telecom

C-band with InAs quantum dots. *ACS Photonics*, 8(8):2337–2344, 2021.

[87] C Nawrath, F Olbrich, M Paul, SL Portalupi, M Jetter, and P Michler. Coherence and indistinguishability of highly pure single photons from non-resonantly and resonantly excited telecom C-band quantum dots. *Applied Physics Letters*, 115(2):023103, 2019.

[88] C Nawrath, H Vural, J Fischer, R Schaber, SL Portalupi, M Jetter, and P Michler. Resonance fluorescence of single In (Ga) As quantum dots emitting in the telecom C-band. *Applied Physics Letters*, 118(24):244002, 2021.

[89] Simone Luca Portalupi, Michael Jetter, and Peter Michler. InAs quantum dots grown on metamorphic buffers as non-classical light sources at telecom C-band: A review. *Semiconductor Science and Technology*, 34(5):053001, 2019.

[90] John C Slater and George F Koster. Simplified LCAO method for the periodic potential problem. *Physical Review*, 94(6):1498, 1954.

[91] LP Howland. Band structure and cohesive energy of potassium chloride. *Physical Review*, 109(6):1927, 1958.

[92] AH Wilson. The Theory of Metals (Cambridge Univ), 1953.

[93] Arnold Sommerfeld. Zur Elektronentheorie der Metalle auf Grund der fermischen Statistik. *Zeitschrift für Physik*, 47(1-2):1–32, 1928.

[94] Po Dong, Young-Kai Chen, Guang-Hua Duan, and David T Neilson. Silicon photonic devices and integrated circuits. *Nanophotonics*, 3(4-5):215–228, 2014.

[95] SP DenBaars, BY Maa, PD Dapkus, AD Danner, and H Co Lee. Homogeneous and heterogeneous thermal decomposition rates of

trimethylgallium and arsine and their relevance to the growth of GaAs by MOCVD. *Journal of Crystal Growth*, 77(1-3):188–193, 1986.

[96] SA Blokhin, AV Sakharov, NA Maleev, MM Kulagina, Yu M Shernyakov, II Novikov, N Yu Gordeev, MV Maximov, AG Kuzmenkov, VM Ustinov, et al. The impact of thermal effects on the performance of vertical-cavity surface-emitting lasers based on sub-monolayer InGaAs quantum dots. *Semiconductor Science and Technology*, 22(3):203, 2007.

[97] Fumio Koyama. Recent advances of VCSEL photonics. *Journal of Lightwave Technology*, 24(12):4502–4513, 2006.

[98] K Haberland, A Kaluza, M Zorn, M Pristovsek, H Hardtdegen, M Weyers, J-T Zettler, and W Richter. Real-time calibration of wafer temperature, growth rate and composition by optical in-situ techniques during $Al_xGa_{1-x}As$ growth in MOVPE. *Journal of Crystal Growth*, 240(1-2):87–97, 2002.

[99] NK Adam. Use of the term 'Young's Equation' for contact angles. *Nature*, 180(4590):809–810, 1957.

[100] MJ Stowell and TE Hutchinson. Nucleation kinetics in thin film growth: II. Analytical evaluation of nucleation and growth behaviour. *Thin Solid Films*, 8(1):41–53, 1971.

[101] Marcia H Grabow and George H Gilmer. Thin film growth modes, wetting and cluster nucleation. *Surface Science*, 194(3):333–346, 1988.

[102] C Ratsch and JA Venables. Nucleation theory and the early stages of thin film growth. *Journal of Vacuum Science & Technology A: Vacuum, Surfaces, and Films*, 21(5):S96–S109, 2003.

[103] István Daruka and Albert-László Barabási. Dislocation-free island formation in heteroepitaxial growth: a study at equilibrium. *Physical Review Letters*, 79(19):3708, 1997.

[104] Alexander A Chernov. Nucleation and epitaxy. In *Modern Crystallography III*, pages 48–103. Springer, 1984.

[105] W. Ostwald. Surface diffusion and island density. In *Z. Phys. Chem.*, pages 34, 495. 1900.

[106] George Neville Greaves, A Lindsay Greer, Roderic S Lakes, and Tanguy Rouxel. Poisson's ratio and modern materials. *Nature Materials*, 10(11):823–837, 2011.

[107] Liang Dong, Jurgen Schnitker, Richard W Smith, and David J Srolovitz. Stress relaxation and misfit dislocation nucleation in the growth of misfitting films: A molecular dynamics simulation study. *Journal of Applied Physics*, 83(1):217–227, 1998.

[108] Tedi Kujofsa and JE Ayers. Dynamics of Kinetically Limited Strain and Threading Dislocations in Temperature-and Compositionally Graded ZnSSe/GaAs (001) Metamorphic Heterostructures. *Journal of Electronic Materials*, 45(9):4580–4586, 2016.

[109] GJ Whaley and PI Cohen. Relaxation of strained InGaAs during molecular beam epitaxy. *Applied Physics Letters*, 57(2):144–146, 1990.

[110] R Beresford, J Yin, K Tetz, and E Chason. Real-time measurements of stress relaxation in InGaAs/GaAs. *Journal of Vacuum Science & Technology B: Microelectronics and Nanometer Structures Processing, Measurement, and Phenomena*, 18(3):1431–1434, 2000.

[111] R Beanland. Multiplication of misfit dislocations in epitaxial layers. *Journal of Applied Physics*, 72(9):4031–4035, 1992.

[112] B Pérez Rodriguez and J Mirecki Millunchick. The role of morphology in the relaxation of strain in InGaAs/GaAs. *Journal of Crystal Growth*, 264(1-3):64–69, 2004.

[113] Srikanth B Samavedam and EA Fitzgerald. Novel dislocation structure and surface morphology effects in relaxed Ge/Si-Ge (graded)/Si structures. *Journal of Applied Physics*, 81(7):3108–3116, 1997.

[114] AM Andrews, JS Speck, AE Romanov, M Bobeth, and W Pompe. Modeling cross-hatch surface morphology in growing mismatched layers. *Journal of Applied Physics*, 91(4):1933–1943, 2002.

[115] AM Andrews, R LeSar, MA Kerner, JS Speck, AE Romanov, AL Kolesnikova, M Bobeth, and W Pompe. Modeling crosshatch surface morphology in growing mismatched layers. Part II: Periodic boundary conditions and dislocation groups. *Journal of Applied Physics*, 95(11):6032–6047, 2004.

[116] GR Booker, JM Titchmarsh, J Fletcher, DB Darby, M Hockly, and M Al-Jassim. Nature, origin and effect of dislocations in epitaxial semiconductor layers. *Journal of Crystal Growth*, 45:407–425, 1978.

[117] VI Vdovin. Misfit dislocations in epitaxial heterostructures: Mechanisms of generation and multiplication. *Physica Status Solidi (a)*, 171(1):239–250, 1999.

[118] LE Levine and Robb Thomson. X-ray scattering by dislocations in crystals. General theory and application to screw dislocations. *Acta Crystallographica Section A: Foundations of Crystallography*, 53(5):590–602, 1997.

[119] O Yastrubchak, T Wosiński, JZ Domagała, E Łusakowska, T Figielski, B Pecz, and AL Toth. Misfit strain anisotropy in partially relaxed lattice-mismatched InGaAs/GaAs heterostructures. *Journal of Physics: Condensed Matter*, 16(2):S1, 2003.

[120] Ichiro Yonenaga and K Sumino. Behaviour of dislocations in GaAs revealed by etch pit technique and X-ray topography. *Journal of Crystal Growth*, 126(1):19–29, 1993.

[121] JW Matthews and AE Blakeslee. Defects in epitaxial multilayers: I. Misfit dislocations. *Journal of Crystal Growth*, 27:118–125, 1974.

[122] R People and JC Bean. Calculation of critical layer thickness versus lattice mismatch for $Ge_xSi_{1-x}$/Si strained-layer heterostructures. *Applied Physics Letters*, 47(3):322–324, 1985.

[123] JC Bean, Leonard C Feldman, AT Fiory, S t Nakahara, and IK Robinson. $Ge_xSi_{1-x}$/Si strained-layer superlattice grown by molecular beam epitaxy. *Journal of Vacuum Science & Technology A: Vacuum, Surfaces, and Films*, 2(2):436–440, 1984.

[124] DC Houghton, CJ Gibbings, CG Tuppen, MH Lyons, and MAG Halliwell. Equilibrium critical thickness for $Si_{1-x}Ge_x$ strained layers on (100) Si. *Applied Physics Letters*, 56(5):460–462, 1990.

[125] B Elman, Emil S Koteles, P Melman, C Jagannath, Johnson Lee, and D Dugger. In situ measurements of critical layer thickness and optical studies of InGaAs quantum wells grown on GaAs substrates. *Applied Physics Letters*, 55(16):1659–1661, 1989.

[126] PJ Orders and BF Usher. Determination of critical layer thickness in $In_xGa_{1-x}As$/GaAs heterostructures by x-ray diffraction. *Applied Physics Letters*, 50(15):980–982, 1987.

[127] RH Dixon and PJ Goodhew. On the origin of misfit dislocations in InGaAs/GaAs strained layers. *Journal of Applied Physics*, 68(7):3163–3168, 1990.

[128] Wei Wang, Qian Zhou, Yuan Dong, Eng Soon Tok, and Yee-Chia Yeo. Critical thickness for strain relaxation of $Ge_{1-x}Sn_x$ ($x \leq 0.17$) grown by molecular beam epitaxy on Ge (001). *Applied Physics Letters*, 106(23):232106, 2015.

[129] DJ Dunstan. Mathematical model for strain relaxation in multilayer metamorphic epitaxial structures. *Philosophical Magazine A*, 73(5):1323–1332, 1996.

[130] R Beanland, DJ Dunstan, and PJ Goodhew. Plastic relaxation and relaxed buffer layers for semiconductor epitaxy. *Advances in Physics*, 45(2):87–146, 1996.

[131] DJ Dunstan, P Kidd, R Beanland, A Sacedón, E Calleja, L González, Y González, and FJ Pacheco. Predictability of plastic relaxation in metamorphicepitaxy. *Materials Science and Technology*, 12(2):181–186, 1996.

[132] PMJ Marée, JC Barbour, JF Van der Veen, KL Kavanagh, CWT Bulle-Lieuwma, and MPA Viegers. Generation of misfit dislocations in semiconductors. *Journal of Applied Physics*, 62(11):4413–4420, 1987.

[133] AV Drigo, A Aydinli, A Carnera, F Genova, C Rigo, C Ferrari, P Franzosi, and G Salviati. On the mechanisms of strain release in molecular-beam-epitaxy-grown $In_xGa_{1-x}As$/GaAs single heterostructures. *Journal of Applied Physics*, 66(5):1975–1983, 1989.

[134] V Bellani, C Bocchi, T Ciabattoni, S Franchi, P Frigeri, P Galinetto, M Geddo, F Germini, G Guizzetti, L Nasi, et al. Residual strain measurements in InGaAs metamorphic buffer layers on GaAs. *The European Physical Journal B*, 56(3):217–222, 2007.

[135] Tedi Kujofsa and John E Ayers. Electric circuit model for strained-layer epitaxy. *Semiconductor Science and Technology*, 31(11):115014, 2016.

[136] SV Sorokin, GV Klimko, IV Sedova, AA Sitnikova, DA Kirilenko, MV Baidakova, MA Yagovkina, TA Komissarova, KG Belyaev, and SV Ivanov. Peculiarities of strain relaxation in linearly graded InxGa1- xAs/GaAs (001) metamorphic buffer layers grown by molecular beam epitaxy. *Journal of Crystal Growth*, 455:83–89, 2016.

[137] MS Abrahams, LR Weisberg, CJ Buiocchi, and J Blanc. Dislocation morphology in graded heterojunctions: $GaAs_{1-x}P_x$. *Journal of Materials Science*, 4(3):223–235, 1969.

[138] B Bertoli, EN Suarez, JE Ayers, and FC Jain. Misfit dislocation density and strain relaxation in graded semiconductor heterostructures with arbitrary composition profiles. *Journal of Applied Physics*, 106(7):073519, 2009.

[139] T Kujofsa, W Yu, S Cheruku, B Outlaw, S Xhurxhi, F Obst, D Sidoti, B Bertoli, PB Rago, EN Suarez, et al. Plastic Flow and Dislocation Compensation in $ZnS_ySe_{1-y}$/GaAs (001) Heterostructures. *Journal of Electronic Materials*, 41(11):2993–3000, 2012.

[140] G Salviati, C Ferrari, L Lazzarini, S Franchi, A Bosacchi, F Taiariol, M Mazzer, C Zanotti-Fregonara, F Romanato, and AV Drigo. TEM and X-ray diffraction studies of III-V lattice mismatched multilayers and superlattices. In *CONFERENCE SERIES-INSTITUTE OF PHYSICS*, volume 146, pages 337–348. IOP PUBLISHING LTD, 1995.

[141] A Sacedon, F González-Sanz, E Calleja, E Munoz, SI Molina, FJ Pacheco, D Araujo, R Garcia, M Lourenco, Z Yang, et al. Design of InGaAs linear graded buffer structures. *Applied Physics Letters*, 66(24):3334–3336, 1995.

[142] EA Fitzgerald, AY Kim, MT Currie, TA Langdo, G Taraschi, and MT Bulsara. Dislocation dynamics in relaxed graded composition semiconductors. *Materials Science and Engineering: B*, 67(1-2):53–61, 1999.

[143] R Hull, JC Bean, and C Buescher. A phenomenological description of strain relaxation in $Ge_xSi_{1-x}$/Si (100) heterostructures. *Journal of Applied Physics*, 66(12):5837–5843, 1989.

[144] DE Grider, SE Swirhun, DH Narum, AI Akinwande, TE Nohava, WR Stuart, P Joslyn, and KC Hsieh. Metamorphic

$In_yGa_{1-y}As/In_zAl_{1-z}$ As heterostructure field effect transistors grown on GaAs (001) substrates using molecular-beam epitaxy. *Journal of Vacuum Science & Technology B: Microelectronics Processing and Phenomena*, 8(2):301–304, 1990.

[145] Tedi Kujofsa and John E Ayers. Equilibrium Lattice Relaxation and Misfit Dislocations in Step-Graded $In_xGa_{1-x}As/GaAs$ (001) and $In_xAl_{1-x}As/GaAs$ (001) Metamorphic Buffer Layers. *Journal of Electronic Materials*, 45(6):2831–2836, 2016.

[146] A Bosacchi, AC De Riccardis, P Frigeri, S Franchi, C Ferrari, S Gennari, L Lazzarini, L Nasi, G Salviati, AV Drigo, et al. Continuously graded buffers for InGaAs/GaAs structures grown on GaAs. *Journal of Crystal Growth*, 175:1009–1015, 1997.

[147] P Sheldon, KM Jones, MM Al-Jassim, and BG Yacobi. Dislocation density reduction through annihilation in lattice-mismatched semiconductors grown by molecular-beam epitaxy. *Journal of Applied Physics*, 63(11):5609–5611, 1988.

[148] JE Ayers. New model for the thickness and mismatch dependencies of threading dislocation densities in mismatched heteroepitaxial layers. *Journal of Applied Physics*, 78(6):3724–3726, 1995.

[149] Y Cordier, P Lorenzini, J-M Chauveau, D Ferre, Y Androussi, J DiPersio, D Vignaud, and J-L Codron. Influence of MBE growth conditions on the quality of InAlAs/InGaAs metamorphic HEMTs on GaAs. *Journal of Crystal Growth*, 251(1-4):822–826, 2003.

[150] Kenneth E Lee and Eugene A Fitzgerald. High-quality metamorphic compositionally graded InGaAs buffers. *Journal of Crystal Growth*, 312(2):250–257, 2010.

[151] M Kawano, T Kuzuhara, H Kawasaki, F Sasaki, and H Tokuda. InAlAs/InGaAs metamorphic low-noise HEMT. *IEEE Microwave and Guided Wave Letters*, 7(1):6–8, 1997.

[152] T Kujofsa and JE Ayers. Evolution of Kinetically Limited Lattice Relaxation and Threading Dislocations in Temperature-Graded ZnSe/GaAs (001) Metamorphic Heterostructures. *Journal of Electronic Materials*, 44(9):3030–3035, 2015.

[153] J-Y Marzin, J-M Gérard, A Izraël, D Barrier, and G Bastard. Photoluminescence of single InAs quantum dots obtained by self-organized growth on GaAs. *Physical Review Letters*, 73(5):716, 1994.

[154] Richard Nötzel, Zhichuan Niu, Manfred Ramsteiner, Hans-Peter Schönherr, Achim Tranpert, Lutz Däweritz, and Klaus H Ploog. Uniform quantum-dot arrays formed by natural self-faceting on patterned substrates. *Nature*, 392(6671):56–59, 1998.

[155] DB Tran Thoai, YZ Hu, and SW Koch. Influence of the confinement potential on the electron-hole-pair states in semiconductor microcrystallites. *Physical Review B*, 42(17):11261, 1990.

[156] S Ates, SM Ulrich, S Reitzenstein, A Löffler, A Forchel, and P Michler. Post-selected indistinguishable photons from the resonance fluorescence of a single quantum dot in a microcavity. *Physical Review Letters*, 103(16):167402, 2009.

[157] Yu-Ming He, Yu He, Yu-Jia Wei, Dian Wu, Mete Atatüre, Christian Schneider, Sven Höfling, Martin Kamp, Chao-Yang Lu, and Jian-Wei Pan. On-demand semiconductor single-photon source with near-unity indistinguishability. *Nature Nanotechnology*, 8(3):213–217, 2013.

[158] Simone Luca Portalupi, Gaston Hornecker, Valérian Giesz, Thomas Grange, Aristide Lemaître, Justin Demory, Isabelle Sagnes, Norberto D Lanzillotti-Kimura, Loïc Lanco, Alexia Auffèves, et al. Bright phonon-tuned single-photon source. *Nano Letters*, 15(10):6290–6294, 2015.

[159] Sebastian Lüker and Doris E Reiter. A review on optical excitation of semiconductor quantum dots under the influence of

phonons. *Semiconductor Science and Technology*, 34(6):063002, 2019.

[160] Thomas K Bracht, Michael Cosacchi, Tim Seidelmann, Moritz Cygorek, Alexei Vagov, V Martin Axt, Tobias Heindel, and Doris E Reiter. Swing-up of quantum emitter population using detuned pulses. *PRX Quantum*, 2(4):040354, 2021.

[161] Nicolas Chauvin, C Zinoni, M Francardi, A Gerardino, L Balet, B Alloing, LH Li, and A Fiore. Controlling the charge environment of single quantum dots in a photonic-crystal cavity. *Physical Review B*, 80(24):241306, 2009.

[162] Jie Sun, Peng Jin, and Zhan-Guo Wang. Extremely low density InAs quantum dots realized in situ on (100) GaAs. *Nanotechnology*, 15(12):1763, 2004.

[163] Oliver Benson, Charles Santori, Matthew Pelton, and Yoshihisa Yamamoto. Regulated and entangled photons from a single quantum dot. *Physical Review Letters*, 84(11):2513, 2000.

[164] Ladislaus Bányai, Ian Galbraith, Claudia Ell, and Hartmut Haug. Excitons and biexcitons in semiconductor quantum wires. *Physical Review B*, 36(11):6099, 1987.

[165] Ranber Singh and Gabriel Bester. Lower bound for the excitonic fine structure splitting in self-assembled quantum dots. *Physical Review Letters*, 104(19):196803, 2010.

[166] M Bayer, G Ortner, O Stern, A Kuther, AA Gorbunov, A Forchel, Pawel Hawrylak, S Fafard, K Hinzer, TL Reinecke, et al. Fine structure of neutral and charged excitons in self-assembled In(Ga)As/(Al)GaAs quantum dots. *Physical Review B*, 65(19):195315, 2002.

[167] LG Wang, Peter Kratzer, Nikolaj Moll, and Matthias Scheffler. Size, shape, and stability of InAs quantum dots on the GaAs (001) substrate. *Physical Review B*, 62(3):1897, 2000.

[168] K Pötschke, L Müller-Kirsch, R Heitz, RL Sellin, UW Pohl, D Bimberg, N Zakharov, and P Werner. Ripening of self-organized InAs quantum dots. *Physica E: Low-dimensional Systems and Nanostructures*, 21(2-4):606–610, 2004.

[169] Ch Heyn. Stability of InAs quantum dots. *Physical Review B*, 66(7):075307, 2002.

[170] E Steimetz, T Wehnert, K Haberland, J-T Zettler, and W Richter. GaAs cap layer growth and In-segregation effects on self-assembled InAs-quantum dots monitored by optical techniques. *Journal of Crystal Growth*, 195(1-4):530–539, 1998.

[171] JS Harris, T O'sullivan, T Sarmiento, MM Lee, and S Vo. Emerging applications for vertical cavity surface emitting lasers. *Semiconductor Science and Technology*, 26(1):014010, 2010.

[172] Tien-Chang Lu, JY Tsai, Hao-Chung Kuo, and SC Wang. Comparisons of InP/InGaAlAs and InAlAs/InGaAlAs distributed Bragg reflectors grown by metalorganic chemical vapor deposition. *Materials Science and Engineering: B*, 107(1):66–69, 2004.

[173] Bertram Eugene Warren. *X-ray Diffraction*. Courier Corporation, 1990.

[174] J-M Chauveau, Y Androussi, A Lefebvre, J Di Persio, and Y Cordier. Indium content measurements in metamorphic high electron mobility transistor structures by combination of x-ray reciprocal space mapping and transmission electron microscopy. *Journal of Applied Physics*, 93(7):4219–4225, 2003.

[175] Cornelius Nawrath. InAs/GaAs quantum dots as sources of non-classical light in the telecom wavelength regime. PhD Thesis, Universität Stuttgart, Institut für Halbleiteroptik und Funktionelle Grenzflächen, 2023.

[176] Ponraj Vijayan. High Contrast Grating Mirror for Photonic Structures Operating at Telecom Wavelength. MSc Thesis, Universität Stuttgart, Institut für Halbleiteroptik und Funktionelle Grenzflächen, 2021.

[177] Stephanie Bauer. Photonic nanostructures for efficient coupling and light enhancement in semiconductor quantum technologies. PhD Thesis, Universität Stuttgart, Institut für Halbleiteroptik und Funktionelle Grenzflächen, 2023.

[178] J Ajayan, D Nirmal, P Mohankumar, Dheena Kuriyan, AS Augustine Fletcher, L Arivazhagan, and B Santhosh Kumar. GaAs metamorphic high electron mobility transistors for future deep space-biomedical-millitary and communication system applications: A review. *Microelectronics Journal*, 92:104604, 2019.

[179] Simon P Philipps, Wolfgang Guter, Elke Welser, Jan Schöne, Marc Steiner, Frank Dimroth, and Andreas W Bett. Present status in the development of III–V multi-junction solar cells. In *Next Generation of Photovoltaics*, pages 1–21. Springer, 2012.

[180] I Kotaka, K Wakita, K Kawano, M Asai, and M Naganuma. High-speed and low-driving-voltage InGaAs/InAlAs multiquantum well optical modulators. *Electronics Letters*, 27(23):2162–2163, 1991.

[181] Klas Hjort. Sacrificial etching of III-V compounds for micromechanical devices. *Journal of Micromechanics and Microengineering*, 6(4):370, 1996.

[182] Yu A Goldberg and NM Schmidt. Handbook series on semiconductor parameters. *vol*, 2:1–36, 1999.

[183] Robert Sittig, Cornelius Nawrath, Sascha Kolatschek, Stephanie Bauer, Richard Schaber, Jiasheng Huang, Ponraj Vijayan, Pascal Pruy, Simone Luca Portalupi, Michael Jetter, et al. Thin-film InGaAs metamorphic buffer for telecom C-band InAs quantum

dots and optical resonators on GaAs platform. *Nanophotonics*, 11(6):1109–1116, 2022.

[184] Y Chen and J Washburn. Structural transition in large-lattice-mismatch heteroepitaxy. *Physical Review Letters*, 77(19):4046, 1996.

[185] CW Snyder, JF Mansfield, and BG Orr. Kinetically controlled critical thickness for coherent islanding and thick highly strained pseudomorphic films of $In_xGa_{1-x}As$ on GaAs (100). *Physical Review B*, 46(15):9551, 1992.

[186] MR Leys. Fundamental growth kinetics in MOMBE/CBE, MBE and MOVPE. *Journal of Crystal Growth*, 209(2-3):225–231, 2000.

[187] Alan G Thompson. MOCVD technology for semiconductors. *Materials Letters*, 30(4):255–263, 1997.

[188] F Bugge, U Zeimer, M Sato, M Weyers, and G Tränkle. MOVPE growth of highly strained InGaAs/GaAs quantum wells. *Journal of Crystal Growth*, 183(4):511–518, 1998.

[189] Takuo Sasaki, Hidetoshi Suzuki, Akihisa Sai, Masamitu Takahasi, Seiji Fujikawa, Itaru Kamiya, Yoshio Ohshita, and Masafumi Yamaguchi. Growth temperature dependence of strain relaxation during InGaAs/GaAs (001) heteroepitaxy. *Journal of Crystal Growth*, 323(1):13–16, 2011.

[190] G Springholz, G Bauer, and V Holy. Scanning-tunneling-microscopy observation of stress-driven surface diffusion due to localized strain fields of misfit dislocations in heteroepitaxy. *Physical Review B*, 54(7):4500, 1996.

[191] A Marti Ceschin and J Massies. Strain induced 2D–3D growth mode transition in molecular beam epitaxy of $In_xGa_{1-x}As$ on GaAs (001). *Journal of Crystal Growth*, 114(4):693–699, 1991.

[192] KR Breen, PN Uppal, and JS Ahearn. Interface dislocation structures in $In_xGa_{1-x}As$/GaAs mismatched epitaxy. *Journal of Vacuum Science & Technology B: Microelectronics Processing and Phenomena*, 7(4):758–763, 1989.

[193] Henry KH Choy and Clifton G Fonstad Jr. Effects of substrate temperature on the growth of InGaAs compositionally graded buffers and on quantum well structures grown above them. *Journal of Vacuum Science & Technology B: Microelectronics and Nanometer Structures Processing, Measurement, and Phenomena*, 23(5):2109–2113, 2005.

[194] A Masalka, E Łusakowska, and P Dłużewski. Anisotropic strain relaxation and surface morphology related to asymmetry in the formation of misfit dislocations in InGaAs/GaAs heterostructures. *Materials Science-Poland*, 26(1), 2008.

[195] Rahul Kumar, Ankush Bag, Partha Mukhopadhyay, Subhashis Das, and Dhrubes Biswas. Investigation of cross-hatch surface and study of anisotropic relaxation and dislocation on InGaAs on GaAs (001). *Electronic Materials Letters*, 12(3):356–364, 2016.

[196] Hidetoshi Suzuki, Takuo Sasaki, Akihisa Sai, Yoshio Ohshita, Itaru Kamiya, Masafumi Yamaguchi, Masamitu Takahasi, and Seiji Fujikawa. Real-time observation of anisotropic strain relaxation by three-dimensional reciprocal space mapping during InGaAs/GaAs (001) growth. *Applied Physics Letters*, 97(4):041906, 2010.

[197] John E Ayers, Tedi Kujofsa, Paul Rago, and Johanna Raphael. *Heteroepitaxy of semiconductors: theory, growth, and characterization.* CRC press, 2016.

[198] IJ Fritz. Role of experimental resolution in measurements of critical layer thickness for strained-layer epitaxy. *Applied Physics Letters*, 51(14):1080–1082, 1987.

[199] J Zou, BF Usher, DJH Cockayne, and R Glaisher. Critical thickness determination of InxGa1-xAs/GaAs strained-layer system by transmission electron microscopy. *Journal of Electronic Materials*, 20(7):855–859, 1991.

[200] Huajian Gao. Some general properties of stress-driven surface evolution in a heteroepitaxial thin film structure. *Journal of the Mechanics and Physics of Solids*, 42(5):741–772, 1994.

[201] JWP Hsu, EA Fitzgerald, YH Xie, PJ Silverman, and MJ Cardillo. Surface morphology of related $Ge_xSi_{1-x}$ films. *Applied Physics Letters*, 61(11):1293–1295, 1992.

[202] F Jonsdottir and LB Freund. Equilibrium surface roughness of a strained epitaxial film due to surface diffusion induced by interface misfit dislocations. *Mechanics of Materials*, 20(4):337–349, 1995.

[203] EA Fitzgerald, SB Samavedam, YH Xie, and LM Giovane. Influence of strain on semiconductor thin film epitaxy. *Journal of Vacuum Science & Technology A: Vacuum, Surfaces, and Films*, 15(3):1048–1056, 1997.

[204] Yasushi Takano, Kazu Kobayashi, Hideaki Iwahori, Masayoshi Umezawa, Sho Shirakata, and Shunro Fuke. Threading dislocations and phase separation in InGaAs layers on GaAs substrates grown by low-temperature metalorganic vapor phase epitaxy. *Japanese Journal of Applied Physics*, 44(9R):6403, 2005.

[205] Zhenzhong Zhang, Jan Berggren, and Mattias Hammar. On the long-wavelength optimization of highly strained InGaAs/GaAs quantum wells grown by metal–organic vapor-phase epitaxy. *Journal of Crystal Growth*, 310(13):3163–3167, 2008.

[206] Yongming Zhao, Jie Huang, Yurun Sun, Shuzhen Yu, Kuilong Li, and Jianrong Dong. Influence of growth conditions on the quality of strained InAlGaAs/AlGaAs quantum wells grown by MOCVD. *Applied Physics A*, 125(2):1–7, 2019.

[207] Tedi Kujofsa and John E Ayers. Design of nonlinear metamorphic buffer layers for lattice-mismatched $In_xGa_{1-x}As/GaAs$ (001) semiconductor devices. *Journal of Vacuum Science & Technology B, Nanotechnology and Microelectronics: Materials, Processing, Measurement, and Phenomena*, 33(5):052206, 2015.

[208] D Sidoti, S Xhurxhi, T Kujofsa, S Cheruku, J Reed, B Bertoli, PB Rago, EN Suarez, FC Jain, and JE Ayers. Critical layer thickness in exponentially graded heteroepitaxial layers. *Journal of Electronic Materials*, 39(8):1140–1145, 2010.

[209] L Seravalli, P Frigeri, M Minelli, P Allegri, V Avanzini, and S Franchi. Quantum dot strain engineering for light emission at 1.3, 1.4 and 1.5 µ m. *Applied Physics Letters*, 87(6):063101, 2005.

[210] Luca Seravalli, Giovanna Trevisi, and Paola Frigeri. Design and growth of metamorphic InAs/InGaAs quantum dots for single photon emission in the telecom window. *CrystEngComm*, 14(20):6833–6838, 2012.

[211] Koichi Yamaguchi Koichi Yamaguchi, Kunihiko Yujobo Kunihiko Yujobo, and Toshiyuki Kaizu Toshiyuki Kaizu. Stranski-Krastanov growth of InAs quantum dots with narrow size distribution. *Japanese Journal of Applied Physics*, 39(12A):L1245, 2000.

[212] OG Schmidt, S Kiravittaya, Y Nakamura, H Heidemeyer, R Songmuang, C Müller, NY Jin-Phillipp, K Eberl, H Wawra, S Christiansen, et al. Self-assembled semiconductor nanostructures: climbing up the ladder of order. *Surface Science*, 514(1-3):10–18, 2002.

[213] K Häusler, K Eberl, F Noll, and A Trampert. Strong alignment of self-assembling InP quantum dots. *Physical Review B*, 54(7):4913, 1996.

[214] Holger Eisele, Andrea Lenz, Robert Heitz, Rainer Timm, Mario Dähne, Yevgeniy Temko, Takayuki Suzuki, and Karl Jacobi. Change of InAs/GaAs quantum dot shape and composition during capping. *Journal of Applied Physics*, 104(12):124301, 2008.

[215] Daniel Richter, Robert Hafenbrak, Klaus D Jöns, Wolfgang-Michael Schulz, Marcus Eichfelder, Matthias Heldmaier, Robert Roßbach, Michael Jetter, and Peter Michler. Low density MOVPE grown InGaAs QDs exhibiting ultra-narrow single exciton linewidths. *Nanotechnology*, 21(12):125606, 2010.

[216] C Carmesin, F Olbrich, T Mehrtens, M Florian, S Michael, S Schreier, C Nawrath, M Paul, J Höschele, B Gerken, et al. Structural and optical properties of InAs/(In)GaAs/GaAs quantum dots with single-photon emission in the telecom C-band up to 77 K. *Physical Review B*, 98(12):125407, 2018.

[217] Kallista Sears, Jenny Wong-Leung, Manuela Buda, Hark Hoe Tan, and C Jagadish. Growth and characterisation of InAs/GaAs quantum dots grown by MOCVD. In *Conference on Optoelectronic and Microelectronic Materials and Devices, 2004.*, pages 1–4. IEEE, 2004.

[218] JG Cederberg, FH Kaatz, and RM Biefeld. The impact of growth parameters on the formation of InAs quantum dots on GaAs (100) by MOCVD. *Journal of Crystal Growth*, 261(2-3):197–203, 2004.

[219] Katharina Zeuner. Semiconductor Quantum Optics at Telecom Wavelengths. PhD Thesis, KTH Royal Institute of Technology, 2020.

[220] AI Tartakovskii, MN Makhonin, IR Sellers, J Cahill, AD Andreev, DM Whittaker, JP R Wells, AM Fox, DJ Mowbray, MS Skolnick, et al. Effect of thermal annealing and strain engineering on the fine structure of quantum dot excitons. *Physical Review B*, 70(19):193303, 2004.

[221] Alexander Högele, Stefan Seidl, Martin Kroner, Khaled Karrai, Richard J Warburton, Brian D Gerardot, and Pierre M Petroff. Voltage-controlled optics of a quantum dot. *Physical Review Letters*, 93(21):217401, 2004.

[222] Senlin Li, Qingqing Chen, Shichuang Sun, Yulian Li, Qiangzhong Zhu, Juntao Li, Xuehua Wang, Junbo Han, Junpei Zhang, Changqing Chen, et al. InAs/GaAs quantum dots with wide-range tunable densities by simply varying V/III ratio using metal-organic chemical vapor deposition. *Nanoscale Research Letters*, 8(1):1–5, 2013.

[223] Qianghua Xie, Anupam Madhukar, Ping Chen, and Nobuhiko P Kobayashi. Vertically self-organized InAs quantum box islands on GaAs (100). *Physical Review Letters*, 75(13):2542, 1995.

[224] JE Ayers, SK Ghandhi, and LJ Schowalter. Crystallographic tilting of heteroepitaxial layers. *Journal of Crystal Growth*, 113(3-4):430–440, 1991.

[225] Rahul Kumar, Ankush Bag, Partha Mukhopadhyay, Subhashis Das, and Dhrubes Biswas. Comparison of different grading schemes in InGaAs metamorphic buffers on GaAs substrate: tilt dependence on cross-hatch irregularities. *Applied Surface Science*, 357:922–930, 2015.

[226] Pawan Sinha, Sarah Crucilla, Tapan Gandhi, Dylan Rose, Amy Singh, Suma Ganesh, Umang Mathur, and Peter Bex. Mechanisms underlying simultaneous brightness contrast: early and innate. *Vision Research*, 173:41–49, 2020.

[227] Yifei Song, Tedi Kujofsa, and John E Ayers. Threading dislocations in InGaAs/GaAs (001) buffer layers for metamorphic high electron mobility transistors. *Journal of Electronic Materials*, 47(7):3474–3482, 2018.

[228] Rosa Leon, S Chaparro, Shane R Johnson, C Navarro, X Jin, Yong-Hang Zhang, Jörg Siegert, S Marcinkevičius, XZ Liao, and

J Zou. Dislocation-induced spatial ordering of InAs quantum dots: Effects on optical properties. *Journal of Applied Physics*, 91(9):5826–5830, 2002.

[229] Gunnar Blume, Max Schiemangk, Johannes Pohl, David Feise, Peter Ressel, Bernd Sumpf, Andreas Wicht, and Katrin Paschke. Narrow linewidth of 633 nm DBR ridge-waveguide lasers. *IEEE Photonics Technology Letters*, 25(6):550–552, 2013.

[230] M Grossmann, M Jetter, and P Michler. Nonlinear reflectivity of AlGaInP SESAMs for mode locking in the red spectral range. *Optics Express*, 30(12):20943–20951, 2022.

[231] RS Goldman, KL Kavanagh, HH Wieder, SN Ehrlich, and RM Feenstra. Effects of GaAs substrate misorientation on strain relaxation in $In_xGa_{1-x}As$ films and multilayers. *Journal of Applied Physics*, 83(10):5137–5149, 1998.

[232] Sudip Saha, Daniel T Cassidy, and DA Thompson. Investigation of cross-hatch in $In_{0.3}Ga_{0.7}As$ pseudo-substrates. *Journal of Applied Physics*, 113(12):124301, 2013.

[233] Megan O Hill, Irene Calvo-Almazan, Marc Allain, Martin V Holt, Andrew Ulvestad, Julian Treu, Gregor Koblmuller, Chunyi Huang, Xiaojing Huang, Hanfei Yan, et al. Measuring three-dimensional strain and structural defects in a single InGaAs nanowire using coherent X-ray multiangle Bragg projection ptychography. *Nano Letters*, 18(2):811–819, 2018.

[234] EC Weiner, R Jakomin, DN Micha, H Xie, P-Y Su, LD Pinto, MP Pires, FA Ponce, and PL Souza. Effect of capping procedure on quantum dot morphology: Implications on optical properties and efficiency of InAs/GaAs quantum dot solar cells. *Solar Energy Materials and Solar Cells*, 178:240–248, 2018.

[235] K Takehana, F Pulizzi, A Patane, M Henini, PC Main, L Eaves, Daniel Granados, and JM Garcia. Controlling the shape of

InAs self-assembled quantum dots by thin GaAs capping layers. *Journal of Crystal Growth*, 251(1-4):155–160, 2003.

[236] R Songmuang, S Kiravittaya, and OG Schmidt. Shape evolution of InAs quantum dots during overgrowth. *Journal of Crystal Growth*, 249(3-4):416–421, 2003.

[237] Qianghua Xie, P Chen, and A Madhukar. InAs island-induced-strain driven adatom migration during GaAs overlayer growth. *Applied Physics Letters*, 65(16):2051–2053, 1994.

[238] F Iikawa, P Motisuke, JA Brum, MA Sacilotti, AP Roth, and RA Masut. Thermally induced In/Ga interdiffusion in $In_xGa_{1-x}As$/GaAs strained single quantum well grown by LP-MOVPE. *Journal of Crystal Growth*, 93(1-4):336–341, 1988.

[239] Wei Zhou, Chak Wah Tang, Jia Zhu, Kei May Lau, Yuping Zeng, HG Liu, NG Tao, and Colombo R Bolognesi. Metamorphic Heterostructure InP/GaAsSb/InP HBTs on GaAs Substrates by MOCVD. *IEEE Electron Device Letters*, 28(7):539–542, 2007.

[240] Wei-Jen Hsueh, Pei-Chin Chiu, Ming-Hwei Hong, and Jen-Inn Chyi. Suppressing Ge diffusion by GaAsSb barriers in molecular beam epitaxy of InGaAs on Ge. *Physica Status Solidi (b)*, 254(2):1600589, 2017.

[241] Keith J Laidler. The development of the Arrhenius equation. *Journal of Chemical Education*, 61(6):494, 1984.

[242] JH Neave, PJ Dobson, BA Joyce, and Jing Zhang. Reflection high-energy electron diffraction oscillations from vicinal surfaces–a new approach to surface diffusion measurements. *Applied Physics Letters*, 47(2):100–102, 1985.

[243] Liang Song, Zhu Hong-Liang, Pan Jiao-Qing, Zhao Ling-Juan, and Wang Wei. Effect of annealing on optical properties of InAs quantum dots grown by MOCVD on GaAs (100) vicinal substrates. *Chinese Physics Letters*, 22(10):2692, 2005.

[244] Fariba Ferdos, Shumin Wang, Yongqiang Wei, Anders Larsson, Mahdad Sadeghi, and Qingxiang Zhao. Influence of a thin GaAs cap layer on structural and optical properties of InAs quantum dots. *Applied Physics Letters*, 81(7):1195–1197, 2002.

[245] Pascal Pruy. Characterization of Single In(Ga)As Quantum Dots as Sources of Nonclassical Light States in the Telecom Spectral Regime. MSc Thesis, Universität Stuttgart, Institut für Halbleiteroptik und Funktionelle Grenzflächen, 2022.

[246] Andreas V Kuhlmann, Julien Houel, Arne Ludwig, Lukas Greuter, Dirk Reuter, Andreas D Wieck, Martino Poggio, and Richard J Warburton. Charge noise and spin noise in a semiconductor quantum device. *Nature Physics*, 9(9):570–575, 2013.

[247] R Mark Stevenson, Robert J Young, Paola Atkinson, Ken Cooper, David A Ritchie, and Andrew J Shields. A semiconductor source of triggered entangled photon pairs. *Nature*, 439(7073):179–182, 2006.

[248] Johannes D Plumhof, Rinaldo Trotta, Armando Rastelli, and Oliver G Schmidt. Experimental methods of post-growth tuning of the excitonic fine structure splitting in semiconductor quantum dots. *Nanoscale Research Letters*, 7(1):1–11, 2012.

[249] Charles H Bennett, Gilles Brassard, Claude Crépeau, Richard Jozsa, Asher Peres, and William K Wootters. Teleporting an unknown quantum state via dual classical and Einstein-Podolsky-Rosen channels. *Physical Review Letters*, 70(13):1895, 1993.

[250] Carl W Wilmsen, Henryk Temkin, and Larry A Coldren. *Vertical-cavity surface-emitting lasers: design, fabrication, characterization, and applications*, volume 24. Cambridge University Press, 2001.

[251] IL Krestnikov, NA Maleev, AV Sakharov, AR Kovsh, AE Zhukov, AF Tsatsul'Nikov, VM Ustinov, Zh I Alferov,

NN Ledentsov, D Bimberg, et al. 1.3 μm resonant-cavity InGaAs/GaAs quantum dot light-emitting devices. *Semiconductor Science and Technology*, 16(10):844, 2001.

[252] Sebastian Maier, Peter Gold, Alfred Forchel, Niels Gregersen, Jesper Mørk, Sven Höfling, Christian Schneider, and Martin Kamp. Bright single photon source based on self-aligned quantum dot–cavity systems. *Optics Express*, 22(7):8136–8142, 2014.

[253] JMea Gerard, D Barrier, JY Marzin, R Kuszelewicz, L Manin, E Costard, V Thierry-Mieg, and T Rivera. Quantum boxes as active probes for photonic microstructures: The pillar microcavity case. *Applied Physics Letters*, 69(4):449–451, 1996.

[254] C Asplund, S Mogg, G Plaine, F Salomonsson, N Chitica, and Mattias Hammar. Doping-induced losses in AlAs/GaAs distributed Bragg reflectors. *Journal of Applied Physics*, 90(2):794–800, 2001.

[255] Fei Ding, Thilo Stöferle, Lijian Mai, Armin Knoll, and Rainer F Mahrt. Vertical microcavities with high Q and strong lateral mode confinement. *Physical Review B*, 87(16):161116, 2013.

[256] D Lu, J Ahn, H Huang, and DG Deppe. All-epitaxial mode-confined vertical-cavity surface-emitting laser. *Applied Physics Letters*, 85(12):2169–2171, 2004.

[257] TK Paraïso, Michiel Wouters, Y Léger, F Morier-Genoud, and Benoit Deveaud-Plédran. Multistability of a coherent spin ensemble in a semiconductor microcavity. *Nature Materials*, 9(8):655–660, 2010.

[258] Jens Jakschik. Investigation and optimization of MOVPE overgrown structured surfaces for resonators operating in the telecom C-Band. MSc Thesis, Universität Stuttgart, Institut für Halbleiteroptik und Funktionelle Grenzflächen, 2022.

[259] Marc Sartison, Lena Engel, Sascha Kolatschek, Fabian Olbrich, Cornelius Nawrath, Stefan Hepp, Michael Jetter, Peter Michler, and Simone Luca Portalupi. Deterministic integration and optical characterization of telecom O-band quantum dots embedded into wet-chemically etched Gaussian-shaped microlenses. *Applied Physics Letters*, 113(3):032103, 2018.

[260] S Martini, AA Quivy, TE Lamas, and ECF Da Silva. Real-time RHEED investigation of indium segregation in InGaAs layers grown on vicinal GaAs (001) substrates. *Physical Review B*, 72(15):153304, 2005.

[261] Marcello Rosini, Maria Clelia Righi, Peter Kratzer, and Rita Magri. Indium surface diffusion on InAs (2× 4) reconstructed wetting layers on GaAs (001). *Physical Review B*, 79(7):075302, 2009.

[262] Hiromitsu Asai. Anisotropic lateral growth in GaAs MOCVD layers on (001) substrates. *Journal of Crystal Growth*, 80(2):425–433, 1987.

[263] Jin Liu, Rongbin Su, Yuming Wei, Beimeng Yao, Saimon Filipe Covre da Silva, Ying Yu, Jake Iles-Smith, Kartik Srinivasan, Armando Rastelli, Juntao Li, et al. A solid-state source of strongly entangled photon pairs with high brightness and indistinguishability. *Nature Nanotechnology*, 14(6):586–593, 2019.

[264] Sascha Kolatschek, Stefan Hepp, Marc Sartison, Michael Jetter, Peter Michler, and Simone Luca Portalupi. Deterministic fabrication of circular Bragg gratings coupled to single quantum emitters via the combination of in-situ optical lithography and electron-beam lithography. *Journal of Applied Physics*, 125(4):045701, 2019.

[265] Cornelius Nawrath, Raphael Joos, Sascha Kolatschek, Stephanie Bauer, Pascal Pruy, Florian Hornung, Julius Fischer, Jiasheng Huang, Ponraj Vijayan, Robert Sittig, et al. High emission rate

from a Purcell-enhanced, triggered source of pure single photons in the telecom C-band. *arXiv preprint arXiv:2207.12898*, 2022.

[266] Kazuya Takemoto, Yoshihiro Nambu, Toshiyuki Miyazawa, Yoshiki Sakuma, Tsuyoshi Yamamoto, Shinichi Yorozu, and Yasuhiko Arakawa. Quantum key distribution over 120 km using ultrahigh purity single-photon source and superconducting single-photon detectors. *Scientific Reports*, 5(1):1–7, 2015.

[267] Kazuya Takemoto, Motomu Takatsu, Shinichi Hirose, Naoki Yokoyama, Yoshiki Sakuma, Tatsuya Usuki, Toshiyuki Miyazawa, and Yasuhiko Arakawa. An optical horn structure for single-photon source using quantum dots at telecommunication wavelength. *Journal of Applied Physics*, 101(8):081720, 2007.

[268] T Miyazawa, K Takemoto, Y Nambu, S Miki, T Yamashita, H Terai, M Fujiwara, M Sasaki, Y Sakuma, M Takatsu, et al. Single-photon emission at 1.5 μ m from an InAs/InP quantum dot with highly suppressed multi-photon emission probabilities. *Applied Physics Letters*, 109(13):132106, 2016.

[269] A Musiał, M Mikulicz, P Mrowiński, A Zielińska, P Sitarek, P Wyborski, M Kuniej, JP Reithmaier, G Sęk, and M Benyoucef. InP-based single-photon sources operating at telecom C-band with increased extraction efficiency. *Applied Physics Letters*, 118(22):221101, 2021.

[270] Pawel Holewa, Aurimas Sakanas, Ugur M Gür, Pawel Mrowinski, Alexander Huck, Bi-Ying Wang, Anna Musial, Kresten Yvind, Niels Gregersen, Marcin Syperek, et al. Bright Quantum Dot Single-Photon Emitters at Telecom Bands Heterogeneously Integrated on Si. *ACS Photonics*, 9(7):2273–2279, 2022.

[271] Dirk Taillaert, Peter Bienstman, and Roel Baets. Compact efficient broadband grating coupler for silicon-on-insulator waveguides. *Optics Letters*, 29(23):2749–2751, 2004.

[272] Niklas Hoppe, Wissem Sfar Zaoui, Lotte Rathgeber, Yun Wang, Rouven H Klenk, Wolfgang Vogel, Mathias Kaschel, Simone Luca Portalupi, Joachim Burghartz, and Manfred Berroth. Ultra-efficient silicon-on-insulator grating couplers with backside metal mirrors. *IEEE Journal of Selected Topics in Quantum Electronics*, 26(2):1–6, 2019.

[273] MR Leys, C Van Opdorp, MPA Viegers, and HJ Talen-Van der Mheen. Growth of multiple thin layer structures in the GaAs-AlAs system using a novel VPE reactor. *Journal of Crystal Growth*, 68(1):431–436, 1984.

[274] Hiroshi Kakibayashi and Fumio Nagata. Composition dependence of equal thickness fringes in an electron microscope image of GaAs/$Al_xGa_{1-x}As$ multilayer structure. *Japanese Journal of Applied Physics*, 24(12A):L905, 1985.

[275] BT Cunningham, LJ Guido, JE Baker, JS Major Jr, N Holonyak Jr, and GE Stillman. Carbon diffusion in undoped, n-type, and p-type GaAs. *Applied Physics Letters*, 55(7):687–689, 1989.

[276] P Kurpas, E Richter, D Gutsche, F Brunner, and M Weyers. Carbon doped GaAs grown by MOVPE using $CBr_4$. In *Compound Semiconductors 1995*, pages 177–182. CRC Press, 2020.

[277] Mitsuhiro Kushibe, Kazuhiro Eguchi, Masahisa Funamizu, and Yasuo Ohba. Heavy carbon doping in metalorganic chemical vapor deposition for GaAs using a low V/III ratio. *Applied Physics Letters*, 56(13):1248–1250, 1990.

[278] Yongkun Sin, Stephen D LaLumondiere, Brendan J Foran, William T Lotshaw, Steven C Moss, Tae Wan Kim, Peter Dudley, Jeremy Kirch, Steven Ruder, Luke J Mawst, et al. Carrier dynamics and defects in MOVPE-grown bulk InGaAs layers with metamorphic InGaAs and InGaPSb buffer layers for solar

cells. In *Physics and Simulation of Optoelectronic Devices XX*, volume 8255, pages 248–259. SPIE, 2012.

[279] D Keiper, R Westphalen, and G Landgren. Comparison of carbon doping of InGaAs and GaAs by $CBr_4$ using hydrogen or nitrogen as carrier gas in LP-MOVPE. *Journal of Crystal Growth*, 197(1-2):25–30, 1999.

[280] Hiroshi Ito, Kenji Kurishima, and Noriyuki Watanabe. Carbon incorporation in InGaAs grown on (311) A oriented substrates by metalorganic chemical vapor deposition. *Journal of Crystal Growth*, 158(4):430–436, 1996.

[281] Tao Lin, Li Jiang, Xin Wei, GH Wang, GZ Zhang, and XY Ma. Growth of heavily Zn-doped InGaAs at low temperature by LP-MOCVD. *Journal of Crystal Growth*, 261(4):490–495, 2004.

[282] D.G. Deppe. Thermodynamic explanation to the enhanced diffusion of base dopant in AlGaAs-GaAs npn bipolar transistors. *Applied Physics Letters*, 56(4):370–372, 1990.

[283] Cheng-Yu Tai, J Seiler, and M Geva. Modeling of Zn diffusion in InP/InGaAs materials during MOVPE growth. In *Conference Proceedings. Eleventh International Conference on Indium Phosphide and Related Materials (IPRM'99)(Cat. No. 99CH36362)*, pages 245–248. IEEE, 1999.

[284] J Dangla, C Dubon-Chevallier, Marcel Filoche, and R Azoulay. Electrical characterisation of the p-type dopant diffusion of highly doped AlGaAs/GaAs heterojunction bipolar transistors grown by MOCVD. *Electronics Letters*, 14(26):1061–1063, 1990.

[285] RJ Field and SK Ghandhi. Doping of gallium arsenide in a low pressure organometallic CVD system: I. Silane. *Journal of Crystal Growth*, 74(3):543–550, 1986.

[286] Li Jiang, Tao Lin, Xin Wei, GH Wang, GZ Zhang, HB Zhang, and XY Ma. Effects of V/III ratio on InGaAs and InP grown

at low temperature by LP-MOCVD. *Journal of Crystal Growth*, 260(1-2):23–27, 2004.

[287] Joan Marie Redwing, H Simka, KF Jensen, and TF Kuech. Study of silicon incorporation from $SiH_4$ in GaAs layers grown by metalorganic vapor phase epitaxy using tertiarybutylarsine. *Journal of Crystal Growth*, 145(1-4):397–402, 1994.

[288] Henry Aldridge Jr, Aaron G Lind, Cory C Bomberger, Yevgeniy Puzyrev, Joshua MO Zide, Sokrates T Pantelides, Mark E Law, and Kevin S Jones. N-type doping strategies for InGaAs. *Materials Science in Semiconductor Processing*, 62:171–179, 2017.

[289] HL Aldridge Jr, AG Lind, ME Law, C Hatem, and KS Jones. Concentration-dependent diffusion of ion-implanted silicon in In0. 53Ga0. 47As. *Applied Physics Letters*, 105(4):042113, 2014.

[290] JE Epler, S Gehrsitz, KH Gulden, M Moser, HC Sigg, and HW Lehmann. Mode behavior and high resolution spectra of circularly-symmetric GaAs-AlGaAs air-post vertical cavity surface emitting lasers. *Applied Physics Letters*, 69(6):722–724, 1996.

[291] Jingtao Zhao, Quanyou Chen, Gang Zhao, Chaoyang Chen, and Zhidong Chen. Damage accumulation mechanism in PIN diode limiters induced via multiple microwave pulses. *Scientific Reports*, 10(1):1–8, 2020.

[292] Jonathan Ensslin. Optical characterization of semiconductor Quantum Dots for electrical excitation in the infrared regime. BSc Thesis, Universität Stuttgart, Institut für Halbleiteroptik und Funktionelle Grenzflächen, 2022.

[293] Chang-Luen Wu and Wei-Chou Hsu. Enhanced resonant tunneling real-space transfer in $\delta$-doped GaAs/InGaAs gated dual-channel transistors grown by MOCVD. *IEEE Transactions on Electron Devices*, 43(2):207–212, 1996.

[294] Manuel Gschrey, Alexander Thoma, Peter Schnauber, Mark Seifried, Ronny Schmidt, Benjamin Wohlfeil, Luzy Krüger, J-H Schulze, Tobias Heindel, Sven Burger, et al. Highly indistinguishable photons from deterministic quantum-dot microlenses utilizing three-dimensional in situ electron-beam lithography. *Nature Communications*, 6(1):1–8, 2015.

[295] S Reitzenstein and A Forchel. Quantum dot micropillars. *Journal of Physics D: Applied Physics*, 43(3):033001, 2010.